Copyright

by

Budi Sutanto Hadisujoto

2013

The Dissertation Committee for Budi Sutanto Hadisujoto Certifies that this is the approved version of the following dissertation:

Control-Oriented Modeling of Dynamic Thermal behavior and Two–phase Fluid Flow in Porous Media for PEM Fuel Cells

Committee:

Tess J. Moon, Supervisor

Dongmei Chen, Co-supervisor

Eric P. Fahrenthold

Benito R. Fernandez

Junjun Liu

Control-Oriented Modeling of Dynamic Thermal behavior and Two–phase Fluid Flow in Porous Media for PEM Fuel Cells

by

Budi Sutanto Hadisujoto, B.S.M.E.; M.S.E.

Dissertation

Presented to the Faculty of the Graduate School of

The University of Texas at Austin

in Partial Fulfillment

of the Requirements

for the Degree of

Doctor of Philosophy

The University of Texas at Austin

December 2013

Dedication

Dedicated to my loving parents

Acknowledgements

I would mostly like thank Dr. Dongmei Chen and Dr. Tess J. Moon for their guidance, continued support, and good faith to finish my study. I would also like to thank Rehan Refai and Alexander Headley for helping me in some of the works. Lastly, I would like to express my gratitude to Chia–Cheng Liu that has been a great friend and for his encouragement and help.

Control-Oriented Modeling of Dynamic Thermal behavior and Two–phase Fluid Flow in Porous Media for PEM Fuel Cells

Budi Sutanto Hadisujoto, Ph.D.

The University of Texas at Austin, 2013

Supervisor: Tess J. Moon

Co-supervisor: Dongmei Chen

The driving force behind research in alternative clean and renewable energy has been the desire to reduce emissions and dependence on fossil fuels. In the United States, ground vehicles account for 30% of total carbon emission, and significantly contribute to other harmful emissions. This issue causes environmental concerns and threat to human health. On the other hand, the demand on fossil fuel grows with the increasing energy consumption worldwide. Particularly in the United States of America, transportation absorbs 75% of this energy source. There is an urgent need to reduce the transportation dependence on fossil fuel for the purpose of national security.

Polymer electrolyte membrane (PEM) fuel cells are strong potential candidates to replace the traditional combustion engines. Even though research effort has transferred the fuel cell technology into real–world vehicle applications, there are still several challenges hindering the fuel cell technology commercialization, such as hydrogen supply infrastructure, cost of the fuel cell vehicles, on–board hydrogen storage, public acceptance, and more importantly the performance, durability, and reliability of the PEM fuel cell vehicles themselves. One of the key factors that affect the fuel cell performance and life is the run–time thermal and water management. The temperature directly affects

the humidification of the fuel cell stack and plays a critical role in avoiding liquid water flooding as well as membrane dehydration which affect the performance and long term reliability. There are many models exists in the literature. However, there are still lacks of control–oriented modeling techniques that describe the coupled heat and mass transfer dynamics, and experimental validation is rarely performed for these models. In order to establish an in–depth understanding and enable control design to achieve optimal performance in real–time, this research has explored modeling techniques to describe the coupled heat and mass transfer dynamics inside a PEM fuel cell. This dissertation is to report our findings on modeling the temperature dynamics of the gas and liquid flow in the porous media for the purpose of control development.

The developed thermal model captures the temperature dynamics without using much computation power commonly found in CFD models. The model results agree very well with the experimental validation of a 1.5 kW fuel cell stack after calibrations. Relative gain array (RGA) was performed to investigate the coupling between inputs and outputs and to explore the possibility of using a single–input single–output (SISO) control scheme for this multi–input multi–output (MIMO) system. The RGA analyses showed that SISO control design would be effective for controlling the fuel cell stack alone. Adding auxiliary components to the fuel cell stack, such as compressor to supply the pressurized air, requires a MIMO control framework.

The developed model of describing water transport in porous media improves the modeling accuracy by adding catalyst layers and utilizing an empirically derived capillary pressure model. Comparing with other control–oriented models in the literature, the developed model improves accuracy and provides more insights of the liquid water transport during transient response.

Table of Contents

ACKNOWLEDGEMENT ..... **V**

ABSTRACT ..... **VI**

LIST OF TABLES ..... **XI**

LIST OF FIGURES ..... **XII**

Chapter 1 Introduction 1

1.1 Background and Motivation 1

1.2 Fuel Cell Components and Operation 5

1.3 PEM Fuel Cell Challenge 9

1.4 Research Objective and Dissertation Outline 14

Chapter 2 Thermal Dynamics Model 16

2.1 Literature Review 16

2.2 Problem Identification 18

2.3 Thermal Dynamics Model Development 19

2.3.1 Fuel Cell Body Control Volume 21

2.3.2 Anode Control Volume 24

2.3.3 Cathode Control Volume 29

2.3.4 Coolant Control Volume 34

2.3.5 Stack Voltage Model 36

2.3.5.1 Activation Loss 38

2.3.5.2 Ohmic Loss 39

2.3.5.3 Concentration Loss 39

2.3 Thermal Dynamics Model Summary 40

Chapter 3 Experimental Setup and Model Calibration and Validation 42

3.1 Experimental Setup 42

3.2 Model Correction and Calibration 45

3.2.1 Sensor Housing Correction 46
3.2.2 Fuel Cell Body Temperature Adjustment 48
3.2.3 Cathode Channel Temperature Adjustment 50
3.2.4 Heating Value Calibration 51
3.3 Model Validation Test 55

Chapter 4 Relative Gain Array Analysis 59
4.1 Relative Gain Array Definition 59
4.2 Case 1: 1.5 kW Fuel Cell Stack 63
4.3 Case 2: 75 kW Fuel Cell Stack 65

Chapter 5 Porous Media Modeling 69
5.1 Literature Review 69
5.2 Model Development 71
5.2.1 Porous Medium Characteristics 74
5.2.1.1 Porosity 74
5.2.1.2 Liquid Water Saturation 74
5.2.1.3 Capillary Pressure 74
5.2.1.4 Relative Permeability 76
5.3 Governing Equations 77
5.3.1 Gas Phase Diffusion 77
5.3.2 Liquid Water Flow 78
5.3.3 Boundary Conditions 81
5.3.3.1 Membrane Boundary Conditions 82
5.3.3.2 Boundary Conditions at the Cathode Channel 84
5.3.3.3 Boundary Conditions at the Anode Channel 86
5.3.4 Stack Voltage Equation 87

Chapter 6 Simulation and Verification of Two–Phase Flow Model for Catalyst Layers 91
6.1 Voltage Calibration 92
6.2 Post Calibration Observation for Potential Improvement 97
6.3 Tuning the Orifice Constant 100

6.4 Utility of The Developed Model for Flooding Estimation 104
6.5 Utilization of the Model for Dead–ended Operation 109
6.5.1 Start–up Response.....110
6.5.2 Step Response 115
Chapter 7 Conclusion and Future Work 120
7.1 Conclusion 120
7.2 Contribution 121
7.3 Future Work 122
Appendix A Parameters, Symbols, and Definitions 124
Appendix B Fuel Cell Stack Dimension.....126
Appendix C Thermal Model Linarization Results.....127
Appendix D Regression Summary.....140
Appendix E Simulink.....141
References.....146

List of Tables

Table 2.1: Heat conduction coefficients at 350K.....28

Table 3.1: Input set values of the test experiment.....44

Table 4.1: RGAs for the relation $\begin{bmatrix} V_{st} \\ T_{ca,out} \end{bmatrix} = RGA \begin{bmatrix} \dot{m}_{ca,in} \\ \dot{m}_{col,in} \end{bmatrix}$.....64

Table 4.2: RGAs for the relation $\begin{bmatrix} V_{st} \\ T_{ca,out} \end{bmatrix} = RGA \begin{bmatrix} \dot{m}_{ca,in} \\ T_{col,in} \end{bmatrix}$.....65

Table 4.3: RGAs for the relation $\begin{bmatrix} P_{gen} \\ T_{st} \end{bmatrix} = RGA \begin{bmatrix} V_{cmpr} \\ \dot{m}_{col} \end{bmatrix}$ of the 75 kW Fuel Cell Stack [65].....66

Table 4.4: RGAs for the relation $\begin{bmatrix} P_{net} \\ T_{st} \end{bmatrix} = RGA \begin{bmatrix} V_{cmpr} \\ \dot{m}_{col} \end{bmatrix}$ of the 75kW Fuel Cell Stack [65].....67

Table 6.1: The parameter result from regression analysis and manual adjustment 96

Table 6.2: Inputs of the dead–ended anode simulation.....109

List of Figures

Figure 1.1: The Program of reducing the high-volume manufacturing cost of automotive fuel cell systems. (Cost estimates are based on dollars for the year the estimate was made; cost targets are based on 2002 dollars) [13] 3

Figure 1.2: The Program of improving the durability of automotive fuel cells under real–world operating conditions [14].....4

Figure 1.3: The Program of increasing the durability of critical fuel cell components [14].....4

Figure 1.4: Fuel cell system durability over the years [15].....5

Figure 1.5: Fuel cell stack and single cell illustration [23] 6

Figure 1.6: PEM fuel cell components and reaction schematic (not drawn to scale) 7

Figure 1.7: An example of polarization curves of a PEM fuel cell operating at different cathode pressures [60].....8

Figure 1.8: Polarization curves showing the effect of water flooding on fuel cell performance [26].....10

Figure 1.9: Accumulation of liquid water droplets over time period on the cathode GDL and flow channel interface at temperature 30ºC [36] 11

Figure 1.10: ESEM images of vapor condensation and liquid water breakthrough in CL [34].....11

Figure 1.11: ESEM images of vapor condensation and liquid water breakthrough in GDL [34].....12

Figure 1.12: Water transport phenomena in PEM fuel cell.....13

Figure 2.1: Problem definition of a single cell of the fuel cell model (not drawn to scale) 18
Figure 2.2: Defining control volumes (CVs) of a single cell of the fuel cell model 20
Figure 2.3: Thermal model block diagram 20
Figure 2.4: Fuel cell body block diagram.....22
Figure 2.5: Anode channel block diagram 25
Figure 2.6: Cathode channel block diagram.....29
Figure 2.7: Coolant channel block diagram 34
Figure 3.1: Fuel cell experimental test station.....43
Figure 3.2: Fuel cell stack test station schematic 43
Figure 3.3: Polarization and alternating step current load profiles respectively .45
Figure 3.4: Sensor housing corrected model of the cathode outlet temperature and the experimental cathode outlet temperature comparison 47
Figure 3.5: The fuel cell body temperature before and after adjusting the fuel cell body surface temperature.....49
Figure 3.6: Cathode outlet temperature before and after cathode temperature calibration 50
Figure 3.7: Model and experimental temperature comparison (E = 1.48V, HHV assumption).....51
Figure 3.8: Model and experimental temperature comparison (E = 1.25V, LHV assumption).....52
Figure 3.9: Model and experimental temperature comparison (E = 1.4V) 52
Figure 3.10: Model voltage results and experimental voltage comparison.....53

Figure 3.11: Model and experimental coolant and fuel cell body temperatures comparison 55
Figure 3.12: Model and experimental temperature step load validation (E = 1.4V) 56
Figure 3.13: Voltage model results versus experimental validation test 57
Figure 3.14: Coolant and fuel cell body model and experimental temperatures comparison 58
Figure 4.1: Closed–loop system diagram [110,114] 60
Figure 5.1: PEM fuel cell components and reaction schematic (not drawn to scale) 72
Figure 5.2: Illustration of water transport in hydrophobic porous media [33] 75
Figure 5.3: Liquid water droplets on GDL surface at different wettability at 70°C [59] 76
Figure 5.4: Experimentally determined capillary pressure of a GDL (Toray 060) and a CL. The fitting parameters of a_1, a_2, b, c, and d are –17.3, –25.1, 32.3, 0.35, and –4.06 for GDL G1 and –23.5, –17.4, 477.0, 0.46 and –3.58 for CL, respectively 81
Figure 5.5: Schematic diagram of the discretization of the porous media layers 78
Figure 6.1: Individual cell voltages and the average cell voltage of the 30–cell fuel cell stack 92
Figure 6.2: Initial simulation of the voltage response 93
Figure 6.3: Stack voltage comparison between model and experimental data 96
Figure 6.4: Rectangle area focus of voltage step change observation 98
Figure 6.5: Voltage step change observation magnification of Figure 6.5 99
Figure 6.6: Voltage degradation at high current load 99
Figure 6.7: Step current load input 101

Figure 6.8: Step voltage response with orifice constant of 1e–7 sec/m 102
Figure 6.9: Anode and cathode experimental step input inlet pressures 102
Figure 6.10: Step voltage response with orifice constant of 1.45e–8 sec/m 103
Figure 6.11: Step voltage response with orifice constant of 1.45e–8 sec/m, offset –0.6 Volts.....104
Figure 6.12: Model predictions of saturation level in the anode GDL and CL...105
Figure 6.13: Model predictions of saturation level in the cathode GDL and CL 105
Figure 6.14: Model predictions of liquid water accumulation in the channel.....106
Figure 6.15: Model predictions of anode and cathode channel RHs.....107
Figure 6.16: Anode and cathode inlet RHs 107
Figure 6.17: Model predictions of membrane water content 108
Figure 6.18: Dead–ended anode cell voltage during start–up 111
Figure 6.19: Liquid water accumulation in the anode channel during start–up ..111
Figure 6.20: Hydrogen and oxygen concentrations in the CLs during start–up..111
Figure 6.21: Relative humidity in the anode and cathode channels during start–up.. 112
Figure 6.22: Saturation levels in the anode GDL and CL during start–up.....113
Figure 6.23: Saturation levels in the cathode GDL and CL during start–up.....113
Figure 6.24: Membrane water content during start–up 114
Figure 6.25: Step response cell voltage.....115
Figure 6.26: Step response liquid water accumulation in the anode channel.....116
Figure 6.27: Step response hydrogen and oxygen concentrations in the CLs.....116
Figure 6.28: Step response relative humidity in the anode and cathode channels 117
Figure 6.29: Step response saturation levels in the anode GDL and CL.....117
Figure 6.30: Step response saturation levels in the cathode GDL and CL.....118

Figure 6.32: Step response membrane water content.....118

Chapter 1: Introduction

1.1 Background and Motivation

Fuel cells are electrochemical devices that convert chemical energy from reactant and oxidant directly into electrical energy. They have very promising future as clean, near–zero emission, high efficiency electric generators. Of the many types of fuel cells, Polymer Electrolyte Membrane (PEM) fuel cells are the most feasible option for portable electric generator and electric vehicle propulsion.

Hydrogen is the most common reactant used as the fuel for fuel cells and reacts with oxygen to form water and released heat as the by–product of the reaction. Although it does not exist in its natural molecular form of H_2, hydrogen is abundant element on earth. Today, most hydrogen production is derived by thermal processing such as reformation of natural gas or liquid fuels, gasification of coal or biomass, or high–temperature water splitting. Electrolytic process that uses electricity to split water into hydrogen and oxygen can also be used. Hydrogen produced via electrolysis can result in zero green house gas (GHG) emissions, depending on the source of the electricity used. Many renewable electric energy resources can be used such as wind, solar, hydroelectric, geothermal, which make the fuel cells very close to zero emission energy producer [1, 2].

Currently, about 70% energy consumed in the United States comes from fossil fuels [3]. The largest consumer is the transportation sector that accounts for nearly two–thirds of the annual consumption. Three quarter of the fossil fuels for transportation is used to power ground vehicles, such as cars, trucks, and buses. These vehicles are responsible for over 60% of the carbon monoxide emissions and about 20% of greenhouse gas emissions [4]. A transportation system powered by hydrogen fuel cells

would significantly reduce dependence on fossil fuels and emissions of harmful pollutants and greenhouse gases not only in the United States but also worldwide that shows a growing demand for energy, particularly in China, India, and other developing countries.

Feasibility studies showed that among many types of fuel cells, a PEM fuel cell type is the most viable application for ground vehicle transportation because of its advantages: high power density, relatively quick start-up, rapid response to varying loads, and low operating temperatures (~80°C) [5, 6]. In automotive industry, it was predicted to replace combustion engines due to its higher efficiency and much lower tail–pipe emission than that of combustion engines [7, 8].

Today's world automotive manufacturers such as Ford, General Motors, Daimler AG, Toyota and others have tested their fuel–cell–powered vehicle prototypes on the road. Honda has even been leasing its fuel–cell–powered car, FCX Clarity, in some areas in Southern California where designated hydrogen refueling stations are available [9]. Additionally, plug–in hybrid battery technology in combination with fuel cells may offer a better alternative vehicle operating strategy [10].

However, there are several challenges facing fuel cell technology commercialization, such as hydrogen supply infrastructure, cost of the fuel cell vehicles, on–board hydrogen storage, public acceptance, and more importantly the performance, durability, and reliability of the PEM fuel cell vehicles themselves [11]. Great efforts have been put to address the above issues. In 2005, feasibility studies conducted by the United States Department of Energy (DOE) have shown the pathways to reduce the hydrogen cost from $5 to $2–$3 per gallon gasoline equivalent and the possibility to establish localized cost–effective hydrogen production [12]. Auto companies have been actively pursuing cost reduction of fuel cell vehicles, and have reduced the fuel cell

system cost from $275/kW in 2002 to $47/kW in 2012 (Figure 1.1) [13]. They also demonstrated the desired on–board hydrogen storage capability by using high pressure storage tanks.

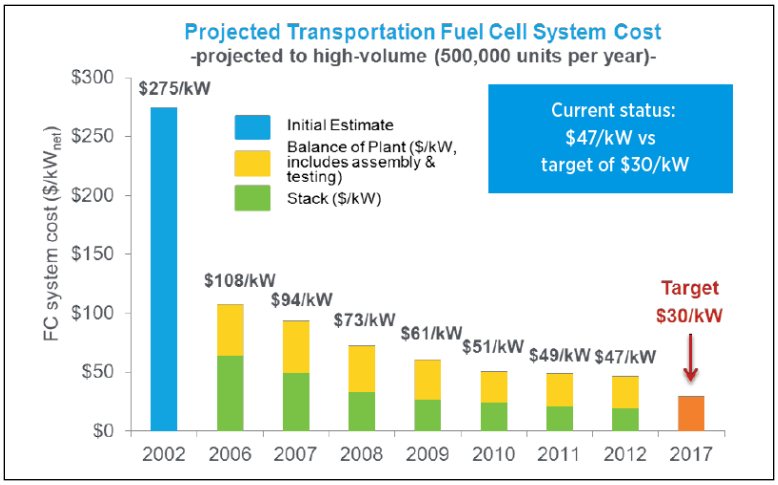

Figure 1.1: The program of reducing the high–volume manufacturing cost of automotive fuel cell systems. (Cost estimates are based on dollars for the year the estimate was made; cost targets are based on 2002 dollars) [13].

While progress is being made in the other areas towards fuel cell vehicle commercialization, the performance, durability, and reliability of the fuel cell vehicles remain the main critical challenge. Over the past couple of decades, fundamental research has been conducted to advance PEM fuel cells from laboratories to consumer vehicles. Significant improvements are still required in order to reach the targeted fuel cell life of 5,000 hours (Figure1.2) [14].

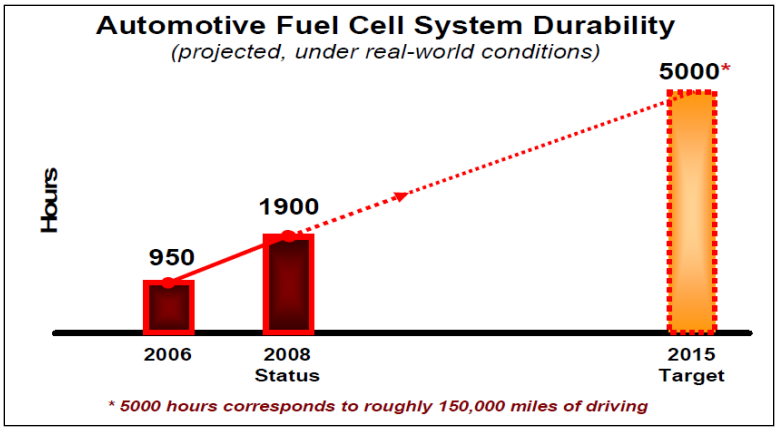

Figure 1.2: The Program of improving the durability of automotive fuel cells under real–world operating conditions [14].

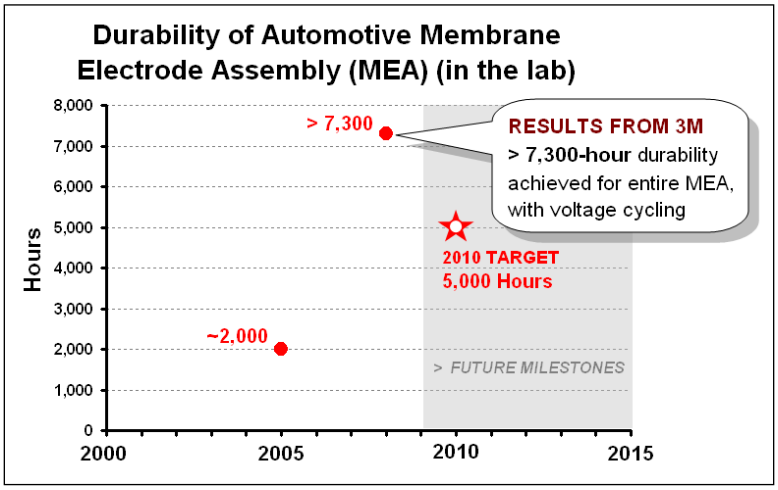

Figure 1.3: The Program of increasing the durability of critical fuel cell components [14].

Currently in real–world environments, fuel cell stack durability is about half of what experts believe for commercialization. Durability has increased substantially over the past few years from 29,000 miles in 2006 to 75,000 miles in 2010. However a 150,000–mile expected lifetime is necessary for fuel cell vehicles to compete with gasoline vehicles (Figure 1.4) [15].

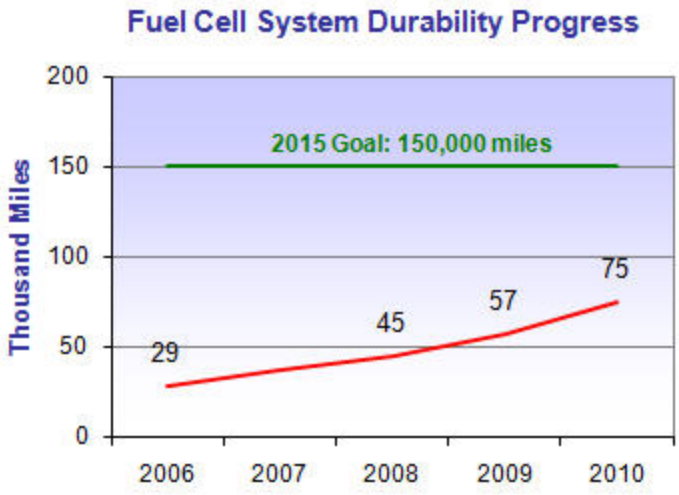

Figure 1.4 : Fuel cell system durability over the years [15].

Numerous researchers have demonstrated that one of the key factors affecting fuel cell performance and life is the run–time thermal and water management [16–21, 24–42]. The thermal and water dynamics, as well as the electrochemical reaction in the PEM fuel cell are coupled which complicate the system behavior. The fuel cell stack temperature directly affects the humidification condition of the fuel cell stack and plays a critical role in avoiding liquid water flooding as well as membrane dehydration which affect the long term reliability [17–22].

1.2 FUEL CELL COMPONENTS AND OPERATION

Depicted in Figure 1.5, a PEM fuel cell stack consists of many single fuel cells stacked together in series to multiply the voltage output of a single cell, much like batteries. A single cell of a PEM fuel cell consists of a layer of polymer electrolyte membrane and anode and cathode electrodes. The membrane is sandwiched between the anode and cathode electrodes.

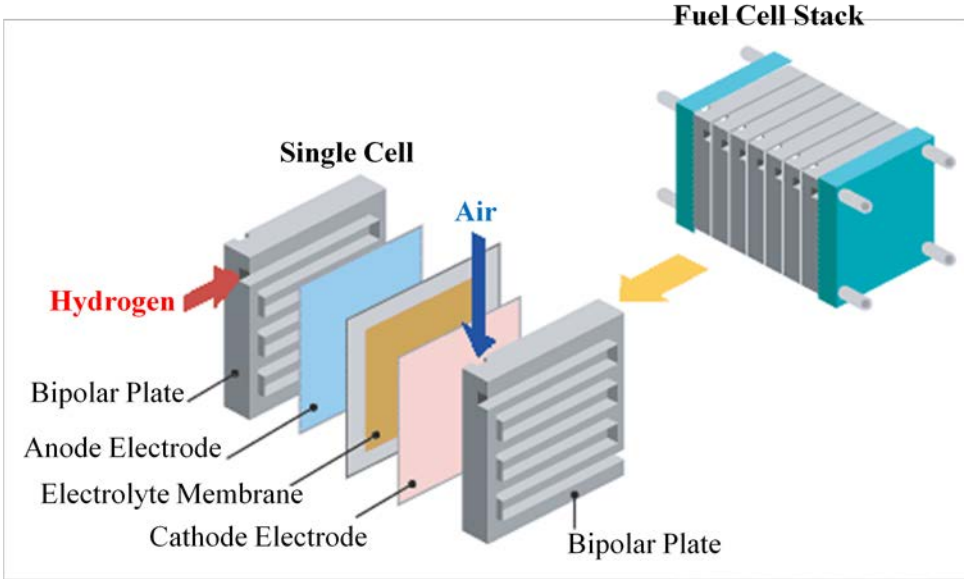

Figure 1.5: Fuel cell stack and single cell illustration [23].

Each electrode consists of a Catalyst Layer (CL), a Gas Diffusion Layer (GDL), and a bipolar plate, arranged such that shown in the schematics shown in Figures 1.5 and 1.6. The catalyst is utilized for splitting the hydrogen and oxygen gas molecules into ions. Typically platinum nano–particles attached to carbon micro–particles form the catalyst. The GDL is a porous material with the main function is to distribute the reactant gas flow from the gas channels to the catalyst layer, repel liquid water to flow out from the catalyst layer to the gas channel, and support the membrane and catalyst layer. Carbon paper and carbon cloth are two types of porous media commonly used for PEM fuel cell as GDL. The GDL is usually hydrophobized with tetrafluoroethylene, also known as Teflon, to wick out liquid water. The bipolar plate serves as gas channels and to conduct the electricity. It is usually made from a high conductivity material such as graphite.

In PEM fuel cell manufacturing, generally the membrane is pressed with CLs and GDLs on both the anode and cathode sides, forming the Membrane Electrolyte Assembly (MEA).

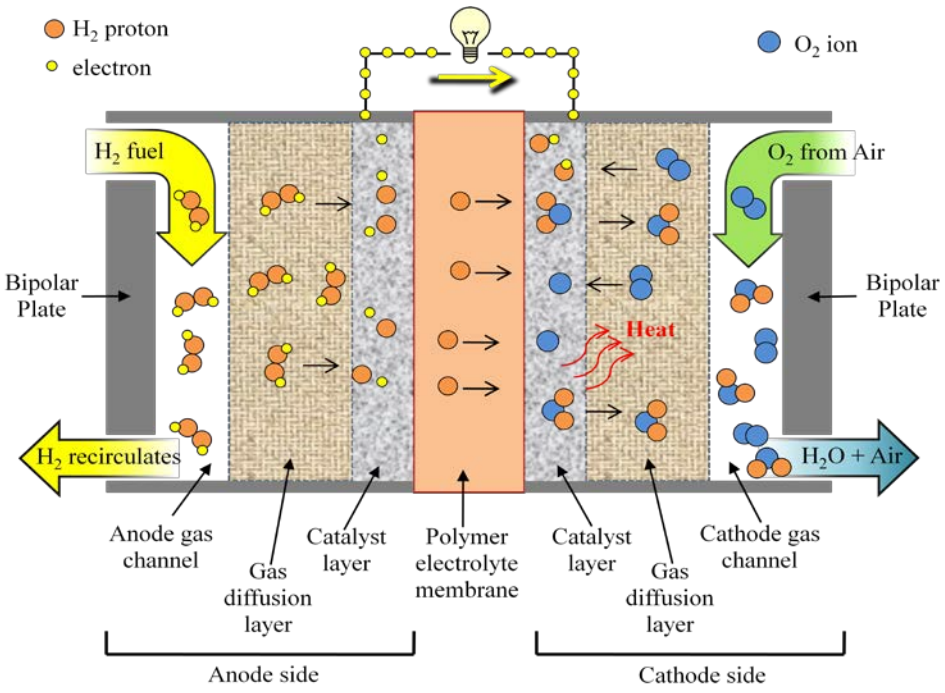

Figure 1.6: PEM fuel cell components and reaction schematic (not drawn to scale).

During the fuel cell operation, reactant and oxidant gases are supplied to both electrodes via the bipolar plates. When the hydrogen gas flows in the anode side, hydrogen molecules are split into positive hydrogen ions (protons) and electrons by the anode catalyst.

$$2\,H_2 \Rightarrow 4\,H^+ + 4\,e^- \tag{1.1}$$

On the cathode side, the oxygen molecules are also split by the cathode catalyst into negative oxygen ions and attract hydrogen protons and form water.

$$O_2 + 4\,H^+ + 4\,e^- \Rightarrow 2\,H_2O \tag{1.2}$$

Thus the overall reaction is

$$2\,H_2 + O_2 \Rightarrow 2\,H_2O \tag{1.3}$$

Referring to Figure 1.6, the main characteristic of the membrane is that it is only permeable to positive ions (hydrogen protons) while blocking electrons. Since the electrons in the anode side cannot pass through the membrane, they are forced to flow through the outside circuit which then generate electric current and combine together with hydrogen and oxygen to form water in the cathode CL. Water and heat are produced as by–products of the chemical reaction.

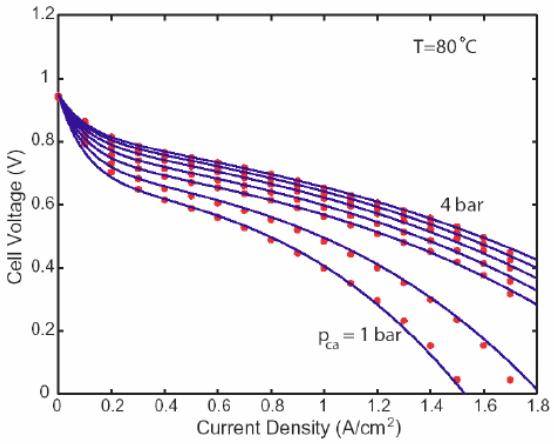

Figure 1.7: An example of polarization curves of a PEM fuel cell operating at different cathode pressures [60].

Typically the performance characteristics of PEM fuel cells are represented in the form of polarization curve where the cell voltage is plotted against current density (current per unit cell of membrane active area). Figure 1.7 is an example of polarization curves of a PEM fuel cell at different cathode pressures.

When condensation occurs, the hydrophobic GDL wicks the liquid water away from the membrane and CL to the gas channels for removal. The production, phase transformation, and transport of water within the fuel cell are critical for efficient performance and long life of the PEM fuel cell. As an example, the hydrogen proton

transport, also known as proton conductivity, is directly dependent upon the water content of the membrane.

1.3 PEM FUEL CELL CHALLENGE

Thermal and water management has been expressed frequently in the literature as the most important and critical factor in the PEM fuel cell operation to have high performance, efficiency and reliability [20, 21, 24–32]. Referring to Figure 1.6, during the fuel cell operation, heat and water are generated as by–product at the cathode catalyst layer where the reaction occurs. Due to low operation temperature of the PEM fuel cell which is generally around 50°C to 80°C, the water can be in two phases, vapor and/or liquid. When the water vapor is thermodynamically saturated, it condenses into liquid form and fills the empty pores of the porous media, i.e. GDL and CL. If the liquid water is not properly removed, its accumulation leads to poor fuel cell performance by blocking the gas pores which are the pathway for gas reactant transport, and eventually could form a thin liquid water layer as the barrier over the reactive area rendering it inactive. This phenomenon is known as flooding and becomes one of the major issues of low performance PEM fuel cells especially in providing high current density output [26, 32–40].

Figure 1.8 illustrates a comparison of polarization curves with various degrees of flooding. At higher current densities, the severer the flooding is, the steeper the slopes of the cell performance curves [26].

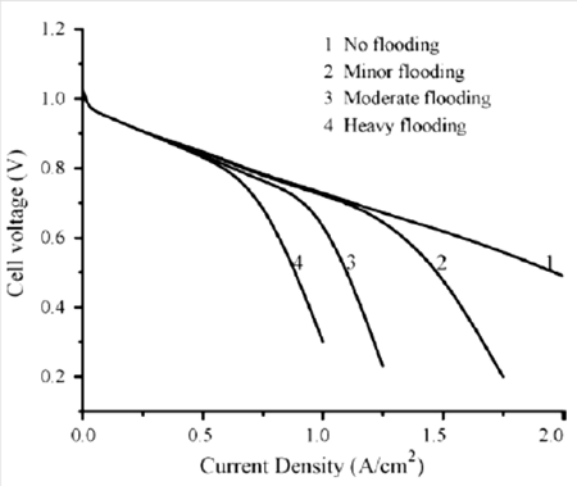

Figure 1.8: Polarization curves showing the effect of water flooding on fuel cell performance [26].

Flooding can be visualized experimentally by using a transparent fuel cell body, as shown in Figure 1.9. The thick dark grey color lines are the gas channels, the white dots in the channels are water droplets and white areas along the channels are liquid water film. When the fuel cell runs at steady state at a constant stack temperature, water droplets grow and form liquid film over the time.

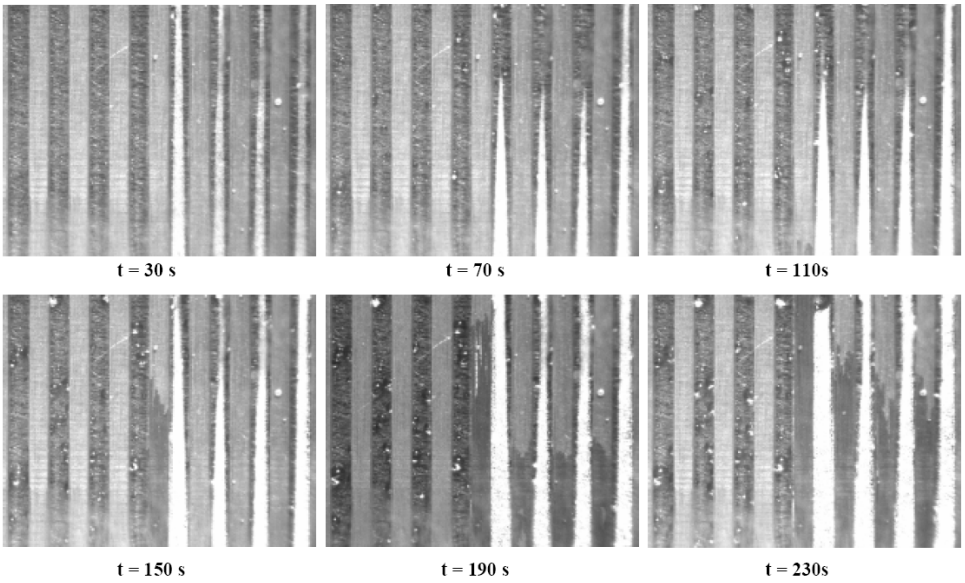

Figure 1.9: Accumulation of liquid water droplets over time period on the cathode GDL and flow channel interface at temperature 30ºC [36].

To look more closely at the flooding, Figures 1.10 and 1.11 show the ESEM (Environmental Scanning Electron Micrograph) images of the liquid water accumulation in the CL and carbon paper GDL. It can be seen that the water droplets become bigger over the time.

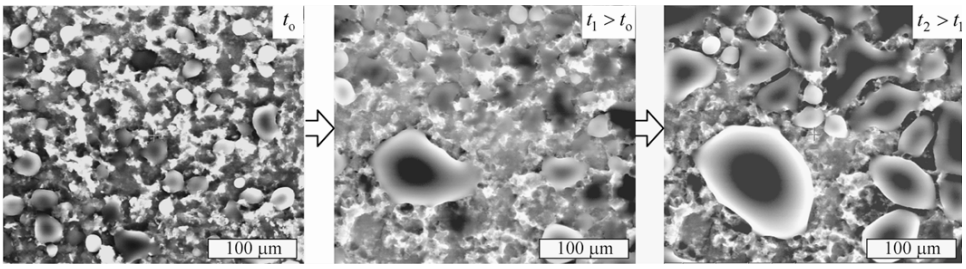

Figure 1.10: ESEM images of vapor condensation and liquid water breakthrough in CL [34].

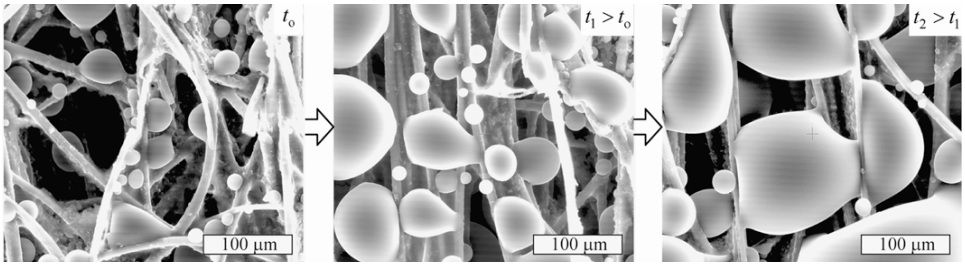

Figure 1.11: ESEM images of vapor condensation and liquid water breakthrough in GDL [34].

In order to have good performance, the polymer membrane must be sufficiently hydrated to have high hydrogen proton conductivity. However during the reaction, the hydrogen protons drag the water molecules in the membrane when moving from the anode to the cathode. This is known as electro–osmosis drag which causes membrane dehydration that decreases the hydrogen proton conduction (Figure 1.12). Moreover many investigations have shown that membrane dehydration degrades the membrane life and fuel cell component reliability such as hot spot, membrane holes, catalyst degradation, carbon corrosion of fuel cell components due to electrochemical reaction, etc [41–45].

To prevent membrane dehydration, water vapor humidification is typically added to the anode gas stream to compensate for the water deficiency. Humidification of the cathode gas stream may also be needed to increase back diffusion, although water is generated in the cathode.

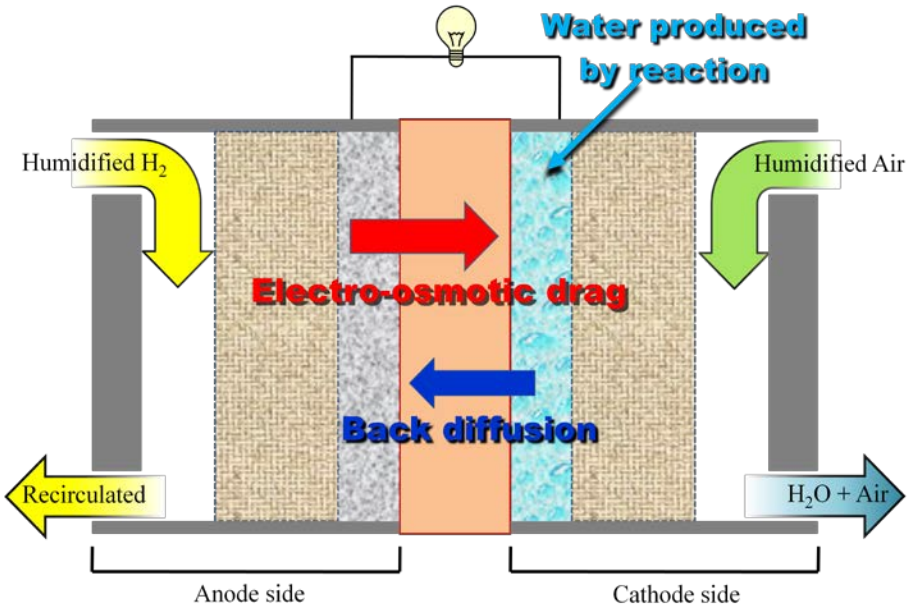

Figure 1.12: Water transport phenomena in PEM fuel cell.

Many experiments in the literature suggest humidification of gaseous fuel in either or both anode and cathode channels to minimize water shortage in the membrane [21, 46]. However, adding humidification to reactant gasses can worsen the flooding problem. This competition between porous media flooding avoidance and membrane hydration needs to be investigated [27, 47].

Thermal and water dynamics models provide a fundamental understanding of the liquid and gas transport which represents the aforementioned problem. Later, control schemes can be applied to the model to maintain water balance in the membrane and prevent liquid water residing in the porous media to achieve optimum fuel cell performance.

1.4 RESEARCH OBJECTIVE AND DISSERTATION OUTLINE

The coupling between temperature and flooding effects on fuel cell performance makes the thermal and the two–phase flow in the porous media models crucial in developing a PEM fuel cell model. Such a model can be used to understand the dynamic thermal and water behavior of the fuel cell system and to investigate the coupling between the thermal effect and mass transport for thermal and water management purpose and to develop control strategies over a wide operation range, especially a wide temperature swing such as in cold weather condition. The goal of this research is to construct models that can capture the temperature and water flow dynamics of the PEM fuel cell by adding to and improving existing physics–based dynamic models for control application without adding too much complexity and calculation time and can also be used for control development and optimization.

The development of a thermal subsystem model that is suitable for control study is explained in Chapter 2. The modeling technique presented is based on the first law of thermodynamics using a control volume approach to describe the transient dynamic thermal behavior [60]. The main purpose of the model is to represent the temperatures of the fluid in the anode and cathode channels, the coolant temperature, and the fuel cell body temperature which all of them influence the mass transport.

Experimental validation was performed on a 1.5 kW, 30–cell fuel cell stack in the Advance Power Systems and Control Laboratory, at The University of Texas at Austin. The fuel cell experimental setup and the results are presented in Chapter 3. The modeled temperatures agreed with the fuel cell specification and experimental data after the model was calibrated, thus validating the accuracy of the model. The model predicts the transient temperature behavior similar to that reported in the literature [53, 55–57].

There are two main dynamics, which are the mass transfer and the heat transfer, in the PEM fuel cell system. This renders the fuel cell a multi–input multi–output (MIMO) system. Relative Gain Array (RGA) analyses were performed in order to investigate the coupling of these two dynamics and explore the possibility of using a decentralized single–input single–output (SISO) control strategy. Two cases are analyzed, 1.5 kW and 75 kW fuel cell stacks, and the results are presented and discussed in Chapter 4.

Liquid water flooding in the PEM fuel cell presents a major problem to fuel cell performance. It will be shown in Chapter 5, the effect of the liquid water residing in the porous media as well as in the channel to the cell voltage output. The dead–ended anode is employed to show the liquid water accumulation. Finite difference is applied to the GDL and CL to solve the ordinary differential equations of the gas diffusion and liquid water saturation. The simulation results are presented in Chapter 6. At the end, conclusions and future work are presented in Chapter 7.

Chapter 2: Thermal Dynamics Model

2.1 Literature Review

Several PEM fuel cell thermal models exist in the literature [48–57]. However, only a few are developed for control optimization. Khemili et al. made a one–dimensional model that predicted the non–uniformity of the temperature distribution with respect to time under a constant current load [48]. The model also pointed out the effect of liquid water on the temperature variations. The temperature profile showed the maximum took place at the membrane electrolyte assembly where the reaction and heat generation occurred. The model used a finite element method which is heavy on computation and thus is not suitable for control application. Shimpalee et al. developed a Computational Fluid Dynamics (CFD) model to describe the fuel cell transient response under variable current load that considered the electrochemical process and water transport [50]. The simulation result showed a voltage overshoot due to the non–uniform reactant distribution in response to the change of current load. However, the model did not emphasize on the thermal dynamics during transient response and also was heavy on computation.

Martins et al. employed seven control volumes to represent the spatial temperature distribution within the fuel cell stack [51]. Non–invasive temperature measurements were performed using an infrared probe and revealed the heat concentration at the membranes. They verified that the temperature distribution is not uniform, even at low current demands, and developed a representative model for thermal distribution in the flow direction. Their study was focused towards design optimization and is not applicable for control optimization due to the high computational expense. A thermodynamic and species conservation model for control design of fuel cell reformers was presented by Di Penta et al. [52]. The model incorporated species variations within

the reformer and fuel cell stack to understand the effect of carbon oxide poisoning on stack efficiency. Reasonable agreement was obtained between experimental and simulation results. However the anode, cathode, and the fuel cell body were lumped together to a single temperature term which is not suitable for anode or cathode specific control concerns, such as the flow rate and relative humidity, given the lack of understanding of the temperature inside each channel.

Muller et al. developed a control–oriented model that showed a good correlation with the experimental validation [53]. The thermal model was developed based on control volume approach neglecting spatial temperature variation which simplified the computation greatly and thus is suitable for control application. Nonetheless, the fuel cell temperature was again lumped into a single value of the bulk fuel cell body temperature. Although this bulk fuel cell body temperature captured the transient response closely to experimental data, it is not sufficient to measure the temperature in the anode and cathode gas channels. Kolodziej also developed a thermal model for nonlinear control application [54]. The fuel cell stack was modeled according to a lumped parameter continuous–flow stirred tank reactor (CSTR) form. Nonetheless, the model was aimed only to maintain the coolant temperature to control the overall temperature of the fuel cell stack. Similar thermal model represented by a lumped thermal mass model of a fuel cell stack was proposed by Zhang et al. [55]. Then again, the model was also aimed to capture the overall stack temperature and the coolant temperature in the radiator. Much alike, Choe et al. made a simple lumped thermal sub–model that was included into fuel cell voltage model to account thermal effect during dynamic load input [56– 57].

Based on the literature reviews mentioned above, it can be concluded that control volume lumped–mass approach is best suited for control–oriented thermal dynamics model development. The approach does not require a heavy computation typically found

in CFD models. However the drawback is that the spatial variation is ignored which is not that critically important for control application.

2.2 PROBLEM IDENTIFICATION

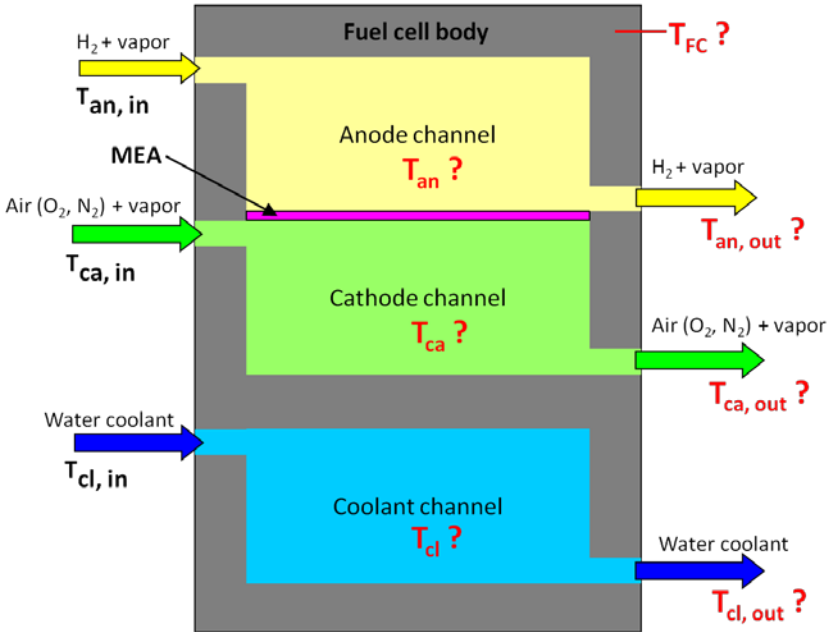

Figure 2.1: Schematic of thermal model problem definition of a fuel cell stack (not drawn to scale).

Referring to Figure 2.1 above, the letter T symbolizes the temperature, the subscripts an, ca, cl, and FC symbolize the anode, cathode, coolant, and fuel cell respectively. The arrows signify the directions of the fluid flow in the inlet and outlet of the fuel cell body.

Figure 2.1 schematic identifies the known temperatures represented by a fuel cell stack and those that are sought for control application purpose. The stack consists of single cells that are connected in series; thus the fluid channels are connected from one

cell to another in series also. The stack has three channels which each channel has a single inlet and single outlet. The channels are the anode, cathode, and coolant channels.

The stack channel inlet temperatures are known and the mass flows and heat generated by the reaction determine the unknown temperatures in every channel, channel outlet and the fuel cell body. One can predict that when the steady state occurs all the temperatures are constant and in balance to each other, signifying an interaction among those temperatures. This interaction is shown in the energy balance equations in the modeling section.

The other known inputs to the fuel cell stack shown in Figure 2.1 are the inlet mass flow rates and pressure of humidified hydrogen gas into the anode channel, the inlet mass flow rates and pressure of humidified air into the cathode channel, and the mass flow rates of liquid water into the coolant channel. The ambient temperatures of the fuel cell stack and the current drawn from the fuel cell are also known.

2.3 THERMAL DYNAMICS MODEL DEVELOPMENT

The developed thermal model is based on the first law of thermodynamics using control volume approach. The fuel cell stack is divided into four control volumes to estimate the transient temperature dynamics. As previously mentioned, spatial variations of temperature in each control volume are neglected, thus the model is lumped into ordinary differential equations.

The four control volumes defined in a fuel cell stack schematic in Figure 2.2 are the anode channel control volume, the cathode channel control volume, the fuel cell body control volume, and the coolant channel control volume.

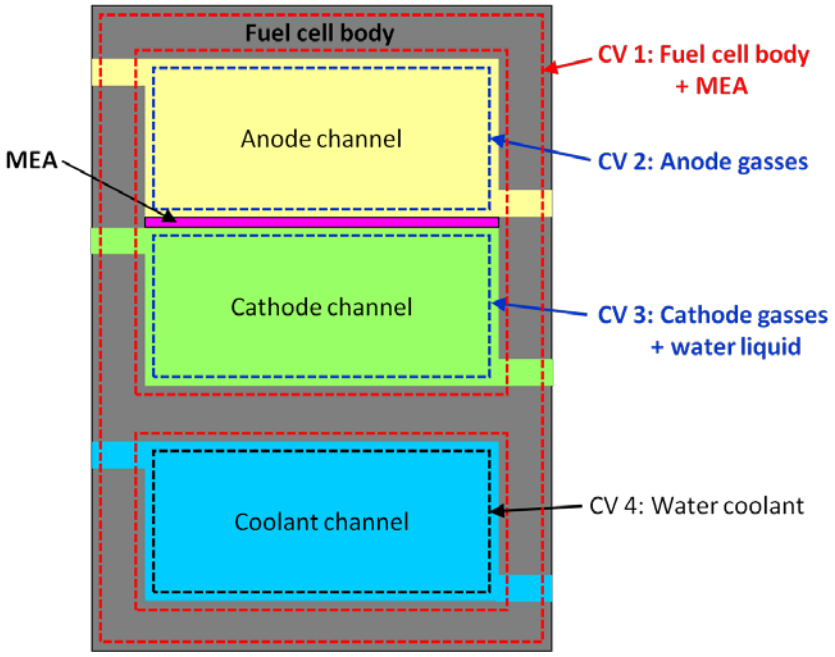

Figure 2.2: Defining control volumes (CVs) of a single cell of the fuel cell model.

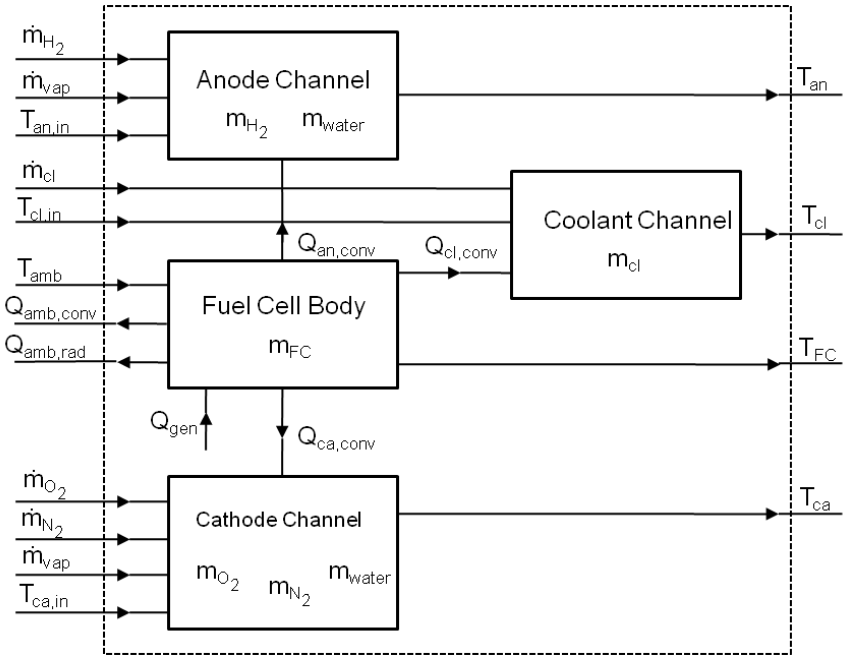

Figure 2.3: Thermal model block diagram.

Figure 2.3 shows the thermal model block diagram which contains the four interacting sub–models where each sub–model represents a control volume accordingly. The arrows signify the variables as inputs or outputs of the control volumes.

The outputs of this system are the outlet mass flow rate and temperature for each control volume. All the gasses are assumed to follow the ideal gas law. The temperature of each control volume is calculated based on the conservation of energy and mass applied to each control volume, represented by the following governing equation.

$$\frac{dU}{dt} = Q_{net} + W_{net} + \sum \dot{m}_{in} h_{in} - \sum \dot{m}_{out} h_{out} \tag{2.1}$$

Equation 2.1 states that the time rate of change of internal energy in a control volume is equal to the sum of the net heat transfer, the net work done onto and by the system, and the sum of the reaction enthalpies associated with the input and output of the mass flow rates. The first law representation for the fuel cell body and each of the channels is explained in the following sections.

2.3.1 FUEL CELL BODY CONTROL VOLUME

The solid fuel cell body and the MEA are combined into a control volume and are assumed to be of uniform temperature. Only the graphite mass of the fuel cell body is considered in the calculation since the MEA mass is negligibly small compared to that of the fuel cell body. Figure 2.4 shows the fuel cell body block diagram for calculation.

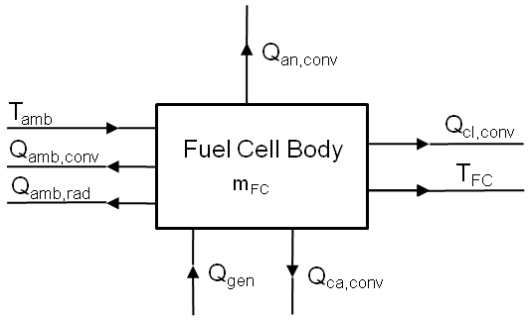

Figure 2.4: Fuel cell body block diagram.

The change in temperature of the fuel cell depends on the heat generated from the chemical reaction (Q_{gen}), the heat transferred by mass convection in the anode ($Q_{an,conv}$), cathode ($Q_{ca,conv}$), coolant channel ($Q_{cl,conv}$), and heat transferred from the body surface to the environment by convection ($Q_{amb,conv}$) and radiation ($Q_{amb,rad}$). Applying Equation 2.1, the fuel cell body control volume results as follow.

$$m_{FC}\, C_{FC}\, \frac{dT_{FC}}{dt} = Q_{gen} - Q_{an,conv} - Q_{ca,conv} - Q_{cl,conv} - Q_{amb,conv} - Q_{amb,rad} \quad (2.2)$$

Using Equation 2.2, the change of the fuel cell body temperature can be estimated given the sum of the heat generation and the heat transfer terms on the right hand side of the equation. Potential and kinetic energies of the mass flows are neglected since they are small compared to the other types of energies.

The heat loss from the fuel cell to the ambient by convection is:

$$Q_{amb,conv} = h_{c_{FC,amb}}\, A_{FC,amb}\, (T_{SFC} - T_{amb}) \quad (2.3)$$

In the above equation, T_{SFC} is the fuel cell surface body temperature. The heat coefficient of convection, $h_{c_{FC,amb}}$, is based on the air property, the average surrounding air flow rate of convection on vertical and horizontal surfaces of the fuel cell. The average airflow is approximated 0.7 m/sec, created by the small fan placed on the hood of

the fuel cell station. The ambient room temperature was measured 23°C. To estimate the convection coefficient, first the Reynolds (Re) is calculated to find the type of fluid flow, as follows [59].

$$Re = \frac{VL}{\upsilon} \tag{2.4}$$

In the above equations, V is the velocity of the fluid, L is the length of the fuel cell body surface parallel to the air flow direction, and υ is the kinematic viscosity. At 300K, the kinematic viscosity of air is 15.66e–6 m^2/sec [59]. Substituting the numbers, the Reynolds number in Equation 2.4 is:

$$Re = \frac{\left(0.7\ \frac{m}{sec}\right)(0.127\ m)}{15.66e-6\ \frac{m^2}{sec}} = 5{,}676.9$$

Since the Reynolds number is below 50,000 which is the transition from laminar to turbulent flow, the ambient air flow is determined to be laminar [59].

The convection coefficient is related to the conduction coefficient by a Nusselt number. For fluid flow on a flat surface, the average Nusselt ($\overline{Nu}$) number is calculated as follows [59].

$$\overline{Nu} = \frac{\overline{h_c}\,L}{k} = 0.664\ Re_L^{1/2}\ Pr^{1/3}; \qquad \text{for } Pr > 0.5 \tag{2.5}$$

where $\overline{h_c}$, k, and Pr are the average convection coefficient, conduction coefficient, and Prandtl number respectively. At 300K, the air conduction coefficient is 0.0267 W/m K, and the Prandtl number is 0.69 [59]. Substituting the numbers into Equation 2.5, we have:

$$\overline{Nu} = 0.664\left(5{,}676.9^{1/2}\right)\left(0.69^{1/3}\right) = 44.21$$

Thus, the heat convection coefficient of ambient air is:

$$\overline{h_{c_{FC,amb}}} = \frac{44.21\left(0.0267\frac{W}{m\,K}\right)}{0.127m} = 9.3\ \frac{W}{m^2\,K}$$

The heat loss from the fuel cell to the ambient by radiation in Equation 2.2 is presented as:

$$Q_{amb,rad} = \varepsilon\ \sigma\ A_{FC,amb}\ (T_{SFC}^4 - T_{amb}^4) \tag{2.6}$$

In the above equation, T_{SFC} is the fuel cell surface body temperature, the same as in Equation 2.3. The emissivity ε was determined to be 0.9 for carbon graphite material [53]. σ is the Stefan–Boltzmann constant and $A_{FC,amb}$ is the fuel cell body surface area that is exposed to the ambient air.

The heat generation term takes the following form.

$$Q_{gen} = (E - V_{fc}) \cdot i \tag{2.7}$$

In Equation 2.7, E is the ideal voltage as related to the heating value of the reactants and V_{fc} is the actual fuel cell voltage. The remaining energy terms in Equation 2.2 and the voltage model are presented in the following sub sections.

2.3.2 ANODE CONTROL VOLUME

The energy flow in the anode control volume consists of the inlet and outlet flow enthalpies, along with the heat convection between the anode channel surface and the flowing gases. The inputs to the model, shown in Figure 2.5, consist of hydrogen and vapor mass flows, and inlet anode gas temperature.

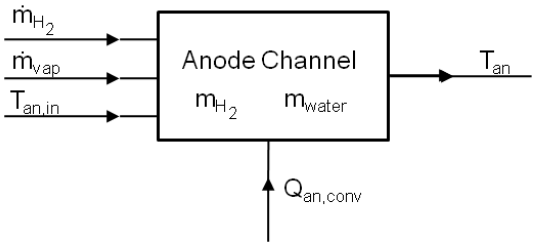

Figure 2.5: Anode channel block diagram.

The energy balance in the anode control volume is:

$$\frac{dU_{an}}{dt} = Q_{an,conv} + H_{an,in} - H_{an,out} \tag{2.8}$$

The left hand side of Equation 2.8 is expanded as

$$\frac{dU_{an}}{dt} = \left(\sum \frac{dm_{an}}{dt} C_{v_{an}}\right) T_{an} + \left(\sum m_{an} C_{v_{an}}\right) \frac{dT_{an}}{dt}$$

$$= \left(\dot{m}_{H_2} C_{v_{H_2}} + \dot{m}_{vap} C_{v_{vap}} + \dot{m}_{liq} C_{liq}\right) T_{an}$$

$$+ \left(m_{H_2} C_{v_{H_2}} + m_{vap} C_{v_{vap}} + m_{liq} C_{liq}\right) \frac{dT_{an}}{dt} \tag{2.9}$$

Equation 2.9 represents the change of internal energy in the anode control volume that depends on the time rate of change of masses at a constant temperature and the time rate of change of temperature at a constant mass. The masses in the anode channel consist of hydrogen, water vapor, and potentially liquid water. Specific heats of the gas species are assumed constant at a constant volume since the pressure changes during the transient response.

On the right hand side of Equation 2.8, the first term is the heat transferred by convection between gases in the anode channel and the fuel cell body. The temperature inside the anode channel is assumed to have the same temperature at the anode outlet. The heat transferred by convection is

$$Q_{an,conv} = h_{c_{an,FC}} A_{an}(T_{FC} - T_{an}) \tag{2.10}$$

The heat convection coefficient for the flow in the anode channel is obtained from the Nusselt number. Based on the anode channel dimensions provided in the Appendix B and the average anode gas flow rate of ~3 liter/min from the experimental data, the flow is laminar and fully developed. This is indicated by the Reynolds number which is below 2300 from the calculations in the following [59].

The Reynolds number for fluid flow in a pipe is:

$$Re_D = \frac{\rho\, V D_h}{\mu} = \frac{\rho\, Q D_h}{\mu\, A_C} \tag{2.11}$$

In the above equation, V is the fluid velocity which equals to anode gas flow rate Q divided by anode channel cross section A_C. D_h is the hydraulic diameter, μ is the dynamic viscosity. ρ is the humid hydrogen gas that enters the anode channel and estimated as:

$$\rho_{H_2,vap} = \frac{p}{R_{H_2}\, T}\left(\frac{1+\omega}{1+\omega\frac{R_v}{R_{H_2}}}\right) \tag{2.12}$$

where R_{H_2} is the hydrogen gas constant, R_v is the vapor gas constant, p is the gas pressure, T is the gas temperature, and ω is the humidity ratio.

$$\omega = \frac{M_v\, p_v}{M_{H_2}\, p_{H_2}} \tag{2.13}$$

M_v in Equation 2.13 is the vapor molar mass, M_{H_2} is the hydrogen molar mass, p_v is the vapor partial pressure, p_{H_2} is the hydrogen partial pressure. These partial pressures are approximated as follows.

$$p_v = \emptyset_{an}\left(p_{sat}\,(@T = 353K)\right) = 0.8\,(38{,}300\,Pa) = 30{,}640\,Pa \tag{2.14}$$

$$p_{H_2} = p_{an} - p_v = 151{,}855\ Pa - 30{,}640\ Pa = 121{,}215\ Pa \tag{2.15}$$

$\emptyset_{an}$ is the relative humidity and p_{an} is the anode channel pressure which is averaged from the experimental data. Substituting the values into Equation 2.13, we have:

$$\omega = \frac{\left(18.02e-3\ \frac{kg}{mol}\right)(30{,}640\ Pa)}{\left(2.016e-3\ \frac{kg}{mol}\right)(121{,}215\ Pa)} = 2.26$$

Substituting the numbers from Equations 2.13, 2.14, and 2.15 into Equation 2.12, one gets:

$$\rho_{H_2,vap} = \frac{151{,}855\ Pa}{4.1243e3\ \frac{J}{kg\ K}(353K)}\left(\frac{1+2.26}{1+2.26\frac{461.5\frac{J}{kg\ K}}{4.1243e3\ \frac{J}{kg\ K}}}\right) = 0.27\ \frac{kg}{m^3}$$

Referring back to Equation 2.11, the dynamic viscosity is approximated as the average that of hydrogen gas and saturated steam at 350K. The dynamic viscosity of hydrogen gas at 350K is 9.86e–6 kg/m.sec and for the saturated steam is 11.1e–6 kg/m.sec [59]. Thus the average dynamic viscosity of anode gas is determined to be 10.48e–6 kg/m.sec. The anode hydraulic diameter is:

$$D_{h_{an,FC}} = 4\frac{A_C}{P} = \frac{4(0.864\ mm \text{ x } 0.56\ mm)}{2(0.864\ mm + 0.56\ mm)} = 0.68\ mm \tag{2.16}$$

where A_c and P in are the cross sectional area and perimeter of the anode channel respectively.

Substituting the numbers into Equation 2.11, the Reynolds number is:

$$Re_D = \frac{0.27e-9\ \frac{kg}{mm^3}\ (3e6\ mm^3/\ 60\ sec)(0.68\ mm)}{\left(10.48e-9\ \frac{kg}{mm.sec}\right)(0.864\ mm \text{ x } 0.56\ mm)} = 1{,}810.4$$

The heat conduction coefficient is estimated from data in Table 2.1 and assumed to be constant during the fuel cell operation given the relatively small changes of the coefficient in the range of the fuel cell operation pressure and temperature. In the anode control volume, the heat conduction coefficient for hydrogen gas is assumed since it is the main constituent in the anode channel and one order larger in magnitude than that of water vapor.

Species	Conduction Coefficients (W/m K)
H_2O (vapor)	0.023
N_2	0.0293
H_2	0.211
O_2	0.0296

Table 2.1: Heat conduction coefficients at 350K [58].

The Nusselt number for laminar fluid flows in rectangular pipes is 2.98 with the assumption of constant surface temperature [58, 59].

$$Nu_D = \frac{h_{c_{an,FC}} D_{h_{an,FC}}}{k_{an}} \approx 2.98 \tag{2.17}$$

Based on that, the anode convection coefficient is:

$$h_{c_{an,FC}} = \frac{Nu_D \ k_{an}}{D_{h_{an,FC}}} = \frac{2.98 \left(0.211 \ \frac{\text{W}}{\text{m K}}\right)}{0.68 \text{ e} - 3 \text{ m}} = 924.6 \ \frac{W}{m^2 \ K} \tag{2.18}$$

Referring back to Equation 2.8 and assuming the pressure is constant, the enthalpies entering the anode control volume consist of the hydrogen and vapor masses

from the anode inlet, as well as the vapor and liquid masses that cross the membrane are given by

$$H_{an,in} = \left(\dot{m}_{H_2,in} C_{p_{H_2}} + \dot{m}_{vap,in} C_{p_{vap}}\right) T_{an,in} + \left(\dot{m}_{vap,in,MEA} C_{v_{vap}} + \dot{m}_{liq,in,MEA} C_{liq}\right) T_{an} \quad (2.19)$$

The enthalpies out of the system are of similar form to that of the inlet and it includes the reacted hydrogen mass as well

$$H_{an,out} = \left(\dot{m}_{H_2,out} C_{v_{H_2}} + \dot{m}_{vap,out} C_{v_{vap}}\right) T_{an,out} + \left(\dot{m}_{H_2,reac} C_{v_{H_2}} + \dot{m}_{vap,out,MEA} C_{v_{vap}} + \dot{m}_{liq,out,MEA} C_{liq}\right) T_{an} \quad (2.20)$$

The hydrogen mass consumed in the reaction is calculated from the stack current as follows

$$\dot{m}_{H_2,reac} = M_{H_2} n_{cells} \frac{I_{st}}{2F} \quad (2.21)$$

M_{H_2} in the above equation denotes the hydrogen molecular masses in kg/mol, n_{cells} is the number of cells in the stack, and *F* is the Faraday constant.

2.3.3 CATHODE CONTROL VOLUME

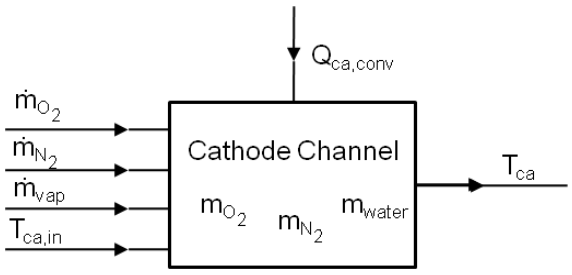

Figure 2.6: Cathode channel block diagram.

Figure 2.6 shows the block diagram of the cathode channel control volume. The cathode channel consists of air (oxygen and nitrogen), water vapor and potentially liquid water that forms due to condensation. The energy balance in the cathode control volume is

$$\frac{dU_{Ca}}{dt} = Q_{ca,conv} + H_{ca,in} - H_{ca,out} + Q_{latent} \tag{2.22}$$

The left hand side of Equation 2.22 is expanded as

$$\begin{aligned}\frac{dU_{ca}}{dt} &= \left(\sum \frac{dm_{ca}}{dt} C_{v_{ca}}\right) T_{ca} + \left(\sum m_{ca} C_{v_{ca}}\right) \frac{dT_{ca}}{dt} \\ &= \left(\dot{m}_{O_2} C_{v_{O_2}} + \dot{m}_{N_2} C_{v_{N_2}} + \dot{m}_{vap} C_{v_{vap}} + \dot{m}_{liq} C_{liq}\right) T_{ca} \\ &\quad + \left(m_{O_2} C_{v_{O_2}} + m_{N_2} C_{v_{N_2}} + m_{vap} C_{v_{vap}} + m_{liq} C_{liq}\right) \frac{dT_{ca}}{dt}\end{aligned} \tag{2.23}$$

The cathode flow enthalpies are expressed by

$$\begin{aligned}H_{ca,in} &= \left(\dot{m}_{O_2,in} C_{v_{O_2}} + \dot{m}_{N_2,in} C_{v_{N_2}} + \dot{m}_{vap,in} C_{v_{vap}}\right) T_{ca,in} \\ &\quad + \left(\dot{m}_{vap,in,MEA} C_{v_{vap}} + \dot{m}_{vap,gen} C_{v_{vap}} + \dot{m}_{liq,in,MEA} C_{liq}\right) T_{ca}\end{aligned} \tag{2.24}$$

$$\begin{aligned}H_{ca,out} &= \left(\dot{m}_{O_2,out} C_{v_{O_2}} + \dot{m}_{N_2,out} C_{v_{N_2}} + \dot{m}_{vap,out} C_{v_{vap}}\right. \\ &\quad \left. + \dot{m}_{liq,out} C_{liq}\right) T_{ca,out} + \left(\dot{m}_{O_2,reac} C_{v_{O_2}} + \dot{m}_{liq,out,MEA} C_{liq}\right) T_{Ca}\end{aligned} \tag{2.25}$$

The oxygen mass consumed and water produced during the reaction are calculated from the stack current input.

$$\dot{m}_{O_2 reac} = M_{O_2} n_{cells} \frac{I_{st}}{4F} \tag{2.26}$$

$$\dot{m}_{H_2O_{reac}} = M_{H_2O} n_{cells} \frac{I_{st}}{2F} \tag{2.27}$$

The heat transferred by convection between the fuel cell body and cathode gases is calculated similarly to that of the anode case.

$$Q_{ca,conv} = h_{c_{ca,FC}} A_{ca} (T_{FC} - T_{ca}) \tag{2.28}$$

The heat convection coefficient of the gas in the cathode channel is calculated in a similar manner as the heat convection coefficient of the gas in the anode channel. Firstly, the gas density entering the cathode channel is estimated in a similar way as Equation 2.12. The cathode gas flow rate averaged from the experimental data is ~15 liter/min. The humid air density is:

$$\rho_{air,vap} = \frac{p}{R_{air}\, T} \left(\frac{1+\omega}{1+\omega \frac{R_v}{R_{air}}} \right) \tag{2.29}$$

In the above equation, R_{air} is the air gas constant, R_v is the vapor gas constant, p is the cathode gas pressure, and T is the cathode gas temperature. ω is the humidity ratio which is calculated:

$$\omega = \frac{M_v\, p_v}{M_{air}\, p_{air}} = \frac{\left(18.02e-3\ \frac{kg}{mol}\right)(30{,}640\ Pa)}{\left(28.84e-3\ \frac{kg}{mol}\right)(166{,}685\ Pa)} = 0.11 \tag{2.30}$$

M_v in Equation 2.30 is the vapor molar mass, M_{air} is the air molar mass, p_v is the vapor partial pressure, p_{air} is the hydrogen partial pressure. These partial pressures are approximated as follows.

$$p_v = \emptyset_{ca} \left(p_{sat}\ (@T = 353K)\right) = 0.8\ (38{,}300\ Pa) = 30{,}640\ Pa \tag{2.31}$$

$$p_{air} = p_{ca} - p_v = 197{,}325\ Pa - 30{,}640\ Pa = 166{,}685\ Pa \tag{2.32}$$

where $\emptyset_{ca}$ is the cathode relative humidity and p_{ca} is the cathode channel pressure which is averaged from the experimental data.

Substituting the numbers from Equations 2.30, 2.31, and 2.32 into Equation 2.29, one gets:

$$\rho_{air,vap} = \frac{197{,}325\ Pa}{286.9\ \frac{J}{kg\ K}(353K)}\left(\frac{1+0.11}{1+0.11\frac{461.5\ \frac{J}{kg\ K}}{286.9\ \frac{J}{kg\ K}}}\right) = 1.84\ \frac{kg}{m^3}$$

The dynamic viscosity of cathode gas is approximated as the average of air and saturated steam at 350K. The dynamics viscosity of air at 353K is 20.5e–6 kg/m.sec and the saturated steam is 11.1e–6 kg/m.sec [59]. These bring the average of 15.8e–6 kg/m.sec. The cathode channel hydraulic diameter is:

$$D_{h_{ca,FC}} = 4\frac{A_C}{P} = \frac{4(1.5748\ mm \text{ x } 1.27\ mm)}{2(1.5748\ mm + \ 1.27\ mm)} = 1.41\ mm \tag{2.33}$$

where A_c and P are the cross sectional area and perimeter of the cathode channel respectively.

Identical to Equation 2.11, the Reynolds number for cathode gas is calculated as:

$$Re_D = \frac{\rho\ Q D_h}{\mu\ A_C} \tag{2.34}$$

Substituting the numbers, one gets:

$$Re_D = \frac{1.84e-9\ \frac{kg}{mm^3}\ (15e6\ mm^3/\ 60\ sec)(1.41\ mm)}{\left(15.8e-9\ \frac{kg}{mm\ sec}\right)(1.5748\ mm \text{ x } 1.27\ mm)} = 20{,}525$$

The cathode Reynolds number is greater than 10,000 which indicate that the gas flow is fully developed turbulence. For turbulent flow, the friction factor takes into account. Assuming the wall is smooth, the friction factor is [59]:

$$f = (0.790 \ln Re_D - 1.64)^{-2}; \qquad \text{for } 10^4 < Re_D < 5\text{x}10^6 \tag{2.35}$$

Substituting the Reynolds number, one gets:

$$f = (0.790\ (\ln 20{,}525) - 1.64)^{-2} = 0.026$$

Hence, the cathode Nusselt number is calculated as follows [59].

$$Nu_D = \frac{(f/8)(Re_D - 1000)\ Pr}{1 + 12.7(f/8)^{1/2}(Pr^{2/3} - 1)}; \qquad \text{for } 3000 < Re_D < 10^6 \tag{2.36}$$

The Prandtl numbers of air and saturated steam at 350K are 0.69 and 0.94 respectively and the average is 0.815 [59]. Substituting the friction number and the Prandtl number, the Nusselt number is:

$$Nu_D = \frac{(0.026/8)(20{,}525 - 1000)\ 0.815}{1 + 12.7(0.026/8)^{1/2}(0.815^{2/3} - 1)} = 57$$

While the gas in the cathode is a mixture of many species, the conduction coefficient is approximated to be that of nitrogen, given that it is the major constituent in the gas, and conduction coefficients for the other prevalent species are similarly close.

Based on the above results, the cathode gas convection coefficient is:

$$h_{c_{ca,FC}} = \frac{Nu_D\ k_{ca}}{D_{h_{ca,FC}}} = \frac{(57)\left(0.0293\ \frac{W}{m\,K}\right)}{1.41e-3\ m} = 1184.5\ \frac{W}{m^2K} \tag{2.37}$$

Assuming that the water produced from the reaction is in the vapor form and when the vapor reaches saturation, the water vapor condenses into liquid which releases heat. The latent heat for the water phase change is

$$Q_{latent} = \left(\dot{m}_{vap,in} + \dot{m}_{vap,gen} + \dot{m}_{vap,in,MEA} - \dot{m}_{vap,out}\right)h_{fg} \quad (2.38)$$

h_{fg} equals to 2260 kJ/kg, is the latent heat of vaporization of water and a function of temperature. Here, it is assumed constant since the change is small around the fuel cell operating temperature.

2.3.4 COOLANT CONTROL VOLUME

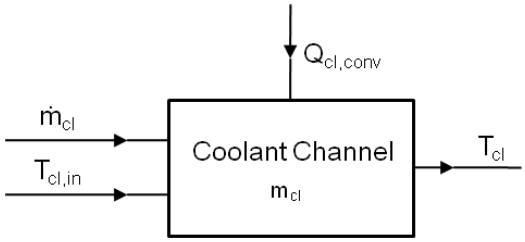

Figure 2.7: Coolant channel block diagram.

Liquid water is used as the coolant in this fuel cell system. Similar to anode and cathode channels, figure 2.7 shows the inputs and output for the calculation. The energy balance of the coolant control volume is given by

$$\frac{dU_{cl}}{dt} = Q_{cl,conv} + H_{cl,in} - H_{cl,out} \quad (2.39)$$

The first term on the left hand of Equation (2.39) side is elaborated as

$$\frac{dU_{cl}}{dt} = \frac{dm_{cl}}{dt} C_{liq} T_{cl} + m_{cl} C_{liq} \frac{dT_{cl}}{dt} \quad (2.40)$$

The coolant temperature in the fuel cell body is assumed as the outlet coolant temperatures. In Equation 2.39, the heat transferred by convection is

$$Q_{cl,conv} = h_{cl}\, A_{cl}\, (T_{FC} - T_{cl}) \quad (2.41)$$

Similar to calculating the convection coefficients of anode and cathode gases, the Reynolds number for the liquid coolant flow in the coolant channel is:

$$Re_D = \frac{\rho\, Q D_h}{\mu\, A_C} \tag{2.42}$$

The density of liquid water is 997 kg/m^3, the average coolant flow is ~0.67 liter/min from the experimental data, and the dynamic viscosity of liquid water at 350K is 3.79e–4 kg/m.sec. The coolant channel hydraulic diameter is:

$$D_{h_{cl,FC}} = 4\frac{A_C}{P} = \frac{4(2.54\ mm \text{ x } 1.27\ mm)}{2(2.54\ mm + \ 1.27\ mm)} = 1.69\ mm \tag{2.43}$$

where A_c and P are the cross sectional area and perimeter of the coolant channel respectively.

Substituting the numbers into equation 2.43, one gets:

$$Re_D = \frac{997e-9\ \frac{kg}{mm^3}\ (0.67e6\ mm^3/\ 60\ sec)(1.69\ mm)}{\left(3.79e-7\ \frac{kg}{mm.sec}\right)(2.54\ mm \text{ x } 1.27\ mm)} = 15{,}390$$

The cathode Reynolds number is greater than 10,000 which indicate that the gas flow is fully developed turbulence. For turbulent flow, the friction factor takes into account. Assuming the wall is smooth, the friction factor is [59]:

$$f = (0.790 \ln Re_D - 1.64)^{-2}; \qquad \text{for } 10^4 < \ Re_D < 5\text{x}10^6 \tag{2.44}$$

Substituting the Reynolds number, one gets:

$$f = (0.790\ (\ln 15{,}390) - 1.64)^{-2} = 0.028$$

Hence, the cathode Nusselt number is calculated as follows [59].

$$Nu_D = \frac{(f/8)(Re_D - 1000)\ Pr}{1 + 12.7(f/8)^{1/2}(Pr^{2/3} - 1)}; \qquad \text{for } 3000 < \ Re_D < 10^6 \tag{2.45}$$

The Prandtl numbers of liquid water at 350K is 2.4 [59]. Substituting the friction number and the Prandtl number, the Nusselt number is:

$$Nu_D = \frac{(0.028/8)(15{,}390 - 1000)\ 2.4}{1 + 12.7(0.028/8)^{1/2}(2.4^{2/3} - 1)} = 75.8$$

The conduction coefficient of liquid water at 350K is 0.669 W/m K [59]. Based on the above results, the coolant convection coefficient is:

$$h_{c_{ca,FC}} = \frac{Nu_D\ k_{ca}}{D_{h_{ca,FC}}} = \frac{(75.8)\left(0.669\ \frac{W}{m\,K}\right)}{1.69e-3\ m} = 30{,}006\ \frac{W}{m^2K} \tag{2.46}$$

The inlet and outlet flow enthalpies in Equation 2.39 are defined as follows.

$$H_{cl,in} = \dot{m}_{cl} C_{liq} T_{cl,in} \tag{2.47}$$

$$H_{cl,out} = \dot{m}_{cl} C_{liq} T_{cl,out} \tag{2.48}$$

2.3.5 STACK VOLTAGE MODEL

For two electrons to move around an external load circuit from the reaction of a single hydrogen molecule, the electrical work done is [60, 61]

$$W_{elec} = -2FE \tag{2.49}$$

Ideally, all of the energy released from the reaction, Δh_f, is converted into electrical energy.

$$\Delta h_f = -2FE \tag{2.50}$$

The reaction product of hydrogen and oxygen molecules can be in the form of water vapor or liquid water. The value of E in Equation 2.50 equals to 1.25 Volts, also

known as Lower Heating Value (LHV), if the water vapor is the product and the value of E equals to 1.48 Volts, also known as Higher Heating Value (HHV), if the liquid water is the product [62].

From thermodynamics, the available energy for work is equal to the change in Gibbs free energy *(*Δg) between the reactants and products.

$$\Delta g = -2FV_{ideal} \tag{2.51}$$

The ideal voltage is achievable if all of the chemical energies are converted to electrical work.

$$V_{ideal} = \frac{-\Delta g}{2F} \tag{2.52}$$

The Gibbs free energy in Equation 2.51 for hydrogen and oxygen to form water is in the form of

$$\Delta g = \Delta g_f^0 + (T_{memb} - T_0)\Delta S^0 - \bar{R}T_{memb} ln\left[\frac{p_{H_2} p_{O_2}^{1/2}}{p_{H_2O}}\right] \tag{2.53}$$

The Gibbs energy of formation varies from the standard state (25°C and 1 atm) value, Δg_f^0, with temperature and entropy changes as well as the concentration differences between the reactants and products. Given that the expected temperature change is relatively small, the entropy change is taken to be a standard value, ΔS^0 [60]. ΔS^0 is selected to be -44.43 J/mol K. Using values of standard state entropy change, the ideal voltage is given by the following expression.

$$V_{ideal} = 1.229 - 0.85 \times 10^{-3}(T_{mb} - 298.15) + 4.3085 \times 10^{-5} T_{mb}\left[ln(p_{H_2}) + \tfrac{1}{2} ln(p_{O_2})\right] \tag{2.54}$$

The 1.229 Volts in the above equation is the reference potential and equals to the standard state Gibbs formation energy for pure liquid water divided by twice the Faraday's number. In Equation 2.53, the pure liquid water assumption makes the partial pressure of the water equal to unity and this term is dropped from the equation.

This ideal voltage is unattainable due to losses inherent to the system, including activation losses, ohmic losses, and concentration losses. Empirical quantifications of these losses are explained in Reference 60 and are summarized in the following subsections.

2.3.5.1 Activation Loss

Activation losses arise due to the energy required to drive the chemical reactions at the anode and cathode. A simple model used to account from has the following form [60].

$$V_{act} = V_0 + V_a\left(1 - e^{-c_1 \cdot i}\right) \tag{2.55}$$

where V_0, V_a and c_1 depend on the oxygen partial pressure and temperature. These values are obtained from a nonlinear regression of experimental data [60]. The model is applied for all current ranges at operating temperature and pressure. The regression results are:

$$V_0 = 0.279 - 8.5\,e-4(T_{FC} - 298.15) + 4.308e-5\,T_{FC}\left[ln\left(\frac{p_{ca} - p_{sat}}{1.01325}\right) + \frac{1}{2}ln\left(\frac{0.1173(p_{ca} - p_{sat})}{1.01325}\right)\right] \tag{2.56}$$

$$V_a = (-1.618e-5\,T_{FC} + 1.618e-2)\left(\frac{p_{O_2}}{0.1173} + p_{sat}\right)^2 + (1.8e-4\,T_{FC} - 0.166)\left(\frac{p_{O_2}}{0.1173} + p_{sat}\right) + (-5.8e-4\,T_{FC} + 0.5736) \tag{2.57}$$

And the constant c_1 equals to 10.

2.3.5.2 Ohmic Loss

Ohmic losses result from voltage drops due to the resistance of the membrane to proton transfer and the electrical resistance of the electrode and collector plate to electron transfer [60].

$$V_{ohm} = i \cdot R_{ohm} \tag{2.58}$$

where R_{ohm}, the membrane's internal electrical resistance, is the ratio of the membrane's thickness to its electrical conductivity.

$$R_{ohm} = \frac{t_m}{\sigma_m} \tag{2.59}$$

Membrane conductivity is a function of the membrane water content and is found using the following empirical relations.

$$\sigma_m = b_1 exp\left(b_2\left(\frac{1}{303} - \frac{1}{T_{fc}}\right)\right) \tag{2.60}$$

$$b_1 = (b_{11}\lambda_m - b_{12}) \tag{2.61}$$

where b_2, b_{11}, and b_{12} are empirically determined constants specific to the membrane being used. The membrane water content, λ_m, is a function of the activity also known as relative humidity, a_m, in the membrane and is given by the following empirical equation.

$$\lambda_m = \begin{cases} 0.043 + 17.81a_m - 39.85a_m^2 + 36.00a_m^3; & a_m \leq 1 \\ 14 + 1.4(a_m - 1) \quad ; & a_m > 1 \end{cases} \tag{2.62}$$

2.3.5.3 Concentration Loss

Concentration losses, due to changes in reactant concentrations as the reaction progresses, can be modeled as [60]

$$V_{conc} = i\left(c_2 \frac{i}{i_{max}}\right)^{c_3} \tag{2.63}$$

where c_2, c_3, and i_{max} are empirical regressions of experimental data that depend on temperature and partial pressures of the reactants.

As spatial temperature variations are neglected, all cells are assumed to have the same voltage, and the total stack voltage is found by simply multiplying the voltage for a single cell by the number of cells. Accounting for all of the voltage losses, the fuel cell voltage is modeled as

$$V_{fc} = (V_{ideal} - V_{act} - V_{ohm} - V_{conc}\ ) \times n_{cells} \tag{2.64}$$

Based on the above equations that describe the heat and mass transfer, electrochemical reaction and thermodynamics of the stack system, a dynamic thermal and voltage model was developed in the Matlab/Simulink environment. The Matlab/Simulink representations are provided in Appendix E.

2.4 THERMAL DYNAMICS MODEL SUMMARY

The developed thermal model is summarized in the following. Four control volumes are employed to represent the dynamics of the temperatures of the anode, cathode, fuel cell body and the coolant. Each control volume is represented with a first order equation, making the thermal system a fourth order system. The four first order equations are:

$$\frac{dT_{FC}}{dt} = \frac{1}{m_{FC}\, C_{FC}} \big(Q_{gen} - Q_{an,conv} - Q_{ca,conv} - Q_{cl,conv} - Q_{amb,conv} - Q_{amb,rad}\big)$$

$$\frac{dT_{an}}{dt} = \left(\frac{1}{m_{H_2}C_{v_{H_2}} + m_{vap}C_{v_{vap}} + m_{liq}C_{liq}}\right)\Big[\big(Q_{an,conv} + H_{an,in} - H_{an,out} + Q_{latent} - \big(\dot{m}_{H_2}C_{v_{H_2}} + \dot{m}_{vap}C_{v_{vap}} + \dot{m}_{liq}C_{liq}\big)T_{an}\Big]$$

$$\frac{dT_{ca}}{dt} = \left(\frac{1}{m_{O_2}C_{v_{O_2}} + m_{N_2}C_{v_{N_2}} + m_{vap}C_{v_{vap}} + m_{liq}C_{liq}}\right)\Big[\big(Q_{ca,conv} + H_{ca,in} - H_{ca,out} + Q_{latent} - \big(\dot{m}_{O_2}C_{v_{O_2}} + \dot{m}_{N_2}C_{v_{N_2}} + \dot{m}_{vap}C_{v_{vap}} + \dot{m}_{liq}C_{liq}\big)T_{ca}\Big]$$

$$\frac{dT_{cl}}{dt} = \frac{1}{m_{cl}C_{liq}}\left[Q_{ca,conv} + H_{ca,in} - H_{ca,out} + Q_{latent} - \frac{dm_{cl}}{dt}C_{liq}T_{cl}\right] \qquad (2.65)$$

Chapter 3: Experimental Setup and Model Calibration and Validation

3.1 EXPERIMENTAL SETUP

The dynamics thermal model was validated by experiments utilizing a PEM fuel cell stack that consisted of 30 cells. Each cell employed a five–layer Membrane Electrolyte Assembly (MEA) with a surface area of approximately 50 cm^2. The polymer membrane used was Nafion 212 with the thickness of 50 μm. The catalyst layers have 0.4 mg/cm^2 of platinum loadings supported in carbon black powder on both the anode and cathode sides. The GDL used is a sheet of hydrophobic Toray 060 carbon paper with a thickness of 190 μm. The flow fields are machined graphite plates having serpentine flow patterns with the anode and cathode flow field passages in a cross flow configuration. The hydrogen of 99.999% purity was used for the experiments.

The tests were performed on the fuel cell test station as shown in Figure 3.1. The station supplies reactant gases and de–ionized liquid water coolant with controlled flow rate, temperature and pressure. The temperature sensors are J – type thermocouples with working temperature range from 0 to 760°C with limits of error of 1.1°C. The fuel cell station also provides humidification of the gases in the anode and cathode lines. Inlet and outlet variables were captured by the station sensors, and monitored and recorded by a computer. Operation of the anode outlet can either be open– or dead–ended flow with a time controlled intermittent purge. Open–ended operation was used for this set of experiments. The schematic diagram of the fuel cell connected to the station is shown in Figure 3.2. The operation parameters of the experiments are listed in Table 3.1.

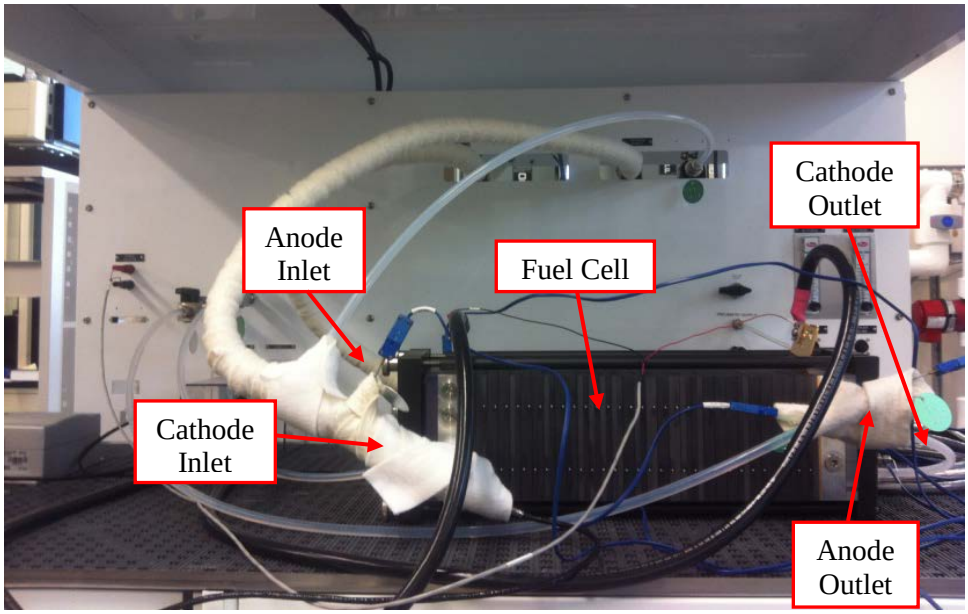

Figure 3.1: Fuel cell experimental test station.

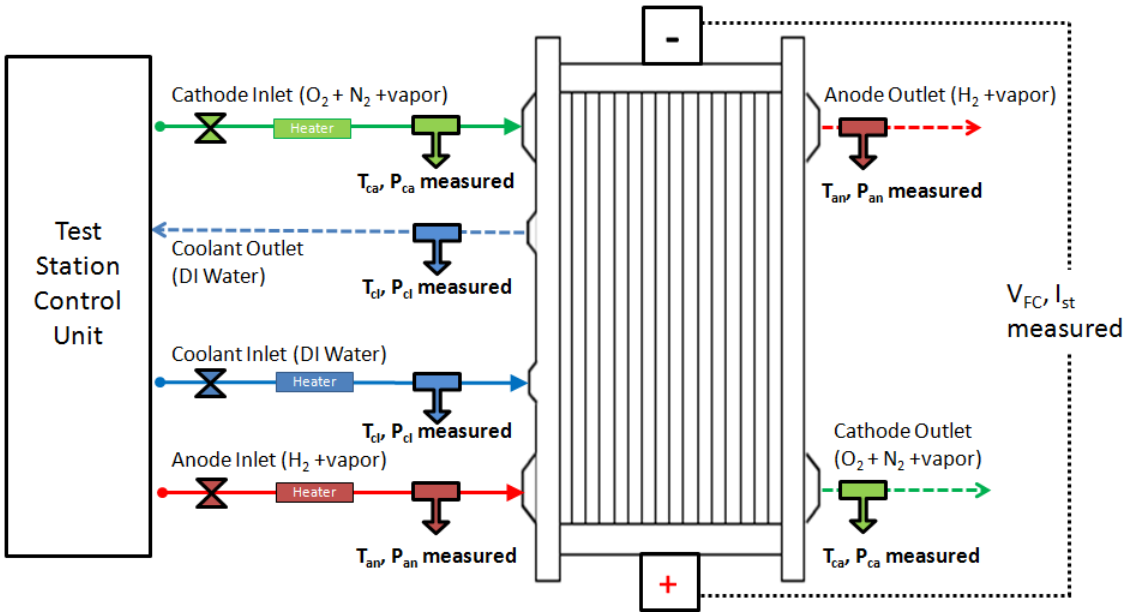

Figure 3.2: Fuel cell stack test station schematic.

Input Name	Symbol	Set Values	Units
Anode Inlet Temperature	$T_{an,in}$	348	K
Cathode Inlet Temperature	$T_{ca,in}$	348	K
Anode Inlet Stack Gas Flow	$\dot{v}_{an,in}$	3	lpm
Cathode Inlet Stack Gas Flow	$\dot{v}_{ca,in}$	15	lpm
Coolant Inlet Flow	$\dot{v}_{cl,in}$	0.6	lpm
Anode Inlet Relative Humidity	$\emptyset_{an,in}$	80	%
Cathode Inlet Relative Humidity	$\emptyset_{ca,in}$	80	%

Table 3.1: Input set values of the test experiment.

Two profiles of current load were run during the test. They are polarization and alternating step current load profiles shown in Figure 3.3 below. Each current load profile was tested in a single run. The polarization current load was applied to examine the fuel cell response typically tested to represent the fuel cell performance. To investigate the time response of the model, alternating step currents of minimum and maximum based on the input operating conditions were applied. The step current was repeated to investigate if similar result was repeatable.

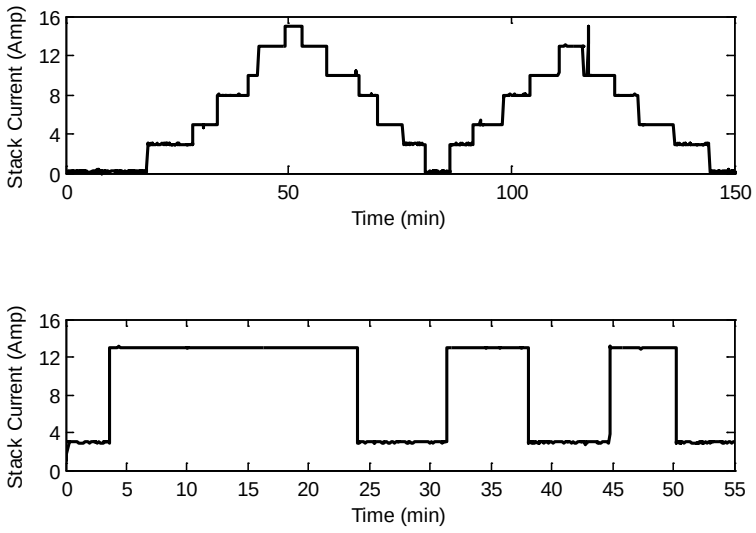

Figure 3.3: Polarization and alternating step current load profiles respectively.

3.2 MODEL CORRECTION AND CALIBRATION

From the thermal control perspective, the experimental validation focuses on the cathode temperature prediction. This is because the reaction and water produced are in the cathode side, and also the water is dragged through the membrane from the anode side to the cathode side. Hence it can be predicted that the liquid water flooding occurs first in the cathode side.

There are two variables and one parameter needed to be tuned to calibrate the thermal model. They are: the surface fuel cell body temperature (T_{SFC}) appeared in Equations 2.3 and 2.6, the cathode temperature inside the fuel cell (T_{ca}) in Equation 2.23, the heating value (E) in Equation 2.7. The effect of the sensor housing on the temperature was also investigated.

3.2.1 Sensor Housing Correction

It was found that the model cathode temperature was a couple of degrees higher than the experimental cathode temperature after the adjustment and calibration. The first observation suggested that the thermocouple sensor used to measure the cathode outlet temperature was attached by a Swagelok sensor housing. The housing was not thermally insulated and caused heat loss to the ambient, resulting in a lower cathode outlet temperature reading. This was corrected by adding a control volume analysis of the sensor housing. The energy balance for the housing is:

$$\frac{dU_{Sh}}{dt} = Q_{Sh,amb,conv} + H_{Sh,in} - H_{Sh,out} \tag{3.1}$$

where subscripts *Sh* and *amb* stand for *sensor housing* and *ambient*, respectively.

The left hand side of Equation 3.1 is expanded as

$$\frac{dU_{Sh}}{dt} = \left(\sum \frac{dm_{Sh}}{dt} C_{v_{Sh}}\right) T_{Sh} + \left(\sum m_{Sh} C_{v_{Sh}}\right) \frac{dT_{Sh}}{dt}$$

$$= \left(\dot{m}_{O_2,Sh} C_{v_{O_2}} + \dot{m}_{N_2,Sh} C_{v_{N_2}} + \dot{m}_{vap,Sh} C_{v_{vap}} + \dot{m}_{liq,Sh} C_{liq}\right) T_{Sh}$$

$$+ \left(m_{O_2,Sh} C_{v_{O_2}} + m_{N_2,Sh} C_{v_{N_2}} + m_{vap,Sh} C_{v_{vap}} + m_{liq,Sh} C_{liq}\right) \frac{dT_{Sh}}{dt} \tag{3.2}$$

Since the outlet enthalpy of the cathode control volume becomes the inlet enthalpy of the sensor housing, the enthalpies are calculated by

$$H_{Sh,in} = \left(\dot{m}_{O_2,in,Sh} C_{v_{O_2}} + \dot{m}_{N_2,in,Sh} C_{v_{N_2}} + \dot{m}_{vap,in,Sh} C_{v_{vap}}\right) T_{Sh,in} \tag{3.3}$$

$$H_{Sh,out} = \left(\dot{m}_{O_2,out,Sh} C_{v_{O_2}} + \dot{m}_{N_2,out,Sh} C_{v_{N_2}} + \dot{m}_{vap,out,Sh} C_{v_{vap}}\right.$$

$$\left. + \dot{m}_{liq,out,Sh} C_{liq}\right) T_{Sh,out} \tag{3.4}$$

where $T_{Sh,in} = T_{ca,out}$.

The heat transferred by convection between the sensor housing to the ambient is calculated similarly to that of the fuel cell body case.

$$Q_{Sh,amb,conv} = h_{c_{Sh,amb}} A_{Sh,amb} \left(T_{Sh,in} - T_{amb}\right) \tag{3.5}$$

The heat coefficient of convection, $h_{c_{Sh,amb}}$, is based on the air property and the ambient air flow rate surrounding the sensor housing.

The first subplot in Figure 3.4 shows the polarization current load applied to the fuel cell stack in a single run. The second subplot shows the before and after sensor housing correction of the modeled cathode outlet temperature. Note that the uncorrected and corrected modeled cathode outlet temperatures are presented after all the three parameters previously mentioned were tuned to give a good demonstration. Even though Figure 3.4 is based on one test, other tests run under the similar condition gave the same trend with similar accuracy.

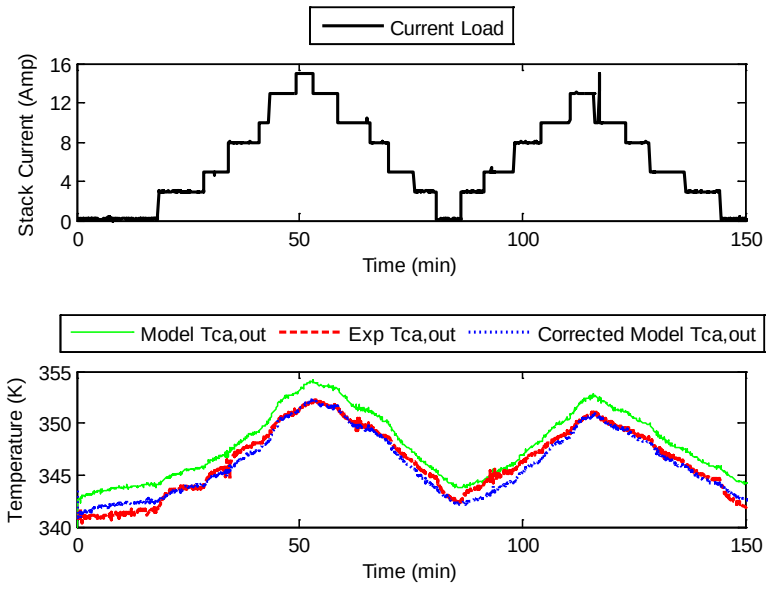

Figure 3.4: Sensor housing corrected model of the cathode outlet temperature and the experimental cathode outlet temperature comparison.

After the cathode outlet temperature was corrected due to the sensor housing, adjustments of the fuel cell body and cathode outlet temperatures were performed for calibration. The fuel cell body temperature must be calibrated first because of the amount of fuel cell internal energy is much greater than the cathode channel internal energy. Therefore an adjustment of the fuel cell body temperature gives a big change to the outlet cathode temperature. In contrast, cathode outlet temperature adjustment does not give any significant changes to the fuel cell body temperature.

To calibrate the cathode outlet temperature, the cathode channel temperature and heating value were adjusted. The cathode channel temperature should be adjusted first where its value lies between the cathode inlet temperature and cathode outlet temperature. The effect is to set the maximum and minimum temperatures to match the polarization temperature data. The heating value adjustment was performed to further fine tune the cathode outlet temperature, where the cathode channel temperature adjustment could not be further tweaked. The effect is to shift the cathode outlet temperature. These adjustments are presented in the following subsections.

3.2.2 Fuel Cell Body Temperature Adjustment

The fuel cell body surface temperature (T_{SFC}) appeared in Equations 2.3 and 2.6 was assumed to have the same value as the fuel cell body temperature (T_{FC}) since the control volume approach used to develop this thermal model neglects the spatial temperature variation. Theoretically the fuel cell body temperature gradient is proportional to the heat conduction by the relation:

$$Q_{conduction} = k \frac{dT}{dx} \tag{3.6}$$

where k is the heat conduction coefficient. Because of that, the fuel cell body surface temperature is substituted by the fuel cell body temperature minus a constant. Thus Equations 2.3 and 2.6 become:

$$Q_{amb,conv} = h_{c_{FC,amb}} A_{FC,amb} (T_{FC} - T_c - T_{amb}) \tag{3.7}$$

$$Q_{amb,rad} = \varepsilon \, \sigma \, A_{FC,amb} ((T_{FC} - T_c)^4 - T_{amb}^4) \tag{3.8}$$

T_c in the above equations is a constant temperature parameter. The regression analysis indicated that the value of T_c equals to 17 K. It gives a good agreement with the experimental data. Figure 3.5 shows the fuel cell body temperature before and after adjusting the fuel cell body surface temperature. It should be noted that the experimental fuel cell body temperature is assumed to have the same values as the experimental coolant temperature that is discuss in the next subsection.

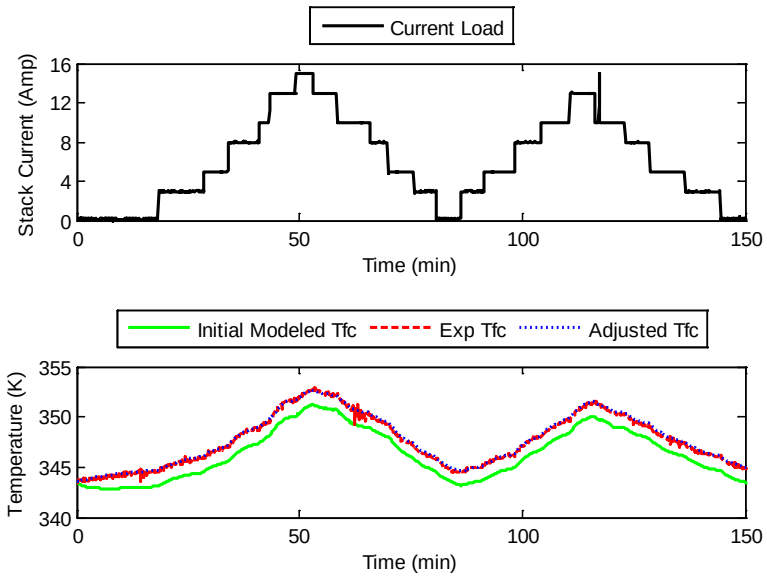

Figure 3.5: The fuel cell body temperature before and after adjusting the fuel cell body surface temperature.

3.2.3 Cathode Channel Temperature Adjustment

The cathode temperature inside the fuel cell (T_{ca}) appeared in Equation 2.23 was calibrated to obtain a good result of the cathode outlet temperature. Since the cathode temperature has a minimal effect on the fuel cell body temperature, it was calibrated after the fuel cell body surface temperature was adjusted. Initially it was assumed that the cathode temperature had the same temperature as the outlet cathode temperature. However the gap between the highest and the lowest temperatures were lower than that of the experimental cathode temperatures.

It was determined that the value of the cathode temperature such that:

$$T_{ca} = \frac{0.46\, T_{ca,in} + 1.54\, T_{ca,out}}{2} \tag{3.9}$$

Figure 3.6 compares the initially assumed temperature and calibrated one at the cathode outlet. The calibrated temperature better agrees with the experimental data.

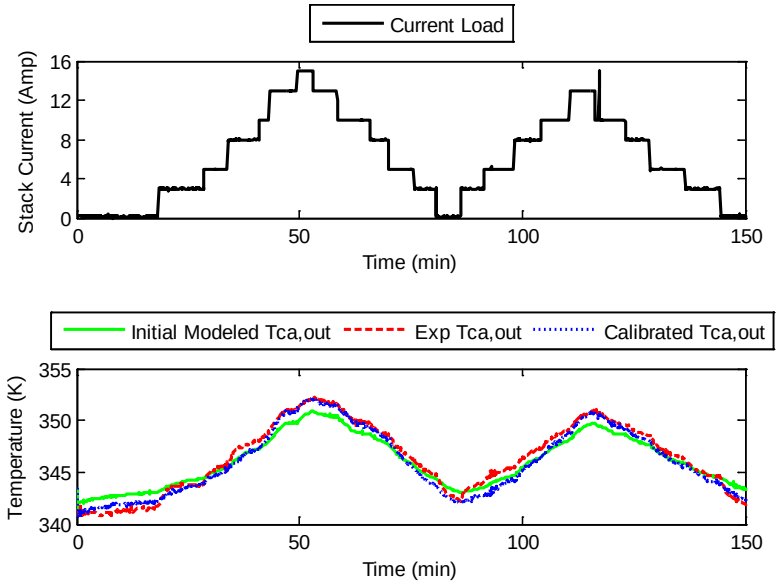

Figure 3.6: Cathode outlet temperature before and after cathode temperature calibration.

3.2.4 Heating Value Calibration

After performing the sensor housing correction and temperature adjustments, the model still predicted a slightly higher cathode outlet temperature during high current input than what was found experimentally as seen in Figure 3.7. The hypothesis is that this discrepancy might be caused by the value of the ideal voltage *E* used in the heat generation calculation in the fuel cell body temperature model from Equation 2.7.

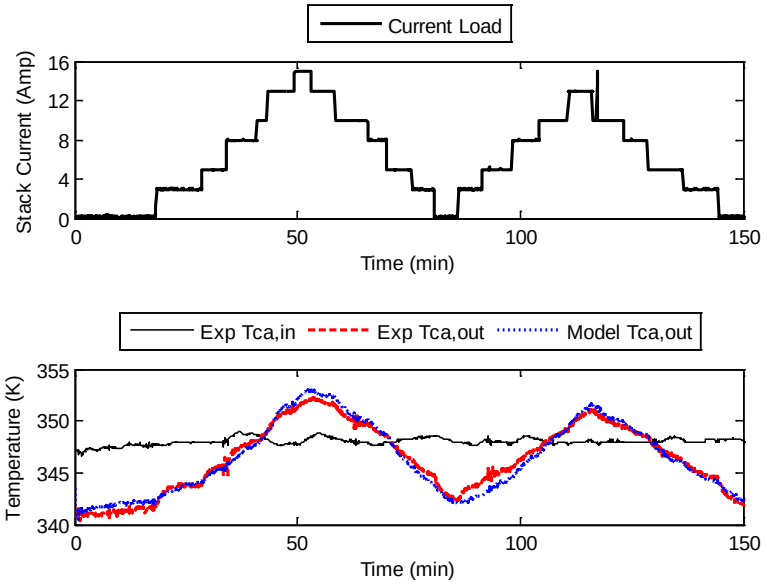

Figure 3.7: Model and experimental temperature comparison (E = 1.48V, HHV assumption).

During the initial development of the fuel cell model, it was assumed that the produced water was all in liquid phase. Consequently, the heating value of the ideal voltage E to be 1.48 Volts (HHV) as previously mentioned in Chapter 2. It was found that using the value of E in between the HHV and LHV led to the more accurate result. In comparison, the LHV assumption is applied and the model prediction is shown in Figure 3.8. Mostly the predicted model cathode temperature is lower than the experiment cathode temperature.

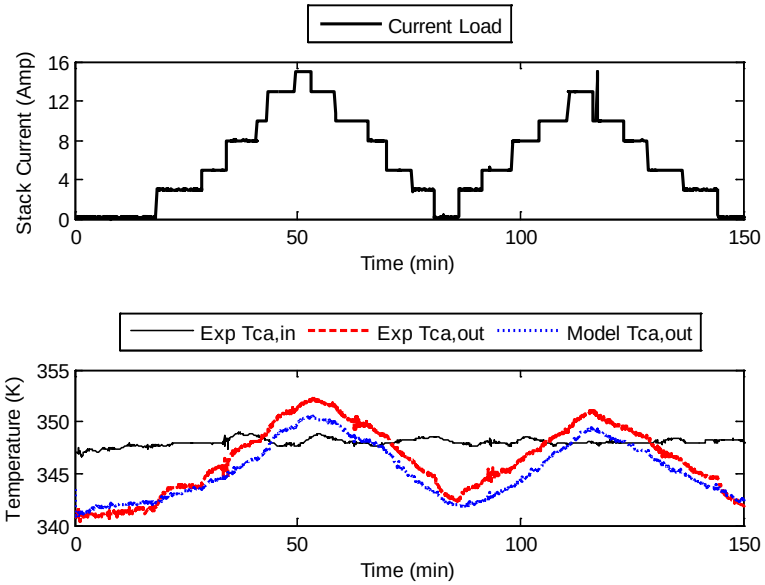

Figure 3.8: Model and experimental temperature comparison (E = 1.25V, LHV assumption).

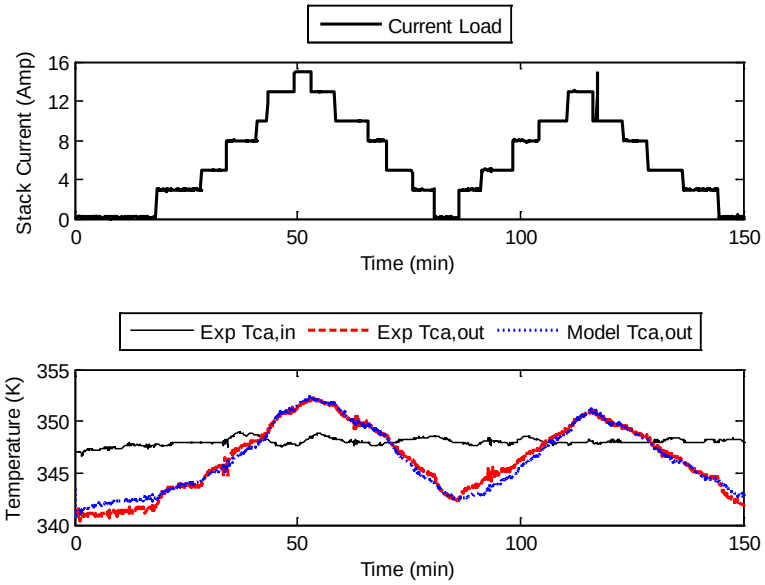

Figure 3.9: Model and experimental temperature comparison (E = 1.4V).

For the calibration, the value of E was determined to be 1.4 Volts to match closely to the experimental data and the result is shown in Figure 3.9.

Overall, the model prediction agrees much better with the experimental data after the value of E was adjusted. Once the thermal calibration was completed, the voltage model was also investigated under the same current load against the experimental data. Figure 3.10 shows the measured voltage and the modeled voltage comparison. It can be seen that the modeled voltage gives good result after the temperature calibration also.

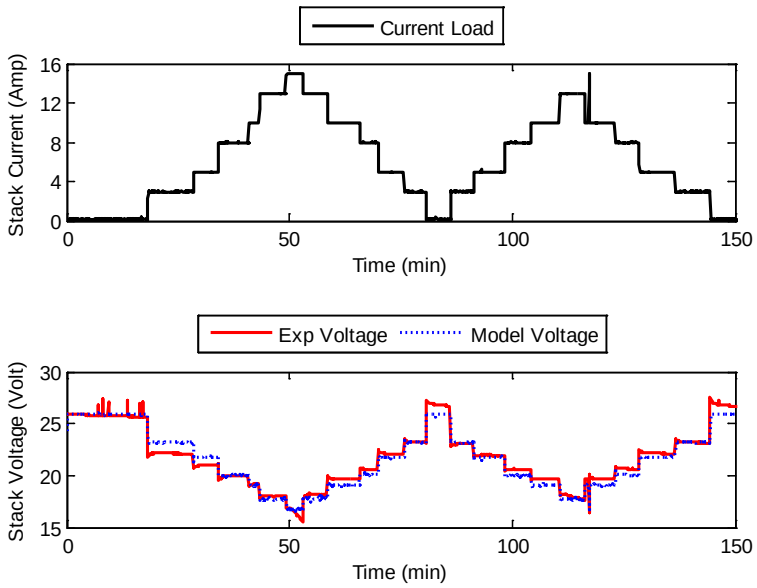

Figure 3.10: Model voltage results and experimental voltage comparison.

However, it should be noted that during the initial 30 minutes or so of the experiment, the model overestimates the voltage output. The effect diminishes as the experiment progresses, and does not occur even returning to the same load later in the cycle. This initial discrepancy might be due to a startup condition that is not accounted

for within the model, such as the fuel cell body temperature that was not yet evenly distributed, or the fuel cell was experiencing start–up flooding condition.

A closer examination of the temperature response shows that the slight inaccuracy in the temperature model is most likely not the source of the voltage discrepancy. Looking at Figure 3.9, one can see that the temperature has perhaps the closest agreement with the experimental data during the phase with the largest discrepancy in the voltage. We hypothesize that the source of this error is caused by the liquid water that may have accumulated in the flow channels or porous media which blocked the reactant gas flow during the initial test.

The coolant model temperature curve matches closely with the coolant experimental temperature curve shown in the first subplot of Figure 3.11. There was no dedicated temperature sensor to monitor continuously the fuel cell body temperature during the experiment. Occasionally, the fuel cell body surface temperature was monitored with a temperature gun. The second subplot shows the comparison of the coolant experimental and fuel cell body temperatures which happen to have the similar curve as we would assumed considering relatively high conduction coefficient of the graphite fuel cell body and convection coefficient of the liquid water coolant.

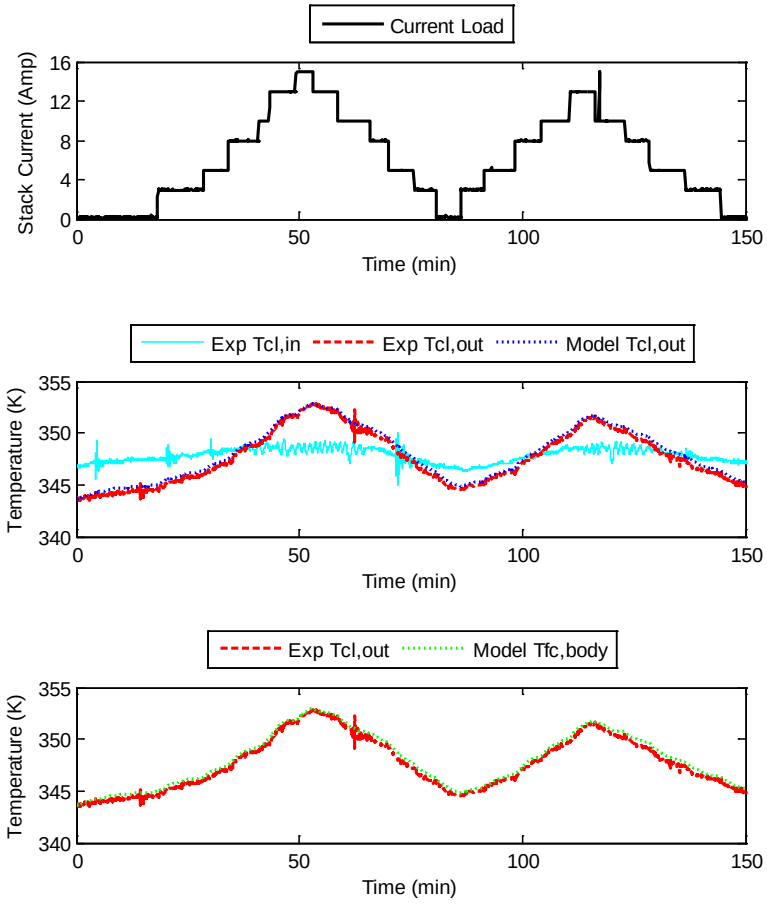

Figure 3.11: Model and experimental coolant and fuel cell body temperatures comparison.

3.3 MODEL VALIDATION TEST

To confirm the validity of the model after the calibrations in the previous section, an alternating step current input load was performed in a single run. The measured cathode temperature response was compared to the model results and is shown in Figure 3.12.

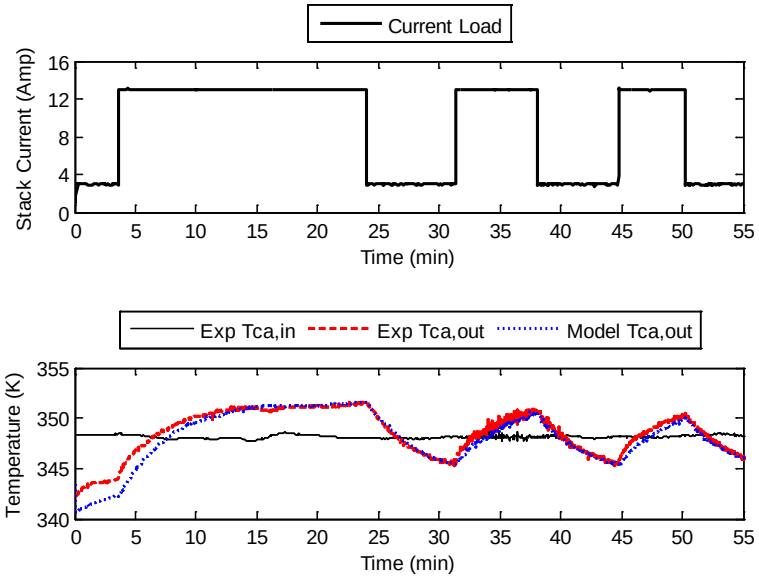

Figure 3.12: Model and experimental temperature step load validation.

It can be seen in the figure, after the temperature calibration and the use of the adjusted value of the ideal voltage E yields good results under an alternating current load condition, validating the alteration to the model. This implies that a mixture of liquid and vapor phase water is the product of the reaction. It depends on the flow and thermodynamics properties within the system that influence the phase of the water.

Unlike the calibration test, the initial voltage discrepancy between the model and the experiment was not seen in the validation test, where the voltage was underestimated.

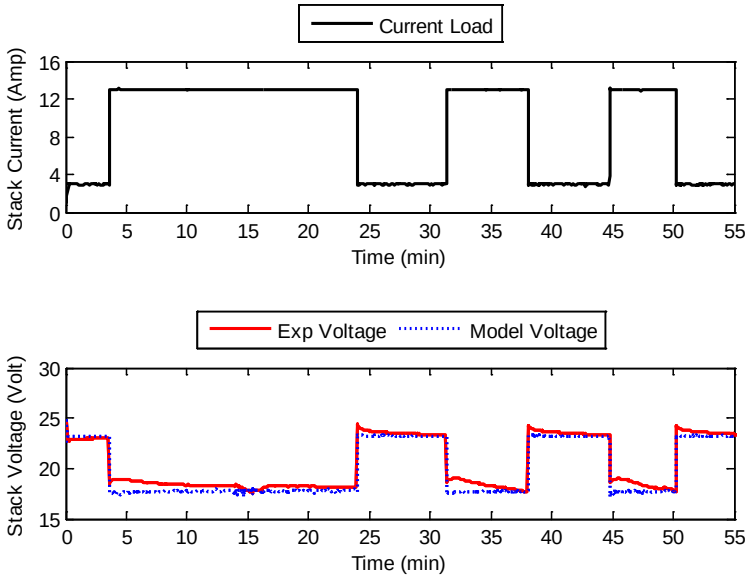

Figure 3.13: Voltage model results versus experimental validation test.

Some parts of the stack voltage dynamics responses are not captured by the voltage model shown in Figure 3.13. After the step change from a low current load to a high current load, the experimental voltage is higher than the modeled voltage, and then gradually approaches to be similar. Likewise, a step change from a high to a low current load shows a jump in experimental voltage in the beginning and a faster decay. Observations against the examination of the aforementioned adjustment of the ideal voltage E, the review in the literature, and the study of the two–phase flow model which is presented in Chapter 5 can be indirectly confirmed that the liquid water build up happened inside the gas channels and/or in the porous media. Despite those, the overall of the voltage model is in good agreement with the experimental results.

Figure 3.14 shows the model coolant and fuel cell body temperatures that matched closely with the experimental coolant temperature. Some small discrepancy can be seen which happens maybe due to the experimental inlet coolant temperature

fluctuations. However in overall, the model can predict the experimental temperatures very close.

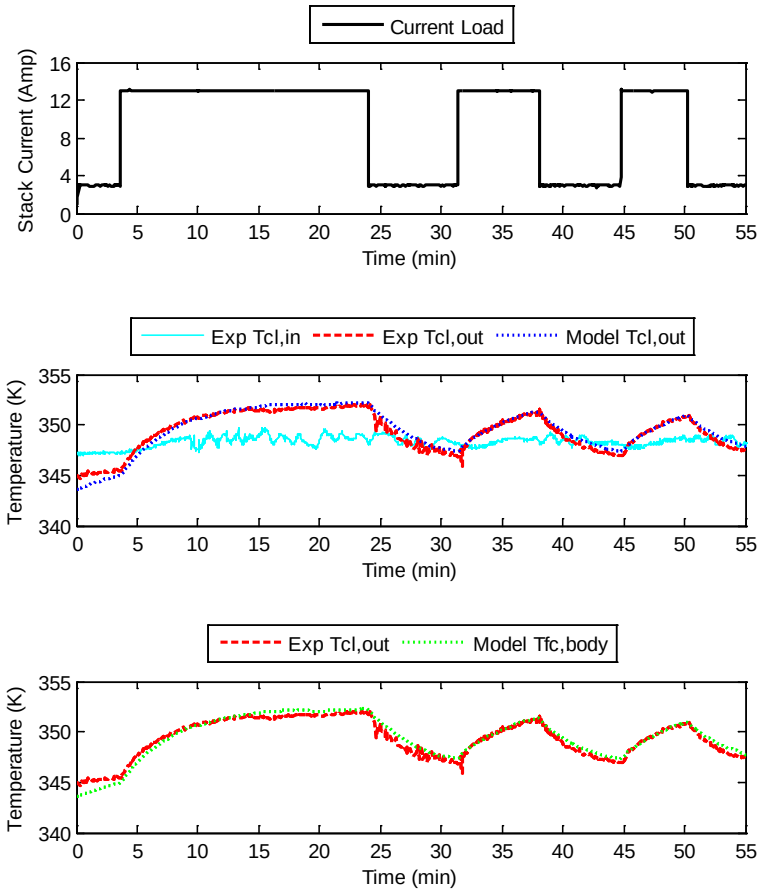

Figure 3.14: Coolant and fuel cell body model and experimental temperatures comparison.

Chapter 4: Relative Gain Array Analysis

4.1 Relative Gain Array Definition

The PEM fuel cell system model has many inputs and outputs which are the inlet gas flow rates, inlet gas pressures, inlet gas temperatures, water coolant flow rate, output voltage, and outlet temperatures. These render the system a multi–input multi–output (MIMO) system. A MIMO control scheme is important for a system that has multiple dependencies and interactions between its variables. Hence, understanding the dependence of different manipulated and controlled variables in a MIMO control scheme is very crucial in designing and implementing a control scheme for a system operation. On the other hand, a single–input single–output (SISO) control scheme may also be applied for a MIMO system if the system is decoupled.

Relative Gain Array (RGA) is one of the methods for analyzing a MIMO system to provide a quantitative measure of the interactions between the inputs and the outputs, showing if the system is towards more coupled or decoupled. It is expressed in an n (inputs) by n (outputs) normalized gain matrix that describes the effect of each input control variable on the outputs, relative to each control variable's effect on other variables [63, 64, 110–113]. The standard format is represented as follow.

$$\begin{bmatrix} Output_1 \\ Output_2 \\ \vdots \\ Output_n \end{bmatrix} = RGA \begin{bmatrix} Input_1 \\ Input_2 \\ \vdots \\ Input_n \end{bmatrix} \tag{4.1}$$

where

$$RGA = \begin{bmatrix} \lambda_{11} & \lambda_{12} & \cdots & \lambda_{1n} \\ \lambda_{21} & \lambda_{22} & \cdots & \lambda_{2n} \\ \vdots & \vdots & \ddots & \vdots \\ \lambda_{n1} & \lambda_{n2} & \cdots & \lambda_{nn} \end{bmatrix} \tag{4.2}$$

Each element λ_{nn} in the RGA matrix for a selected pair of input–output variables is defined as the ratio of the open loop gain for that pair with all other loops open to their open – loop gain where all other loops are closed in the process, with their variables held at set points by their controllers [112]. This format facilitates a control design engineer to easily compare the relative gains related with each input–output variable pair, and to match the input and output variables that have the largest effect on each other while minimizing unwanted outcome. An example of a closed–loop system is shown in Figure 4.1 and expressed as follows [112].

$$y_1 = a_{11}\, m_1 + a_{12}\, m_2 \tag{4.3}$$

$$y_2 = a_{21}\, m_1 + a_{22}\, m_2 \tag{4.4}$$

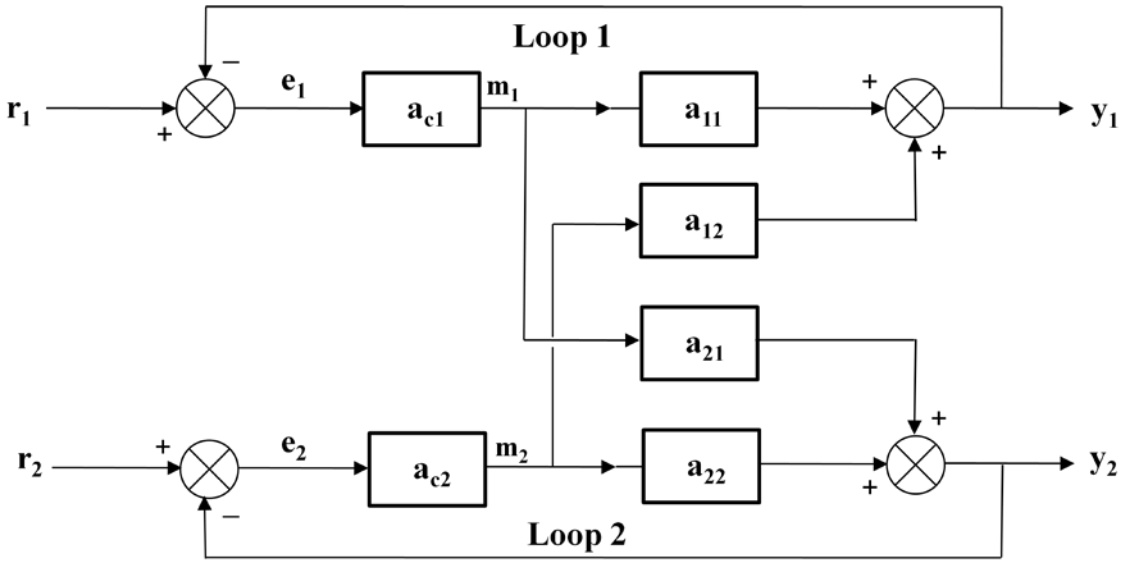

Figure 4.1: Closed–loop system diagram [110, 114].

From Equations 4.3 and 4.4 represented in the example diagram above, a 2 by 2 RGA matrix for the system can be calculated. The controlled variables y_1 and y_2 are

affected by the manipulated variables m_1 and m_2. The controlled variables y_1 and y_2 are compared with reference inputs r_1 and r_2 respectively, generally resulting in errors e_1 and e_2. The controller outputs, the manipulated variables, m_1 and m_2 are the responses of controllers a_{c1} and a_{c2} to errors e_1 and e_2, respectively, [110, 114].

Firstly, the objective is to calculate the effect of m_1 to y_1 by removing all the loops while keeping m_2 constant. The gain of y_1 due to m_1 with all the loops open is defined as:

$$g_{11} = \frac{\Delta y_1}{\Delta m_1} \quad (all\ loops\ open) \tag{4.5}$$

Secondly, to observe the effect of m_2 to y_1, loop 2 is closed and loop 1 remains open, and is calculated as:

$$g_{11}{}^{*} = \frac{\Delta y_1}{\Delta m_1} \quad (only\ loop\ 1\ open) \tag{4.6}$$

Finally the relative gain is defined as the ratio of the two gains above and represented as:

$$\lambda_{11} = \frac{g_{11}}{g_{11}{}^{*}} \tag{4.7}$$

In general form the relative gain is:

$$\lambda_{ij} = \frac{g_{ij}}{g_{ij}{}^{*}} = \frac{\frac{\delta y_i}{\delta m_j} \quad (all\ loops\ open)}{\frac{\delta y_i}{\delta m_j} \quad (all\ loop\ 1\ open)} \tag{4.8}$$

For other different kind of MIMO systems with specific feedback loops, the basic objective can be followed in a similar way described above.

RGA values are normalized, making the sum of each row or column in the RGA matrix equals to one. Normalization helps the readers to read the RGA. The system is

more decoupled if the values are closer to one and zero, and more coupled if the values are closer towards the value of one–half.

For a simple example, consider a MIMO system of two inputs and two outputs represented by Equations 4.5. The values in the RGA matrix diagonal are ones and all other values are zeros, as shown in Equation 4.6. This RGA indicates that the system is completely decoupled since each output depends only to a single input. For such a MIMO system, a SISO control scheme can be applied.

$$\begin{bmatrix} Output_1 \\ Output_2 \end{bmatrix} = RGA \begin{bmatrix} Input_1 \\ Input_2 \end{bmatrix} \tag{4.9}$$

$$RGA = \begin{bmatrix} 1 & 0 \\ 0 & 1 \end{bmatrix} \tag{4.10}$$

If the values of the RGA are such that shown in Equation 4.7, the system is fully coupled since each input affects both of the outputs equally.

$$RGA = \begin{bmatrix} 0.5 & 0.5 \\ 0.5 & 0.5 \end{bmatrix} \tag{4.11}$$

After the model is developed, the type of control framework can be chosen before a control design is determined. The heat transfer and mass transport inside the PEM fuel cell stack are coupled together which would typically require a MIMO controller for such system [61]. In the next sections RGA analyses results are presented to show the coupling between the inputs of interest to the outputs. RGA analyses were performed to determine the feasibility of applying the SISO control strategy which can simplify control design and reduce the processing power for the controller.

Two cases are presented. The first one is a 75 kW fuel cell stack model which has an air compressor model to represent the air supplied to the fuel cell. The other is the 1.5 kW fuel cell stack model which was validated in the previous chapter.

4.2 CASE 1: 1.5 KW FUEL CELL STACK

To perform the RGA analysis, the thermal model was first linearized using the linearize function of Matlab's Control System Toolbox at various operating conditions. The linearized equations are provided in the Appendix C. The operating conditions are the coolant temperature at 293K, 318K, and 343K, and the applied current load at 0.15, 5, 10, and 15 Amps, which are shown in table 4.1.

The control inputs of interests are the cathode inlet air flow rate $\dot{m}_{ca,in}$, the inlet water coolant flow rate $\dot{m}_{col,in}$, and the coolant inlet temperature $T_{col,in}$ since these variables can be independently adjusted by the controller and are not directly affected by the current load. The selected outputs for the analysis are the stack voltage V_{st} and the cathode outlet temperature $T_{ca,out}$. The stack voltage is the indicator of the fuel cell performance and its interaction with the cathode outlet temperature needs to be investigated. The inputs and outputs are correlated by the RGA matrix in Equations 4.8 and 4.9. The results of the RGA analyses at varying coolant temperatures T_{cl} and current loads I_{st} are shown in Table 4.1.

$$\begin{bmatrix} V_{st} \\ T_{ca,out} \end{bmatrix} = RGA \begin{bmatrix} \dot{m}_{ca,in} \\ \dot{m}_{col,in} \end{bmatrix} \tag{4.12}$$

$$\begin{bmatrix} V_{st} \\ T_{ca,out} \end{bmatrix} = RGA \begin{bmatrix} \dot{m}_{ca,in} \\ T_{col,in} \end{bmatrix} \tag{4.13}$$

where the RGA is

$$RGA = \begin{bmatrix} \lambda_{11} & \lambda_{12} \\ \lambda_{21} & \lambda_{22} \end{bmatrix} \tag{4.14}$$

$T_{cl} \setminus I_{st}$	0.15 A	5 A	10 A	15 A
293 K	$\begin{matrix} 0.9939 & 0.0061 \\ 0.0061 & 0.9939 \end{matrix}$	$\begin{matrix} 1.0002 & -0.0002 \\ -0.0002 & 1.0002 \end{matrix}$	$\begin{matrix} 0.9997 & 0.0003 \\ 0.0003 & 0.9997 \end{matrix}$	$\begin{matrix} 0.9988 & 0.0012 \\ 0.0012 & 0.9988 \end{matrix}$
318 K	$\begin{matrix} 0.9943 & 0.0057 \\ 0.0057 & 0.9943 \end{matrix}$	$\begin{matrix} 1.0003 & -0.0003 \\ -0.0003 & 1.0003 \end{matrix}$	$\begin{matrix} 0.9984 & 0.0016 \\ 0.0016 & 0.9984 \end{matrix}$	$\begin{matrix} 0.9961 & 0.0039 \\ 0.0039 & 0.9961 \end{matrix}$
343 K	$\begin{matrix} 0.9984 & 0.0016 \\ 0.0016 & 0.9984 \end{matrix}$	$\begin{matrix} 0.9996 & 0.0004 \\ 0.0004 & 0.9996 \end{matrix}$	$\begin{matrix} 0.9976 & 0.0024 \\ 0.0024 & 0.9976 \end{matrix}$	$\begin{matrix} 0.9953 & 0.0047 \\ 0.0047 & 0.9953 \end{matrix}$

Table 4.1: RGA analysis results for the relation $\begin{bmatrix} V_{st} \\ T_{ca,out} \end{bmatrix} = RGA \begin{bmatrix} \dot{m}_{ca,in} \\ \dot{m}_{col,in} \end{bmatrix}$.

The RGA analyses showed the values on the diagonal are close to a value of one and the off–diagonal values are close to a value of zero. This indicates that the effect of the coolant flow rate and cathode inlet air flow rate inputs to the stack voltage and cathode outlet temperature outputs are highly decoupled. For the case of 0.15 Amps current load, the trend of the RGAs shows a slightly more coupled of the coolant flow rate and cathode air flow rate inputs with higher current load and coolant temperature outputs. However the changes in RGAs are very small and the couplings are negligible. For that reason, SISO control can be safely applied to the system for those inputs.

The following are the RGA results comparing the influence of the cathode gas flow rate and coolant temperature inputs.

$T_{cl} \setminus I_{st}$	0.15 A	5 A	10 A	15 A
293 K	0.9874 0.0126 0.0126 0.9874	1.0003 − 0.0003 −0.0003 1.0003	0.9994 0.0006 0.0006 0.9994	0.9975 0.0025 0.0025 0.9975
318 K	0.9883 0.0117 0.0117 0.9883	1.0005 − 0.0005 −0.0005 1.0005	0.9967 0.0033 0.0033 0.9967	0.9919 0.0081 0.0081 0.9919
343 K	0.9968 0.0032 0.0032 0.9968	0.9992 0.0008 0.0008 0.9992	0.9950 0.0050 0.0050 0.9950	0.9902 0.0098 0.0098 0.9902

Table 4.2: RGA analysis results for the relation $\begin{bmatrix} V_{st} \\ T_{ca,out} \end{bmatrix} = RGA \begin{bmatrix} \dot{m}_{ca,in} \\ T_{col,in} \end{bmatrix}$.

Similar to the previous results, the RGA values show that the stack voltage is strongly influenced by the cathode inlet air flow rate which affects very weakly the outlet cathode temperature. Likewise the outlet cathode temperature is strongly influenced by the inlet coolant temperature which affects very weakly the stack voltage. The couplings towards higher current loads and coolant temperature are also negligible.

It can be determined for a SISO control framework that the input–output pairings are the cathode inlet air flow rate with the stack voltage and the inlet coolant flow rate or inlet coolant temperature with the cathode outlet temperature.

4.3 CASE 2: 75 KW FUEL CELL STACK

For case 2, a 75 kW fuel cell stack RGA analysis is presented [65]. The model includes a compressor sub–system model to supply air to the fuel cell stack. The control inputs are the compressor voltage V_{cmpr} instead of the cathode inlet air flow rate in case 1, and the coolant flow rate $\dot{m}_{col}$. The outputs are the power generated P_{gen} and the stack temperature T_{st} instead of the stack voltage and the cathode outlet temperature,

represented in Equation 4.8. However those inputs values are correlated and the results were expected to be similar.

$$\begin{bmatrix} P_{gen} \\ T_{st} \end{bmatrix} = RGA \begin{bmatrix} V_{cmpr} \\ \dot{m}_{col,in} \end{bmatrix} \tag{4.15}$$

$T_{col} \setminus I_{st}$	50 A		100 A		150 A		200 A	
283 K	0.8322	0.1678	0.8933	0.1067	0.9231	0.0769	0.9334	0.0666
	0.1678	0.8322	0.1067	0.8933	0.0769	0.9231	0.0666	0.9334
303 K	0.8510	0.1490	0.9021	0.0979	0.9282	0.0718	0.9408	0.0592
	0.1490	0.8510	0.0979	0.9021	0.0718	0.9282	0.0592	0.9408
323 K	0.8511	0.1489	0.9133	0.0867	0.9409	0.0591	0.9550	0.0450
	0.1489	0.8511	0.0867	0.9133	0.0591	0.9409	0.0450	0.9550

Table 4.3: RGA analysis results for the relation $\begin{bmatrix} P_{gen} \\ T_{st} \end{bmatrix} = RGA \begin{bmatrix} V_{cmpr} \\ \dot{m}_{col} \end{bmatrix}$ of the 75 kW Fuel Cell Stack [65].

The RGAs for the compressor voltage and coolant flow rate inputs with power generated and stack temperature outputs are shown in Table 4.3. The variables are decoupled although not as strongly decoupled as the 1.5 kW fuel cell stack variables in case 1. The main reason of increases in couplings is due to the nonlinear dynamics of the compressor that are affected by the current load and temperature; the higher the current load and temperature, the more decoupled the variables. In general, the system is considered highly decoupled and the SISO control methods will work well for the fuel cell stack system. The RGAs suggest that the compressor voltage is paired with the power generated and the coolant flow is paired with the stack temperature.

To analyze further the use of a compressor to supply pressurized air, the energy drawn by the compressor must be put into account. In this case, the net power of the fuel

cell system would be of interest rather than the generated power. Table 4.4 shows the RGAs calculated based on the compressor voltage V_{cmpr} and the coolant flow rate $\dot{m}_{col}$ inputs and the net power P_{net} and stack temperature T_{st} outputs. The net power equals the generated power minus the compressor power.

$$P_{net} = P_{gen} - V_{cmpr}\, I \tag{4.16}$$

$T_{col} \setminus I_{st}$	50A	100A	150A	200A
10°C	0.4188 0.5812 0.5812 0.4188	0.6656 0.3344 0.3344 0.6656	0.7760 0.2240 0.2240 0.7760	0.8227 0.1773 0.1773 0.8227
30°C	0.2046 0.7954 0.7954 0.2046	0.6692 0.3308 0.3308 0.6692	0.7629 0.2371 0.2371 0.7629	0.6431 0.3569 0.3569 0.6431
50°C	0.6097 0.3903 0.3903 0.6097	0.7726 0.2274 0.2274 0.7726	0.8358 0.1642 0.1642 0.8358	0.8716 0.1284 0.1284 0.8716

Table 4.4: RGA analysis results for the relation $\begin{bmatrix} P_{net} \\ T_{st} \end{bmatrix} = RGA \begin{bmatrix} V_{cmpr} \\ \dot{m}_{col} \end{bmatrix}$ of the 75kW Fuel Cell Stack [65].

The RGA values in Table 4.4 show that at low current load and coolant temperature the variables are coupled, while at higher current load and coolant temperature, the variables become more decoupled. This indicates that when the auxiliary components such as compressor are added to the system, the system becomes more complex and may be more coupled than the stack itself. As a result, while the RGA analyses showed that SISO control design would be effective for controlling only the fuel cell stack, the more complex integrated system requires a MIMO control framework.

The RGA analyses presented in normalized numbers on the two cases above show the degree of couplings. From the control design perspective, these analyses help the

designers to choose the SISO or MIMO control design depending on the system interaction, application, and designer's justifications and objectives of the end result.

Chapter 5: Incorporation of Porous Media Model for Catalyst Layer

5.1 LITERATURE REVIEW

As previously mentioned in the first chapter, thermal and water management is very important for PEM fuel cells to have high performance, efficiency, and reliability. Water management is correlated with humidification of the polymer membrane. Fuel cell flooding in the catalyst layer causes poor performance. Previous research results also indicated that flooding in the catalyst layer (CL) could reduce the life of the electrode. Therefore, it is important to understand and model the humidification condition of the CL. Catalyst layer mainly consists of porous material. Water dynamics inside a CL can be described by two–phase flow in porous media. In this section, reviews of modeling two–phase flow in porous media are presented.

To better understand the water transport and the gas reactant flow within porous media i.e. GDL and CL, many researchers have developed one, two, or three dimensional CFD models [17, 27, 33, 47, 66–74]. The two–phase flow model developed by Wang's research group comprehensively described the water flow as vapor and liquid phases in porous media [71–74]. Basic characteristics of the two different types of GDL porous media, carbon paper and carbon cloth, were thoroughly presented. Their advantages and disadvantages were also compared [73]. The study of the capillary properties of porous media by Nguyen's group provided guidance for GDL and CL designs. It showed the effect of the porous media property modifications that correlated the degree of flooding to the fuel cell performance [47, 69]. Those models basically represent similar physics based model which employs diffusion law based on concentration gradient for the gas phase and Darcy's law for the liquid water transport where capillary is the driving force for the liquid water to flow in porous media.

An obvious distinction of those research group approaches is the use of capillary pressure approximation. Wang's and most other research groups used Udell's correlation namely the Leverett J–function which was developed for sand packs and widely used in the geological and petroleum areas to express the capillary pressure function for fluid trapped in rock dirt formation in the earth. Alternatively, Nguyen's group used an empirical correlation which they developed base on experimental data for carbon papers and fitted into a fitting function [69]. They claimed that the fitting function was more accurate and removed the uncertainties of the parameters when a porous media was characterized and measured [75–84]. Even though those models are not suitable for control design due to their steady–state nature and computationally intensive characteristic, the above models provide details of the PEM fuel cell flow, temperature, and humidity conditions. They could be used as a base to develop a two–phase flow control–oriented model that focuses on the flooding effect on fuel cell performance during transient.

In order to fully understand the fuel cell transient thermal and humidification behavior in the automotive application, a control–oriented thermal dynamics fuel cell model that considers two–phase water flow model is required. Although being computationally intensive types of models, two–phase flow thermodynamic modeling techniques developed in References 69 and 72 would be a good starting point to develop a low–order control–oriented model. From the literature reviews above, emphasis should be given to capture the thermal dynamics and the flooding issue.

Additionally, investigation of water distribution in the GDL and CL and its effect on reactant species in an operating fuel cell should also be conducted. Even though it is difficult to obtain, such understanding will provide an enabling tool for water management inside a fuel cell stack. Many mathematical models have been developed to

gain qualitative insight, but these models treated the CL as an interface and did not fully account the effect of the liquid water build–up in this layer [17–20, 28, 33, 66, 86, 87]. It has been shown that water flooding level in the CL was higher than that in the GDL since the water is generated in this layer and removed from this layer via evaporation and/or capillary flow. For that reason the CL should not be treated as an interface and the effect of the liquid water in this layer on the cell performance should be taken into account [32, 67, 69].

McKay et al. presented a low order control–oriented model of the liquid and gas dynamics within GDLs to simulate the effects of reactant flow reduction and flooding [86, 87].The model is mainly based on the model developed in Reference 33. The model captured the dynamics of the reactant flow, pressure, and flooding effect on the PEM fuel cell voltage performance after tuning modeling parameters based on their experimental data. However the model did not include the CLs where the water is produced in this layer. Water dynamics in CLs were lumped together with the GDLs. In order to better understand the water dynamics in CLs and be able to predict the flooding effect inside CLS, it is necessary to develop a CL model and incorporate it into the overall fuel cell model. There exist few control–oriented models that include flooding effect; nevertheless experimental validations are still scarce [88–90]. In the following sections, modeling of water dynamics inside CLs will be presented.

5.2 MODEL DESCRIPTION

A one–dimensional, two–phase mass transport in porous media model for control application in order to capture the flooding and its effect to fuel cell performance is described in this section. The modeled domain is shown in Figure 5.1 and consists of the

polymer electrolyte membrane, CL and GDL layers, and gas channels in the anode and cathode sides. The anode and cathode outlet manifold are also included.

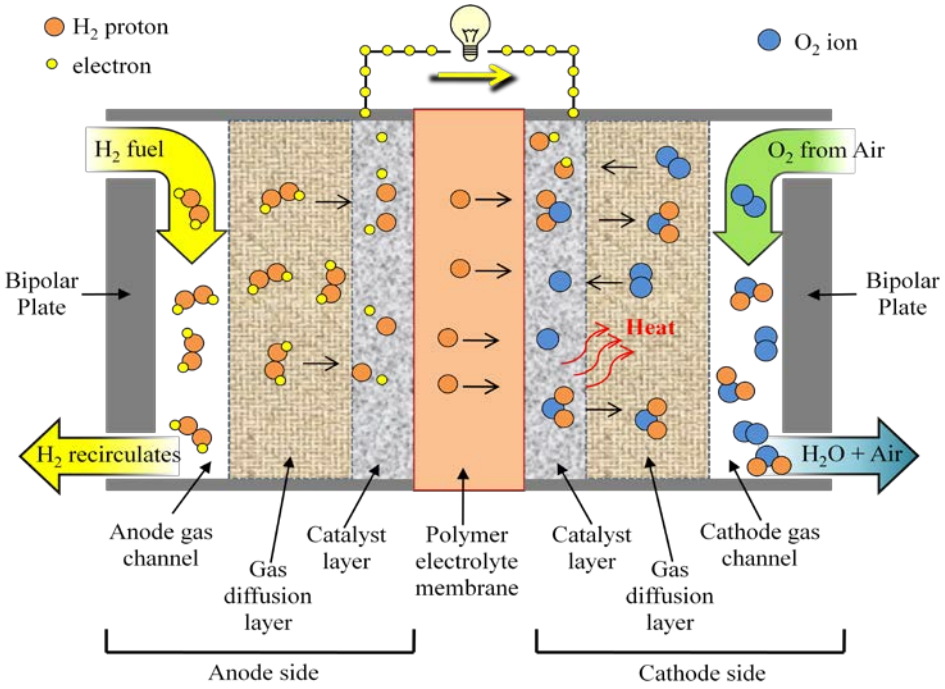

Figure 5.1: PEM fuel cell components and reaction schematic (not drawn to scale).

The anode volume contains a mixture of hydrogen and water, while the cathode volume contains a mixture of oxygen, water, and nitrogen. The concentration of each species is calculated based on the conservation of mass with the assumptions that the volumes are homogeneous, have lumped–parameter, and are isothermal. The model describes the diffusion of the gases and the capillary transport of the liquid water, as well as the time varying boundary conditions at the GDL and gas channel interfaces, and the membrane. The finite difference method was applied to approximate the one–dimensional gradients.

The initial approach of gas diffusion transport model is similar to the model in the literature [20, 32, 33, 67, 87]. The CLs are added to take into account the effect of the liquid water on the reactant and vapor concentrations in these layers which determine the cell voltage. Most porous media models in the literature employ Udell's correlation namely Leverett J–function to express the liquid water capillary flow [35, 39, 42, 48, 71–74]. The use of Udell's correlation in these models predicted rather low liquid water saturation levels in the gas diffusion components. Some experiments using diagnostic tools, such as pressure drop measurements with an interdigitated flow field and neutron radiography, have confirmed that the liquid water saturation levels in the gas diffusion components were higher than those predicted by those models [94]. Here, an empirical fitting function based on experimental data to estimate the liquid saturation level is used [68]. The fitting function removes the uncertainties of parameter values when a porous media was characterized and measured.

The cell voltage was estimated as a function of the reactant concentrations in the anode and cathode CLs, the membrane water content, temperature, and the modified current density due to active area reduction, which in turn is a function of liquid water accumulation in the gas channel.

The transient model is presented in a single dimension normal to the membrane area. Constant temperature with respect to time is assumed throughout the operating conditions of the fuel cell and no temperature gradient is considered. The gas transports in the porous media is due to diffusion caused by concentration gradient. Convective flow is neglected considering the small flux of reactant at the current density observed. The liquid water flow in the porous media is based on Darcy's law. It is assumed that no liquid water comes out of the channel and the water only escapes from the channel through evaporation. This assumption is based on a visual observation through the plastic

tube pipe of the anode and cathode outlets during the thermal validation experiment reported in the Chapter 3. In future, a more accurate measurement can be conducted when the outlets are environmentally controlled to detect any liquid water and humidity measured. The phase change of water of evaporation and condensation is assumed that it happens instantaneously regardless of the water surface area.

5.2.1 Porous Medium Characteristics

To analyze the fluid flow, the following definitions are presented to describe the characteristics of the porous media.

5.2.1.1 Porosity

Porosity is defined as the ratio of void volume (V_p) to total volume (V) of a porous medium.

$$\varepsilon = \frac{V_{pore}}{V_{pore} + V_{solid}} = \frac{V_p}{V} \tag{5.1}$$

5.2.1.2 Liquid Water Saturation

Liquid water saturation s is defined as the volume fraction of the total void volume of a porous medium filled by the liquid water volume (V_l).

$$s = \frac{V_l}{V_p} \tag{5.2}$$

5.2.1.3 Capillary pressure

Inside a porous medium, the liquid water flow is driven by capillary pressure. It is illustrated in Figure 5.2, as a branch–tree–like water percolation [33].

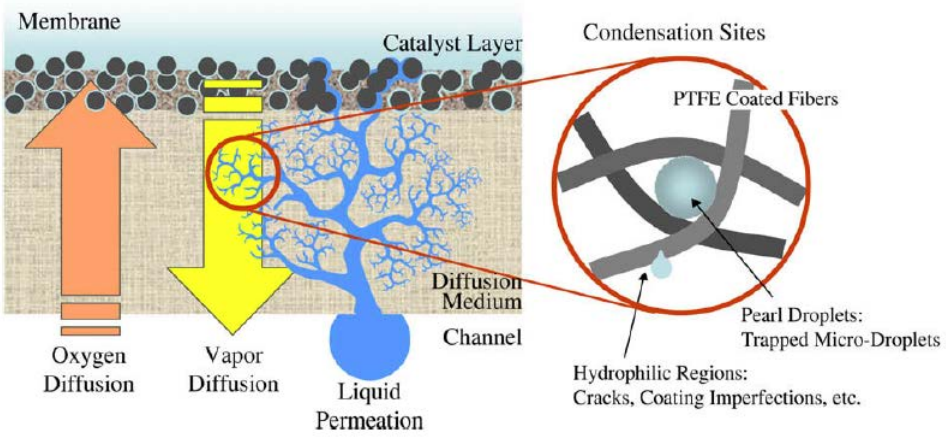

Figure 5.2: Illustration of water transport in hydrophobic porous media [33].

This capillary action results from the capillary pressure differences between the gas and liquid water. The capillary pressure p_c is typically defined as [71]

$$p_c = p_g - p_l \tag{5.3}$$

where p_g is the gas pressure and p_l is the liquid water pressure.

In hydrophilic porous media, the capillary pressure (p_c) is positive where the gas pressure (p_g) is higher than the pressure of the liquid phase (p_l). On the contrary, in hydrophobic porous media, the capillary pressure is negative where the liquid pressure is higher than the pressure of the gas phase [20].

$$\begin{aligned} p_c > 0 \ \therefore \ p_g > p_l \ \ for\ 0° < \theta_c < 90° \text{ (hydrophilic)} \\ p_c < 0 \ \therefore \ p_g < p_l \ \ for\ 90° < \theta_c < 180° \text{ (hydrophobic)} \end{aligned} \tag{5.4}$$

where θ_c is the contact angle of the liquid droplet measured from the surface. Figure 5.3 shows the examples of water droplet contact angles on hydrophobic and hydrophilic GDL surfaces.

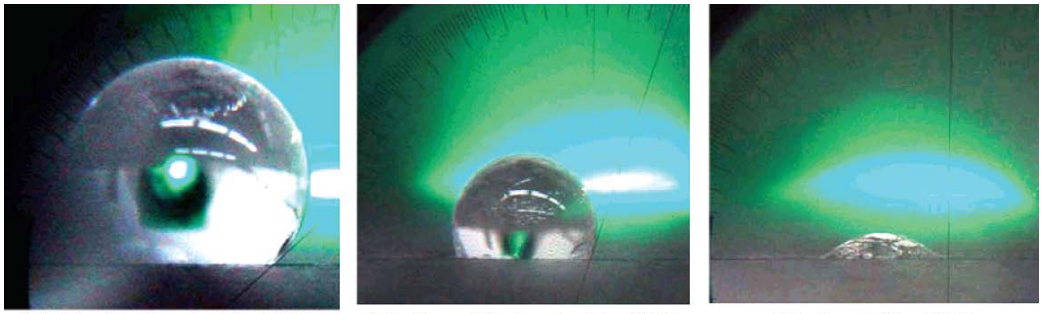

Figure 5.3: Liquid water droplets on GDL surface at different wettability at 70°C [70].

When the gas pressure and the liquid pressure are different, they are related by the equivalent capillary pore radius given by the Young–Laplace equation

$$r_c = \frac{2\,\sigma\,\cos\theta_c}{p_c} \tag{5.5}$$

where σ is the surface tension of the liquid water and is a function of temperature [70].

5.2.1.4 Relative Permeability

According to Darcy's law, liquid water flow in a porous media is driven by the liquid pressure gradient. The discharge flow rate (Q) is related to fluid viscosity (μ) and the pressure drop (Δp) at a distance length (Δx) by a proportional constant permeability as follow [104]

$$Q = \frac{K\,A}{\mu}\frac{\Delta p}{\Delta x} \tag{5.6}$$

If two fluids flow simultaneously in a porous medium, relative permeability K_{ri} is used and defined as the ratio of the intrinsic permeability K_i for liquid or gas at a given saturation to the total intrinsic permeability of the porous medium K.

$$K_{ri} = \frac{K_i}{K} \tag{5.7}$$

where i is the liquid or gas phase. Assuming the GDL and CL are homogeneous porous media, the relative permeability is proportional to the power of 3 of the saturation phase [33].

$$K_{rl} = s^3 \tag{5.8}$$

5.3 GOVERNING EQUATIONS

The governing differential equations for the gas phase and liquid phase are presented in the following subsections.

5.3.1 Gas phase diffusion

Gas flow in the porous media is governed by the fluid continuity equation, represented in the form of a partial differential equation

$$\frac{\partial c_i}{\partial t} = \frac{\partial N_i}{\partial x} + R_i \tag{5.9}$$

Equation 5.9 states that the time rate of change of the molar concentration c of each gas species i equals to local molar flux N gradient and the local reaction rate R.

The diffusion of the gas through the porous media is due to concentration gradient and the molar concentration of the gas species follow the ideal gas law such that

$$c_i = \frac{P_i}{R\,T} \tag{5.10}$$

where P_i is the partial pressure of the gas species, R is the universal gas constant, and T is the gas temperature.

The hydrogen fuel and water vapor diffuse in the anode porous media while the oxygen and water vapor diffuse in the cathode porous media. Nitrogen is an inert gas;

hence its concentration is assumed to be constant throughout the porous media and not calculated in the diffusion equation. Nitrogen crossover through the membrane from the cathode side to the anode side is neglected in this model although some reported that it happens during the reaction [109]. Therefore only binary diffusion is applied.

The molar gas flux N is a function of the concentration gradient and calculated by

$$N_i = -D_{i,eff} \frac{\partial c_i}{\partial x} \tag{5.11}$$

$D_{i,eff}$ in Equation 5.11 is the effective diffusivity that accounts for the presence of the liquid water in the porous media which reduces the actual porosity and thereby hinders the gas transport. The relation with the ordinary binary gas diffusivity D_i is as follows

$$D_{i,eff} = D_i \left[\varepsilon_j (1 - s)\right]^{1.5} \tag{5.12}$$

where the power of 1.5 is the Bruggeman's factor that accounts for the pore tortuosity [94]. Index j of the porous medium porosity ε signifies the porous medium type i.e. GDL or CL, and D_i is the gas species diffusivity.

5.3.2 Liquid Water Flow

Similar to the gas flow, the continuity equation governs the liquid water flow W_l in the porous media, represented by

$$\frac{\varepsilon_j \partial s}{\partial t} = \frac{\partial W_l}{\partial x} + \frac{M_v \, R_w}{\rho_l} \tag{5.13}$$

Equation 5.13 states that the time rate of change of the liquid water saturation s equals to local liquid water flow gradient and the local water reaction rate R of

evaporation or condensation. M_v is the vapor molar mass and the ρ_l is the liquid water density.

In the fuel cell, the water produced by the reaction in the anode CL increases the capillary pressure, causing the liquid water to flow to the gas channel through GDL. Applying Darcy's law in Equation 5.6, the liquid water flow in porous media is [66, 67, 87]

$$W_l = -\frac{\varepsilon_j \, A_{FC} \, \rho_l \, K_l \, K_{rl}}{\mu_l} \frac{\partial P_c}{\partial x} \tag{5.14}$$

A_{FC} in the above equation is the fuel cell area. μ_l and P_l, are the viscosity and the pressure of the liquid water respectively. K_l and K_{rl} are the liquid water permeability and relative permeability respectively as mentioned earlier.

Taking the saturation into account and assuming that the gas pressure is constant throughout the porous media, Equation 5.14 becomes

$$W_l = -\frac{\varepsilon_j \, A_{FC} \, \rho_l \, K_l \, K_{rl}}{\mu_l} \left(\frac{\partial P_c}{\partial s}\right)\left(\frac{\partial s}{\partial x}\right) \tag{5.15}$$

The differential of capillary pressure with respect to liquid water saturation requires a special attention. Most of the two phase flow models of PEMFC in the literature used Udell's correlation, namely Leverett J–function [71]. It calculates the capillary pressure using the following relation:

$$P_c = \sigma \cos\theta \left(\frac{\varepsilon}{K}\right)^{0.5} J(s) \tag{5.16}$$

The $J(s)$ in the above equation is the empirical Leverett J–function which is used generally in the petroleum area to model the oil trapped in porous rock dirt formation. The J–function is a function of saturation s and has the following forms [71]:

$$J(s) = \begin{cases} 1.417(1-s) - 2.120(1-s)^2 + 1.263(1-s)^3, & if \ \ 0° < \theta_c < 90° \\ 1.417s - 2.120s^2 + 1.263s^3, & if \ \ 90° < \theta_c < 180° \end{cases} \quad (5.17)$$

However in the PEMFC application that typically uses Teflon treated carbon paper or carbon cloth as the GDL, it was reported that it calculated lower saturation than the observance [67]. In this model, the capillary pressure proposed by Nguyen et al. is used and takes the form [68]

$$P_c = d\left[e^{-a_1(s-c)} - e^{a_2(s-c)}\right] + b \quad (5.18)$$

where s is the liquid water saturation and a_1, a_2, b, c, and d are fitting parameters.

Figure 5.4 is a measurement plot of the experimentally determined capillary pressure of Toray carbon paper 060 with 10% weight wet proof with PTFE by Nguyen's research group. The fitting parameters were obtained from experimental data using a volume displacement method with some adjustment to fit the model [94]. The fitting parameters for the CL were obtained by a neutron radiography method [95].

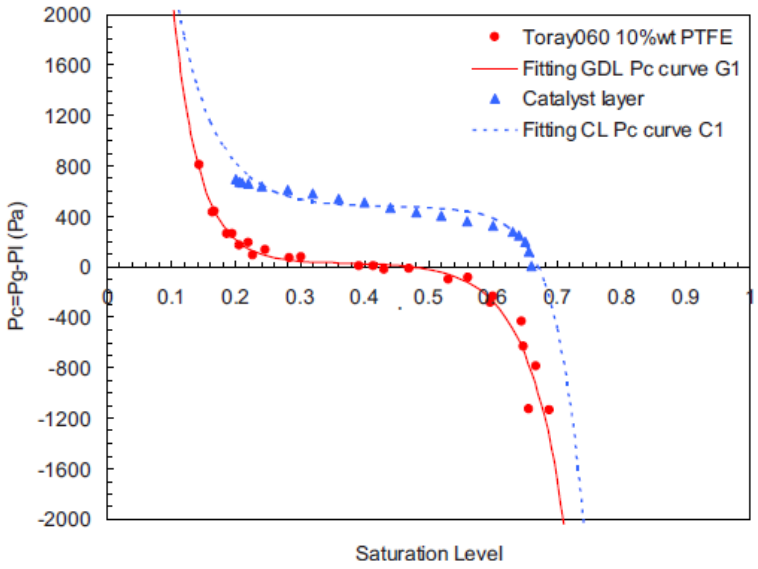

Figure 5.4: Experimentally determined capillary pressure of a GDL (Toray 060) and a CL. The fitting parameters of a_1, a_2, b, c, and d are –17.3, –25.1, 32.3, 0.35, and –4.06 for GDL G1 and –23.5, –17.4, 477.0, 0.46 and –3.58 for CL, respectively [69].

5.3.3 Boundary Conditions

The one–dimensional differential equations of gas diffusion in Equations 5.9 and 5.11, and liquid water flow in Equation 5.15 are solved using finite difference method. Each GDL and CL in the anode and cathode sides is divided into three sections with a finite thickness to approximate the solution of those equations. The three section division is considered coarse to solve the equations. However to reduce the complexity and computation time, and considering the thickness of the GDL and CL, a minimal division of three was chosen to obtain the response. Equations 5.9, 5.11, and 5.13 required boundary conditions to solve. The membrane and the gas channels become the time–varying boundary conditions. The schematic representation of the gases and water flows is shown in Figure 5.5.

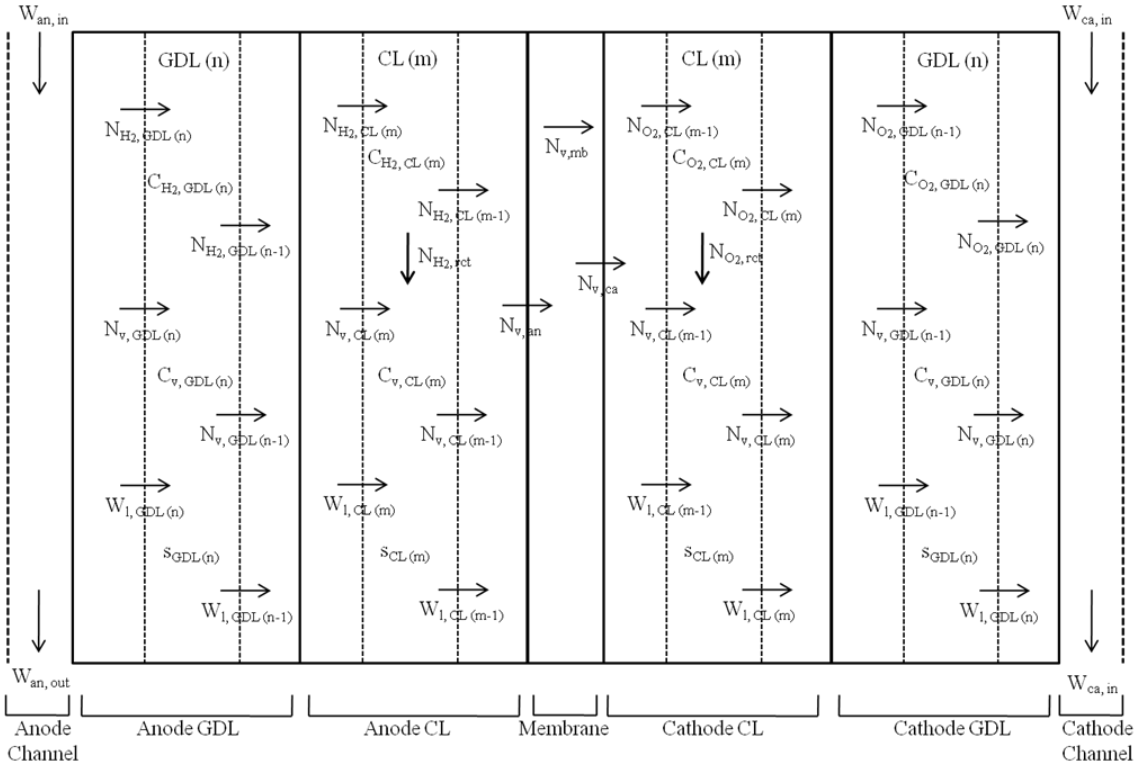

Figure 5.5: Schematic diagram of the discretization of the porous media layers.

5.3.3.1 Membrane boundary conditions

The membrane water content is influenced by the water vapor mass transport which varies during the dynamics operation. The water vapor flux through the membrane is caused by the electro–osmosis and back diffusion [46],

$$N_{v,mb} = n_d \frac{I}{A_{FC}\, F} - D_w \frac{\left(c_{v,ca,mb} - c_{v,an,mb}\right)}{t_{mb}} \tag{5.19}$$

where D_w is the water vapor diffusion coefficient of the membrane, and t_{mb} is the membrane thickness. n_d is the electro–osmosis coefficient of drag and depends on the membrane water content λ_{mb}.

$$n_d = \frac{2.5\ \lambda_{mb}}{t_{mb}} \tag{5.20}$$

The water vapor flux through the membrane depends on the water vapor diffusion coefficient [87]

$$D_w = 3.5 \times 10^{-6} \left(\frac{\lambda_{mb}}{14}\right) \exp\left(\frac{-2436}{T}\right) \tag{5.21}$$

The water vapor concentration in the CL section next to the membrane surface is

$$c_{v,j,mb} = \frac{2.5\ \rho_{mb,dry}}{M_{mb,dry}} \lambda_j \tag{5.22}$$

In the above equation, $\rho_{mb,dry}$ is the dry membrane density and $M_{mb,dry}$ is the membrane dry equivalent weight. λ is the membrane water content in the anode and cathode CL sections adjacent to the membrane surface and is a function of water activity a, i.e. relative humidity.

$$a_j = \frac{p_{v,j}}{p_{sat}} \tag{5.23}$$

The membrane water activity is averaged between anode and cathode water activities.

$$a_{mbr} = \frac{a_{an} + a_{an}}{2} \tag{5.24}$$

Two measurements were conducted by Springer [46] and Hinatsu [97] to determine the membrane water content at 30°C and 80°C. For an intermediate temperature between those two measured temperatures, linear interpolation is used.

$$\lambda_i^{30^\circ C} = 0.043 + 17.81\ a_i - 39.85\ {a_i}^2 + 36.0\ {a_i}^3 \tag{5.25}$$

$$\lambda_i^{80^\circ C} = 0.300 + 10.8\ a_i - 16.0\ {a_i}^2 + 14.1\ {a_i}^3 \tag{5.26}$$

5.3.3.2 Boundary conditions at the cathode channel

The gas species concentrations at the cathode channel determine the gas species concentrations at the cathode GDL section adjacent to the cathode channel. The oxygen, nitrogen, and water vapor concentrations are calculated based on the gas species mass conservation which depends on the cathode inlet and outlet gas properties that are the inlet temperature, relative humidity, pressure, gas flow rate and outlet pressure [60,87]. The oxygen, nitrogen, and water vapor mass conservations in the cathode channel are

$$\frac{dm_{O_2,ca}}{dt} = W_{O_2,ca,in} - W_{O_2,ca,out} + W_{O_2,an,GDL(3)} \tag{5.27}$$

$$\frac{dm_{N_2,ca}}{dt} = W_{N_2,ca,in} - W_{N_2,ca,out} \tag{5.28}$$

$$\frac{dm_{w,ca}}{dt} = W_{v,ca,in} - W_{v,ca,out} + W_{w,ca,GDL(3)} \tag{5.29}$$

where $W_{O_2,ca,in}$ is the mass flow rate of oxygen gas entering the cathode channel,

$W_{O_2,ca,out}$ is the mass flow rate of oxygen gas leaving the cathode channel,

$W_{O_2,an,GDL(3)}$ is the mass flow rate of oxygen gas entering the cathode GDL section 3 which is next to the cathode channel,

$W_{N_2,ca,in}$ is the mass flow rate of nitrogen gas entering the cathode channel,

$W_{N_2,ca,out}$ is the mass flow rate of nitrogen gas leaving the cathode channel,

$W_{v,ca,in}$ is the mass flow rate of water vapor entering the cathode channel,

$W_{v,ca,out}$ is the mass flow rate of water vapor leaving the cathode channel,

$W_{w,ca,GDL(3)}$ is the mass flow rate of water entering the cathode GDL section 3 which is next to the cathode channel.

The mass flow rates of each gas species entering the cathode channel are calculated by

$$W_{O_2,ca,in} = x_{O_2,ca,in}\, W_{da,ca,in} \tag{5.30}$$

$$W_{N_2,ca,in} = x_{N_2,ca,in}\, W_{da,ca,in} \tag{5.31}$$

$$W_{v,ca,in} = \omega_{ca,in}\, W_{da,ca,in} \tag{5.32}$$

The humidity ratio is defined by

$$\omega = \frac{M_v}{M_{da}} = \frac{\phi\, p_{sat}}{p - \phi\, p_{sat}} \tag{5.33}$$

And the mass fractions of oxygen and nitrogen are

$$x_{O_2} = y_{O_2} M_{O_2} / M_{da} \tag{5.34}$$

$$x_{N_2} = \left(1 - y_{O_2}\right) M_{N_2} / M_{da} \tag{5.35}$$

where the dry air molar mass is

$$M_{da} = y_{O_2} M_{O_2} + \left(1 - y_{O_2}\right) M_{N_2} \tag{5.36}$$

y_{O_2} is the oxygen mole fraction in dry air, approximated as 0.21.

The cathode channel pressure is the sum of each gas species partial pressure such that

$$p_{ca} = \frac{RT}{V_{ca}} \left(\frac{m_{O_2,ca}}{M_{O_2}} + \frac{m_{N_2,ca}}{M_{N_2}} \right) + \min \left[p_{sat}\, , \frac{RT\, m_{w,ca}}{V_{ca}\, M_v} \right] \tag{5.37}$$

The mass flow rates of gasses leaving the cathode channel are expressed by

$$W_{ca,out} = k_{ca,out} \left(p_{ca} - p_{ca,out} \right) \tag{5.38}$$

$$W_{da,ca,out} = \frac{1}{1 + \omega_{ca,out}} W_{ca,out} \tag{5.39}$$

$$W_{O_2,ca,out} = x_{O_2,ca,ch}\, W_{da,ca,out} \tag{5.40}$$

$$W_{N_2,ca,out} = \left(1 - x_{O_2,ca}\right) W_{da,ca,out} \tag{5.41}$$

$$W_{v,ca,out} = W_{ca,out} - W_{a,ca,out} \tag{5.42}$$

In the above equation, $k_{ca,out}$ is cathode outlet orifice constant. Although in the fuel cell station the outlet valve is controlled to maintain the cathode pressure, it is assumed to be constant in the model. For future work, it can be modified accordingly.

The liquid water saturation boundary condition in the GDL section next to the cathode channel is assumed to be zero i.e. no liquid forming on the GDL surface.

5.3.3.3 Boundary conditions at the anode channel

Similar to the cathode boundary conditions, the gas species concentrations at the anode channel determine the gas species concentrations at the anode GDL section adjacent to the cathode channel.

The hydrogen and water vapor mass conservations in the anode channel are

$$\frac{dm_{H_2,an}}{dt} = W_{H_2,an,in} - W_{H_2,an,out} + W_{H_2,an,GDL(3)} \tag{5.43}$$

$$\frac{dm_{w,an}}{dt} = W_{v,an,in} - W_{v,an,out} + W_{w,an,GDL(3)} \tag{5.44}$$

where $W_{H_2,an,in}$ is the mass flow rate of hydrogen gas entering the anode channel,

$W_{H_2,an,out}$ is the mass flow rate of hydrogen gas leaving the anode channel,

$W_{H_2,an,GDL(3)}$ is the mass flow rate of hydrogen gas entering the anode GDL section 3 which is next to the anode channel,

$W_{v,an,in}$ is the mass flow rate of water vapor entering the anode channel,

$W_{v,an,out}$ is the mass flow rate of water vapor leaving the anode channel,

$W_{w,an,GDL(3)}$ is the mass flow rate of water entering the anode GDL section 3 which is next to the anode channel.

The mass flow rate of hydrogen entering the anode channel is controlled with a pressure regulator in the fuel cell station.

$$W_{H_2,an,in} = k_{an,in}\left(p_{an,in} - p_{an}\right) \tag{5.45}$$

The cathode channel pressure is the sum of each gas species partial pressure and calculated by

$$p_{an} = \frac{RT}{V_{an}}\left(\frac{m_{H_2,an}}{M_{H_2}}\right) + \min\left[p_{sat}, \frac{RT\, m_{w,an}}{V_{an}\, M_v}\right] \tag{5.46}$$

The mass flow rates of gasses leaving the anode channel are

$$W_{an,out} = k_{an,out}\left(p_{an} - p_{an,out}\right) \tag{5.47}$$

$$W_{H_2,an,out} = \frac{1}{1+\omega_{an,out}}\, W_{an,out} \tag{5.48}$$

$$W_{v,an,out} = W_{an,out} - W_{H_2,an,out} \tag{5.49}$$

Similar to cathode, the liquid water saturation boundary condition in the GDL section next to the anode channel is also assumed to be zero.

5.3.4 Stack Voltage Equation

The stack voltage equation used in this porous media model is similar to the thermal model stack voltage equation with some modification of the activation voltage loss to account for the liquid water accumulation in the anode channel. Additionally, adjustable parameters are added to account for unmeasured voltage loss, variation in

measured parameters and in cell to cell voltages found in the experiment data. The stack voltage uses Equation 2.40 which is repeated here.

$$V_{fc} = (V_{ideal} - V_{act} - V_{ohm} - V_{conc}\ ) \times n_{cells} \tag{5.50}$$

The ideal voltage, V_{ideal}, is calculated the same manner as Equations 2.31 and 2.32. However instead of assuming liquid water form, the reaction product is assumed to be in the vapor form which gives a lower value of the ideal voltage and gives a better result when compared to the experimental data. The liquid water formation is assumed only to occur due to condensation.

$$V_{ideal} = \frac{1}{2F}\left[T\ \Delta S - \Delta H + RT \ln\left(\frac{p_{H_2,an\ (avg\ \ CL)}\ \ p_{O_2,ca\ (avg\ CL)}{}^{0.5}}{p_o{}^{1.5}}\right)\right] \tag{5.51}$$

The accumulated liquid water forms a thin film on the GDL surface, reducing the active fuel cell area. Since it is difficult to be measured, the liquid water film thickness is assumed. Since the active area is reduced, the real current density increases and is named the apparent current density. This approach was proposed in reference 87 to account for the anode channel water accumulation. It is utilized in this model and extended to also account for the cathode channel water accumulation. The stack voltage is calculated using the apparent current density of anode or cathode whichever has the greater value, i.e. greater coverage of liquid water covering the active area.

The liquid water accumulation in the anode channel is expressed by

$$m_{l,ch} = max\left[0, m_{w,an} - \frac{p_{sat}\ M_v\ V_{ch}}{RT}\right] \tag{5.52}$$

The apparent current density i_{app} is defined as

$$i_{app} = \frac{I_{st}}{A_{app}} \tag{5.53}$$

The apparent reduced fuel cell area A_{app} is estimated by

$$A_{app} = A_{fc} - \frac{2\, m_{l,ch}}{n_{cells}\, \rho_l\, t_{wl}} \tag{5.54}$$

where the t_{wl} is the liquid water thickness. The scaling factor of 2 was used to account for the channel ribs covering half of the active surface area, which reduces the area available for the formation of a liquid water film [87]. Another model also proposed an increased current density due to the water accumulation in the CL at CL–membrane interface [107].

The activation voltage loss takes the form of

$$V_{act} = A_1 \frac{RT}{F} \ln\left(\frac{i_{app} + i_{loss}}{i_0}\right) \tag{5.55}$$

In the above equation, i_{loss} is the current density loss caused by hydrogen crossover from anode to cathode side through the membrane. i_0 is the exchange current density which depends on the oxygen partial pressure and the fuel cell temperature.

$$i_0 = A_2 \left(\frac{P_{O_2,ca\ (avg\ CL)}}{P_0}\right)^{A_3} \exp\left[-\frac{E_c}{RT}\left(1 - \frac{T_{fc}}{T_0}\right)\right] \tag{5.56}$$

where E_c is the activation energy oxygen reaction reduction and T_0 is the reference temperature.

The ohmic voltage loss in Equation 2.34 is used with a modification of additional proportional constant A_4 in the following form.

$$V_{ohm} = A_4\, i_{app}\, R_{ohm} \tag{5.57}$$

A_1, A_2, A_3, and A_4 in Equations 5.55, 5.56, and 5.57 are adjustable parameters which were suggested to calibrate the stack voltage to account for cell to cell voltage variation, uncertainties, and for the flooding effect [67, 87, 102, 105, 106].

The concentration voltage loss is similar to Equation 2.39 with the application of apparent current density such that

$$V_{conc} = i_{app}\left(c_2 \frac{i_{app}}{i_{max}}\right)^{c_3} \tag{5.58}$$

A model to describe the two phase flow was developed in Matlab/Simulink environment based on the above modeling equations. A focus was first given to the mass transport behavior rather than heat transfer effect. A steady state temperature was assumed during the porous media modeling. The Matlab/Simulink representations are attached in the Appendix E.

Chapter 6: Simulation and Verification of Two–Phase Flow Model for Catalyst Layers

Simulations were conducted and the results were then calibrated and verified using the same experimental polarization and alternating step current input data described in Chapter 3. Regression was performed to tune model parameters focusing on the voltage response.

The fuel cell stack used in this experiment consists of 30 cells where the voltage of each cell was measured individually. The average cell voltage of the 30 cell voltages represents the experimental stack voltage that is used for calibration. Figure 6.1 shows current density load applied to the fuel cell stack and the individual voltages of the 30 cells with the average voltage plotted as a thick red line. It can be seen that the cell to cell standard deviation becomes larger when the current load is increased, while during low current load the variations are much smaller. This may be due to cell to cell differences in temperature, degree of flooding in the channel and porous media, reactant and oxidant concentration, relative humidity, as well as membrane conductivity.

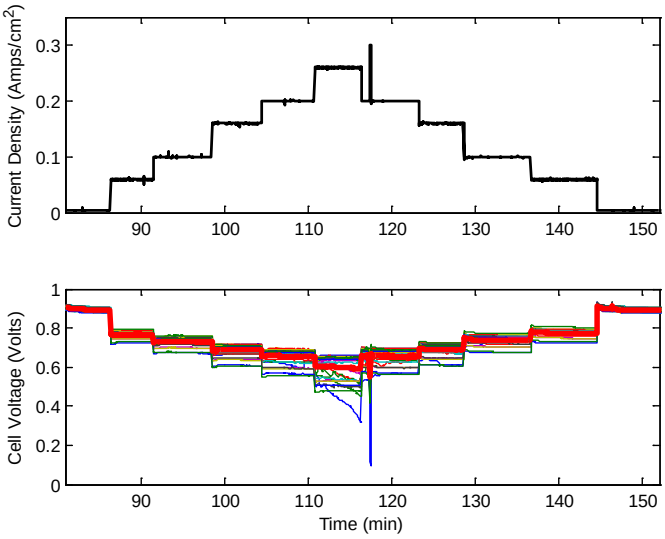

Figure 6.1: Individual cell voltages and the average cell voltage of the 30–cell fuel cell stack.

6.1 VOLTAGE CALIBRATION

It is generally acknowledged among fuel cell researchers that there is no single analytical solution that can model the voltage response satisfactorily for all cases [102]. Therefore calibration is needed to better represent the model output. An operational range of current load was applied to the 30–cell fuel cell stack that was assumed exhibiting both non–flooding and flooding conditions. The experimental voltage output showed degradation during high current load that was presumed the flooding occurred.

The initial result of the model voltage response is presented in Figure 6.2. It can be seen that the modeled voltage shows the proper trends although the curve is shifted upward and the curve profile is not proportional compared to the experimental data.

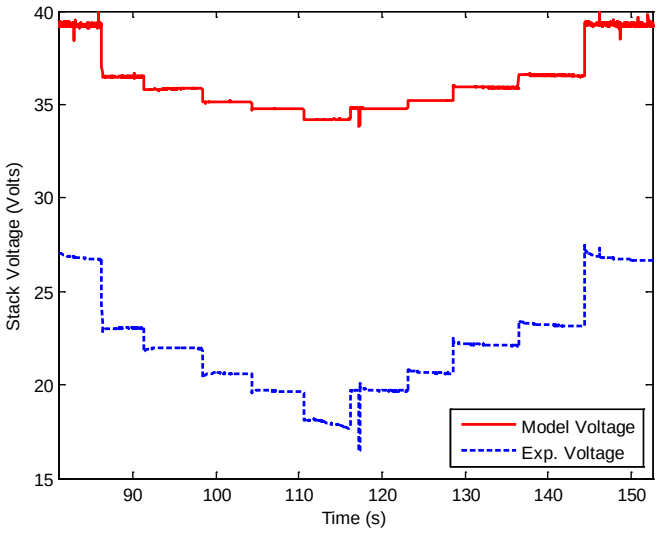

Figure 6.2: Initial simulation of the voltage response.

To calibrate the modeled voltage, the voltage losses need to be adjusted. Regression analysis was employed to estimate the constants A_1, A_2, A_3, and A_4 in Equations 5.55, 5.56, and 5.57. The modified voltage equation becomes

$$V_{fc} = \left(V_{ideal} - A_1 \frac{RT}{F} \ln\left(\frac{i_{app} + i_{loss}}{i_0}\right) - A_4\, i_{app}\, R_{ohm}\right) \times n_{cells} \tag{6.1}$$

where:

$$V_{ideal} = \frac{1}{2F}\left[T\,\Delta S - \Delta H + RT \ln\left(\frac{p_{H_2,an\,(avg\ \ CL)}\ \ p_{O_2,ca\,(avg\ CL)}{}^{0.5}}{p_o{}^{1.5}}\right)\right] \tag{6.2}$$

$$i_0 = A_2 \left(\frac{p_{O_2,ca\,(avg\ CL)}}{P_0}\right)^{A_3} \exp\left[-\frac{E_c}{RT}\left(1 - \frac{T}{T_0}\right)\right] \tag{6.3}$$

$$R_{ohm} = \frac{t_m}{\sigma_m} = \frac{t_m}{(b_{11}\lambda_m - b_{12})\, exp\left(b_2\left(\frac{1}{303} - \frac{1}{T_{fc}}\right)\right)} \tag{6.4}$$

R_{ohm} is the ohmic membrane resistance expressed in Equations 2.35, 2.36, and 2.37.

In order to run the regression analysis, first Equation 6.1 is linearized, which gives

$$V_{fc} = \left\{V_{ideal} - A_1 \frac{RT}{F}\left[\ln\left(i_{app} + i_{loss}\right) + \frac{E_c}{RT}\left(1 - \frac{T}{T_0}\right)\right] + A_1 \ln(A_2)\frac{RT}{F}\right.$$
$$\left. + A_1\, A_3 \frac{RT}{F} \ln\left(\frac{p_{O_2,ca\,(avg\ CL)}}{P_0}\right) - A_4\, R_{ohm}\left(i_{app} + i_{loss}\right)\right\} \times n_{cells} \qquad (6.5)$$

The concentration voltage loss is not accounted in this equation since the current load range is from 0 to 0.3 Amps/cm^2. The concentration loss is typically considered significant at higher current density loads, around 1Amps/cm^2 [60, 87].

The Microsoft Excel regression tool was utilized to process the experiment data, which provides the stack voltage V_{fc} shown in Equation 6.4. A multivariable regression was performed to find A_1, A_2, A_3 and A_4 in Equation 6.5 that provide the best fit for stack voltage. Here, the temperature T is assumed to be the same as the coolant temperature from the experimental data. The hydrogen partial pressure $p_{H_2,an\,(avg\ CL)}$, oxygen partial pressure $p_{O_2,ca\,(avg\ CL)}$, apparent current density i_{app}, and membrane water content λ_m are obtained from the simulation calculations. The regression result of A_1, A_2, A_3 and A_4 is listed in row "First Regression" of Table 6.1. Even though these four parameters were obtained from regression, they are all physical parameters. The feasibility of using those regression values should be examined.

The exchange current density in Equation 6.3 is revisited according to its original form as follow [102, 108].

$$i_0 = i_0^{ref} a_c\, L_c \left(\frac{p_{O_2,ca,CL}}{P_0}\right)^{\gamma} \exp\left[-\frac{E_c}{RT}\left(1 - \frac{T}{T_0}\right)\right] \qquad (6.6)$$

In the above equation, i_0^{ref} is the current density at reference temperature T_0 and pressure p_0 per unit platinum catalyst surface area (A/cm^2). Its value is in the magnitude of 10^{-9}

A/cm^2. a_c is the catalyst specific area which is around 600 to 1000 cm^2/mg (theoretical limit of platinum catalyst is 2400 cm^2/mg). L_c is the catalyst loading which is 0.4 mg/cm^2 used in this experiment. Considering those values, the coefficient of A_2 which is equal to $i_0^{ref} a_c L_c$, is in the magnitude of 10^{-7} to 10^{-6} A/cm^2. Assuming i_0^{ref} equals to $9x10^{-9}$ A/cm^2, a_c equals to 1000, the A_2 becomes $3.6x10^{-6}$ A/cm^2. The regression result of 0.001867556 A/cm^2 is larger than the above A_2 upper limit. Therefore, we have to choose $A_2 = 3.6x10-6$ A/cm^2.

γ, represented as coefficient A_3 in Equation 6.2, is the pressure dependence coefficient with respect to oxygen partial pressure and its suggested value is from 0.5 to 1.0 [102]. In the regression observation, γ shapes the voltage curve during the high current density where flooding happens. It was found that the value greater than 1 led the voltage model to better agreement with the experimental voltage. However due to the above parameters' constraint, a maximum value of 1.0 should be for parameter A_3 instead of the regression result of 4.909837247.

A_1 is related to cathode transfer coefficient α_c such that

$$V_{act} = A_1 \frac{RT}{F} \ln\left(\frac{i_{app} + i_{loss}}{i_0}\right) = \frac{RT}{\alpha_c F} \ln\left(\frac{i_{app} + i_{loss}}{i_0}\right) \tag{6.7}$$

α_c equals to 1 at high cathode potentials (low current densities) and 0.5 at low cathode potentials (high current densities) [102]. This makes the range of A_1 from 1 to 2. The effect of increasing A_1 is to increase the overall activation voltage. Since A_2 and A_3 already maximized the activation voltage, A_1 could not be further increased more than 1. Therefore A_1 should use 1 instead of the regression result of 1.294751508.

There is no constraint on parameter A_4. A second regression on A_4 was then performance based on the above updated value of A_1, A_2 and A_3. The result is listed in row "Second Regression" of Table 6.1.

DATA	PARAMETERS			
	A_1	A_2	A_3	A_4
First Regression	1.294751508	0.001867556	4.909837247	1.951230007
Second Regression	1	3.6e–6	1	5.705676921

Table 6.1: The parameter result from the first and second regression analyses.

Applying the parameters of the "Second Regression", the modeled stack voltage is plotted against experimental data in Figure 6.3. Comparing with Fig. 6.2, the modeling accuracy has been significantly improved. However, there still exist discrepancies between the model and testing data. More research efforts are needed to close the gap.

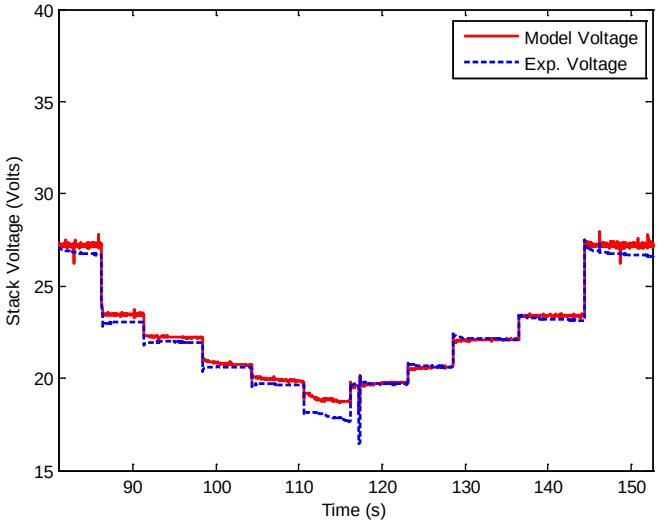

Figure 6.3: Stack voltage comparison between model and experimental data.

It should be noted that the above validation was conducted based on several experiments collected over one year. Even though our observation indicated the test data had a good repeatability and accuracy, it is necessary to provide a quantitative measure of

statistical significance for the test data. However, due to the high operating cost of the experiments (in terms of hydrogen gas and deionized water), we only performed these limited number of experiments. In the future, when the operating cost is reduced, we could apply the design of experiment (DOE) technical to obtain the value of A_1, A_2, A_3 and A_4.

6.2 POST CALIBRATION OBSERVATION FOR POTENTIAL IMPROVEMENT

In the previous section, after the parameters were adjusted, the voltage model fits better to the experimental data. However one can observe that some of the transient responses were not properly captured by the model. This section points out the causes that may possibly affect the transient response.

In order to show the transient response during the step voltage change, the model and experimental polarization curves of Figure 6.3 were magnified. Figure 6.3 is presented again with rectangular area of interest as shown in Figure 6.4. The portion inside the area is magnified and plotted in Figure 6.5. One can see that there are voltage spikes just after the voltage drop or rise which then gradually settles (circled area). These are commonly found in pressure build up in the manifold and/or inside the fuel cell channels, or due to compressor that supply the air pressure to the cathode channel. The fuel cell stack in this experiment used a fuel cell test station that provides the inlet pressure and its measurements. The pressure inside the fuel cell is regulated by a diaphragm valve via a controller. This valve is located at the gas outlet of the fuel cell. Since the diaphragm opening size of the valve could not be recorded, it was assumed constant in the model. Once the characteristic of the valve is known, the model can be modified and calibrated that may capture these transient responses. It can be seen also

from the second subplot of Figure 6.5, the cathode inlet pressure changes gradually whenever the voltage experiences a step change. The fuel cell station computer controls the compressor and the outlet valves to maintain the inlet gas flow rates.

From the above observations, the outlet diaphragm valve may be the main cause that changes the pressures inside the fuel cell channels. Since the experiment channel pressures could not be obtained and depends on the outlet diaphragm valve opening, the modeled stack voltage, which depends on pressure directly, could not catch those transient responses during the current input changes.

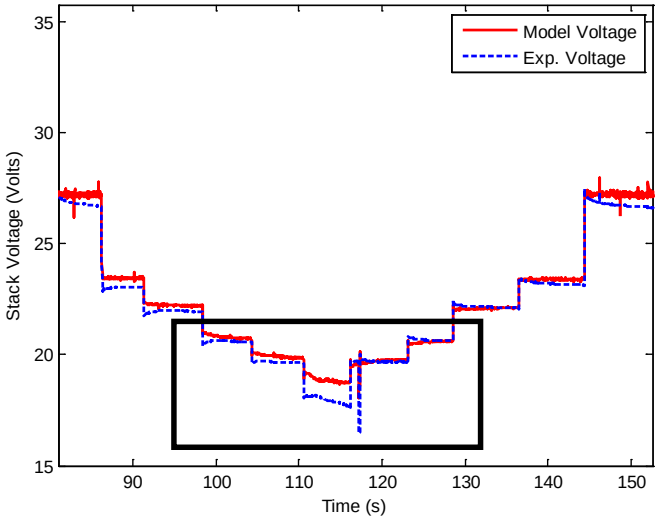

Figure 6.4: Rectangle area focus of voltage step change observation.

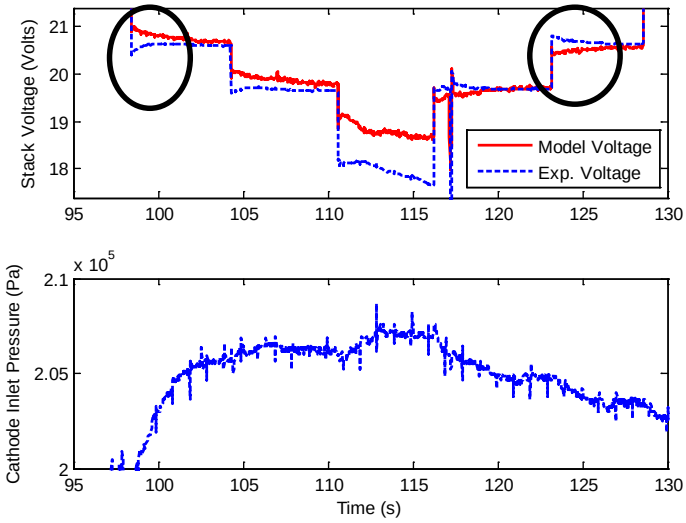

Figure 6.5: Voltage step change observation magnification of Figure 6.5.

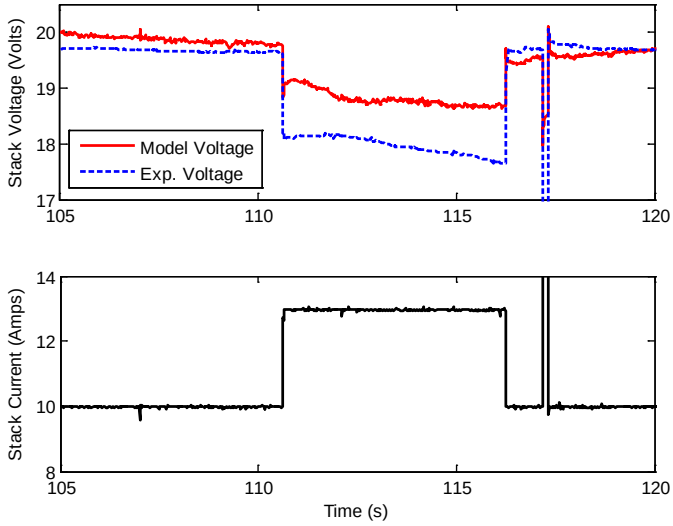

Figure 6.6: Voltage degradation at high current load.

Another observation is the voltage degradation at the high current load of 13 Amps shown Figure 6.6, where the stack voltage is around 18 Volts. Our initial guess was that flooding happened when liquid water accumulated inside the fuel cell without

being able to escape or vaporize quickly enough. Increasing the current load to more than 13 Amps shut off the fuel cell test station as it detected low voltage below the safety threshold. In the next section, by adjusting the orifice constant, it will be demonstrated that the flooding degrades the output voltage.

6.3 TUNING THE ORIFICE CONSTANT

As indicated in the previous section, the experimental voltage during high current load was not accurately captured by the model. The voltage degradation suggested flooding happened and the accumulated liquid water could not be removed or decreased by the out–flowing gasses from the anode and cathode outlets. The mass flow rates of the gas species flowing out from the fuel cell are given in Equation 5.38 and 5.47, and recaptured in the following.

$$W_{ca,out} = k_{ca,out}\left(p_{ca,ch} - p_{ca,out}\right) \tag{6.4}$$

$$W_{an,out} = k_{an,out}\left(p_{an,ch} - p_{an,out}\right) \tag{6.5}$$

Since the valve opening cannot be measured directly, it is assumed that the value of the valve opening, also known as orifice constant, was tuned according to the experimental data to match the operating pressures in the anode and cathode channels.

In this section, an alternating step input of the current demand shown in Figure 6.7 was used as the first attempt to verify the model. It was found that further orifice constant adjustment was necessary to calibrate the model. Figure 6.8 is the modeled stack voltage compared to the experimental data using the orifice constant of 1e–7 sec/m. Experimental data of anode and cathode inlet pressures are shown in Figure 6.9. The modeled voltage captures the transient response during high current demand, but not

during low current demand. As previously mentioned, this may be due to the pressure dynamics of the compressor and outlet valve opening as can be seen in the inlet pressures of anode and cathode in Figure 6.9. For future work it is necessary to investigate the operation of the fuel cell station that provides the inputs to the fuel cell.

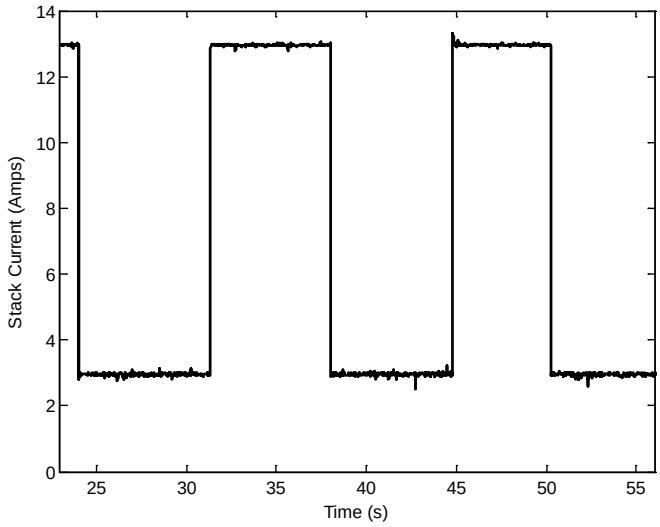

Figure 6.7: Step current load input.

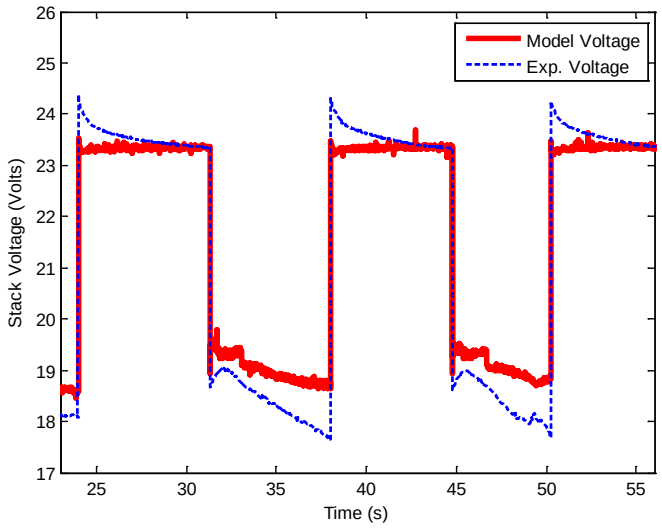

Figure 6.8: Step voltage response with orifice constant of 1e–7 sec/m.

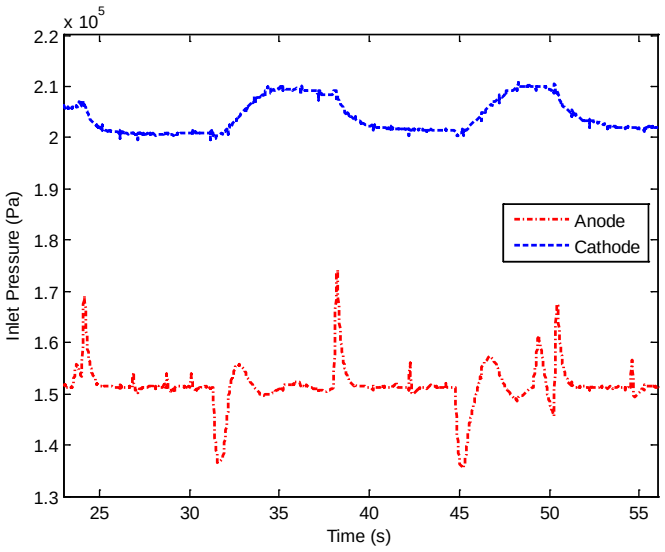

Figure 6.9: Anode and cathode experimental step input inlet pressures.

After the orifice constant is lowered to1.45e–8 sec/m, the voltage gradient during high current load is steeper similar to that of the experimental data. However the voltage is shifted upward due to the increase in pressure and hence increased the hydrogen and

oxygen concentrations, as shown in Figure 6.10. Further tuning of offsetting the voltage by –0.6 Volts gives a better result which is shown in Figure 6.11. Further characterization of the variable orifice dynamics is essential to further improve the modeling accuracy.

From the above and section 6.2 observations, it can be concluded that the channel pressures is affected by the outlet diaphragm valve and these pressure directly calculate the modeled stack voltage. During the high current load, the outlet valve opening is constant; thus the stack voltage transient response is represented by the model properly. However, during the current step changes, the outlet valve opening is changing; hence fluctuating stack voltage transient response could not be catched.

The dynamics of the opening of the outlet diaphragm valve is controlled by the fuel cell station computer and must be included in the model to capture the overall stack voltage transient response.

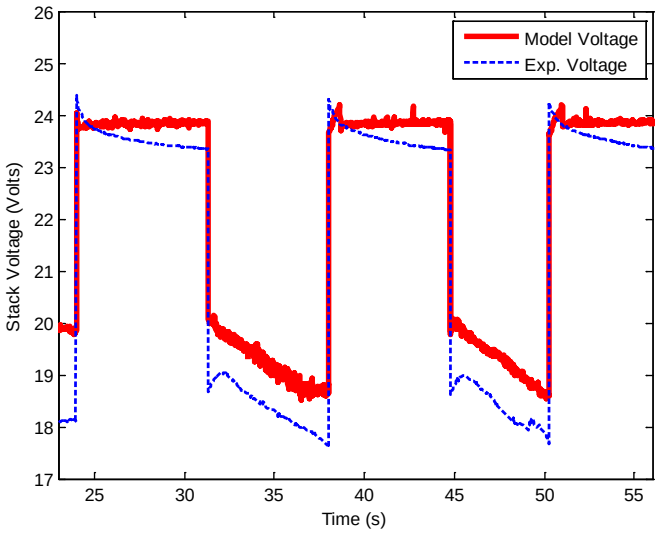

Figure 6.10: Step voltage response with orifice constant of 1.45e–8 sec/m.

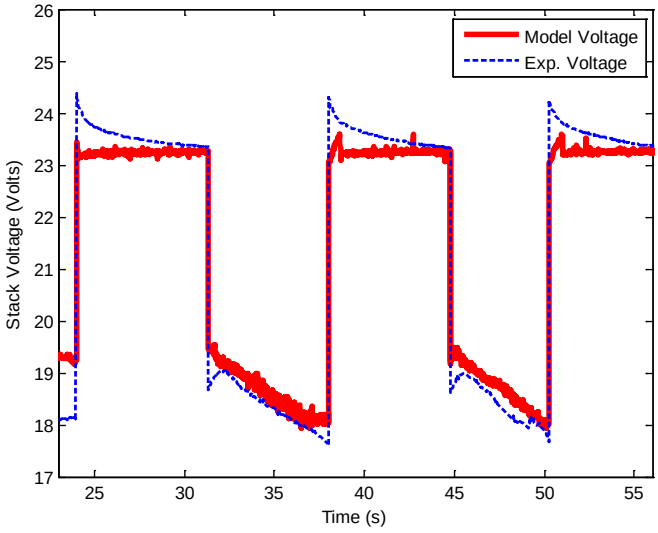

Figure 6.11: Step voltage response with orifice constant of 1.45e–8 sec/m, offset –0.6 Volts.

6.4 UTILITY OF THE DEVELOPED MODEL FOR FLOODING ESTIMATION

To demonstrate that the model captures flooding in the porous media and also in the channels, simulations were conducted and the results are shown as follows. Figures 6.12 and 6.13 show the saturation levels in the anode and cathode GDL and CL. The three different GDLs and CLs refer to the finite thickness division described in section 5.3.3 to solve the liquid water flow in GDLs and CLs (Equation 5.15). The GDL 3 is the GDL section next to the gas channel and GDL 1 is the GDL section adjacent to CL 3. The CL 1 is the CL section in contact with the membrane.

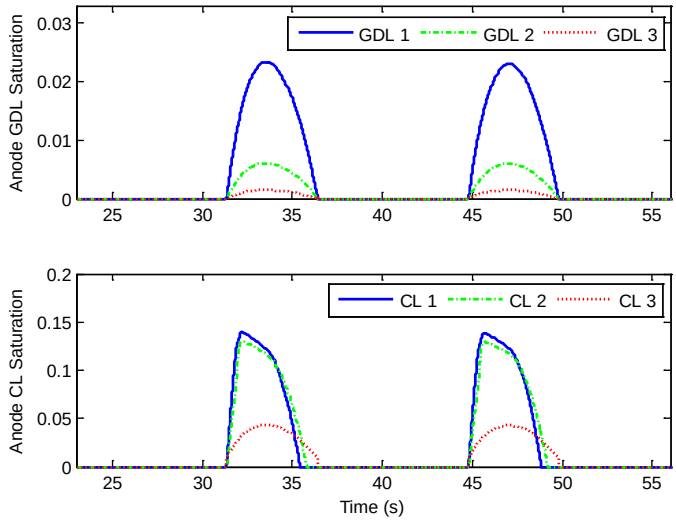

Figure 6.12: Model predictions of saturation level in the anode GDL and CL.

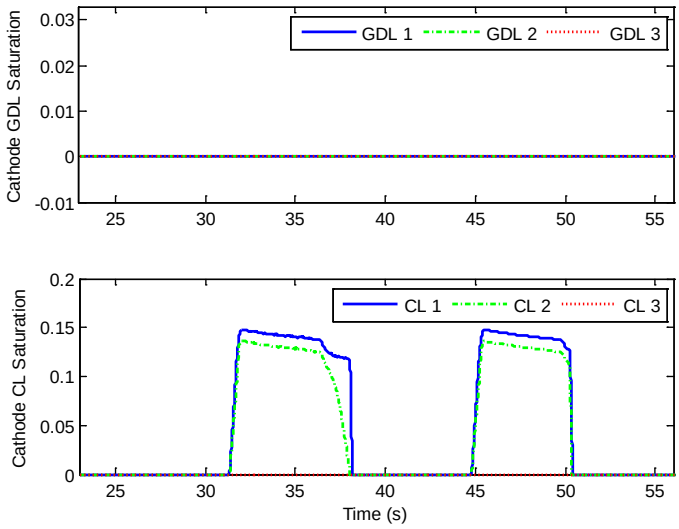

Figure 6.13: Model predictions of saturation level in the cathode GDL and CL.

Figure 6.14 shows the liquid water accumulations in the channels. The saturation in the cathode GDL is zero and no liquid water is accumulated in the cathode channel.

Flooding only occurs in the cathode CL during the high current demand. However in the anode side flooding occurs in three places, the GDL, CL and channel.

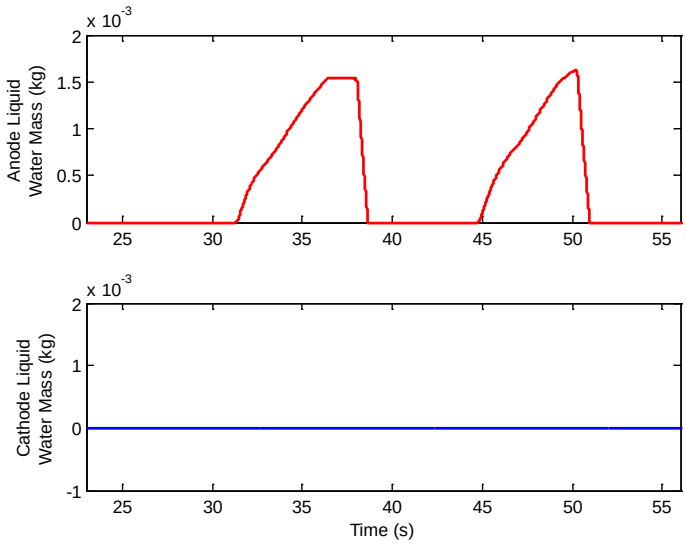

Figure 6.14: Model predictions of liquid water accumulation in the channel.

Looking at Figure 6.15, it was found that the anode RH reaches 100% during high current demand and resulted in condensation. On the other hand, the cathode channel never reaches 100% RH. Due to higher input pressure that causes higher gas flow rate of the cathode channel than that of the anode channel, the liquid water inside the cathode side is simply vaporized and removed by gas convection. A high cathode inlet RH (~80%) also forces higher back diffusion to diffuse water vapor from cathode to anode side (Figure 6.16).

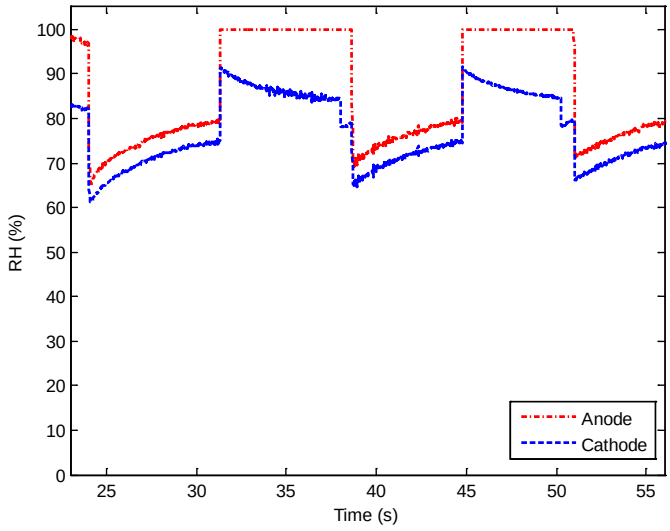

Figure 6.15: Model predictions of anode and cathode channel RHs.

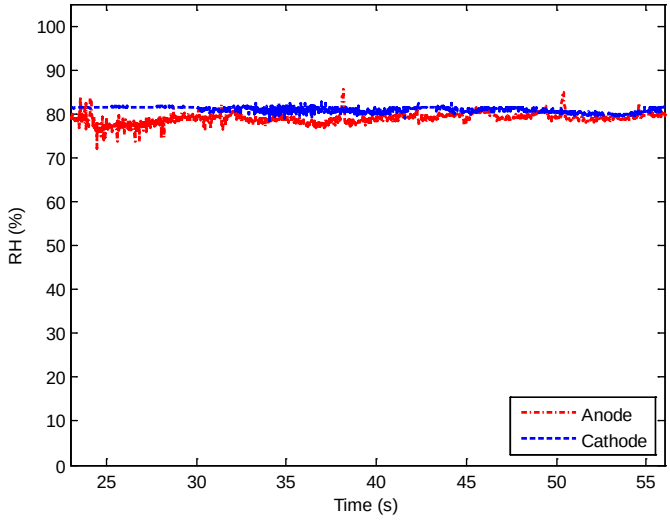

Figure 6.16: Anode and cathode inlet RHs.

The above simulations suggest that channel flooding happens in the anode side that increases the current density due to the fuel cell active area being covered by the

liquid water in the channel. The escalation of current density increases the voltage losses significantly, particularly the ohmic loss represented in Equation 5.57. Enlarging the orifice opening of the anode outlet valve can reduce flooding in the channel considerably without having significant voltage loss due to the reduced reactant gas pressure. A control scheme can be developed to adjust the orifice opening to optimize the fuel cell performance.

A similar application of control can also be used to adjust the cathode orifice opening. In Figure 6.17, it can be seen that the membrane water content can be improved by increasing the cathode channel RH shown in Figure 6.15. A control of cathode orifice opening can regulate the cathode pressure such that it is close to saturation vapor pressure but does not exceed it to cause condensation.

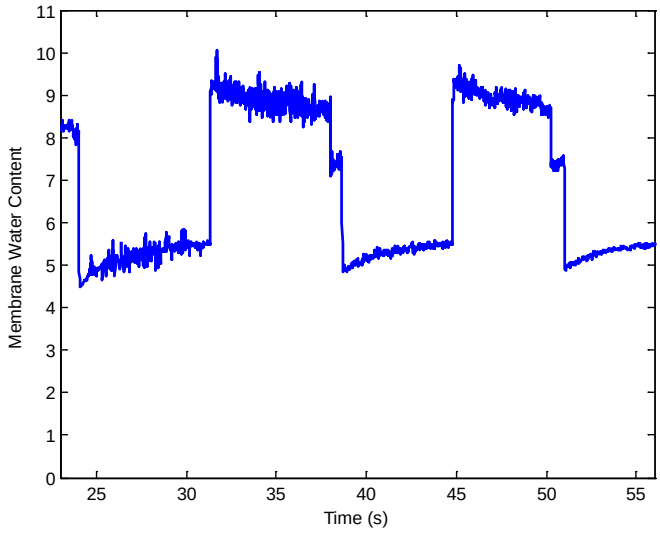

Figure 6.17: Model predictions of membrane water content.

6.5 UTILIZATION OF THE MODEL FOR DEAD-ENDED OPERATION

A full utilization of hydrogen fuel is desirable when using PEM fuel cells. In addition, high purity hydrogen gas is generally required to prevent platinum poisoning for the fuel cell to have a good reliability and longevity. Currently, the price of hydrogen gas is still higher than that of gasoline equivalent for combustion engines. In order to minimize the hydrogen fuel wasted, a dead–ended anode configuration is applied where the anode outlet is closed for a longer period of time and opened for a short period of time intermittently at a certain cycle period. This configuration is also useful to purge any liquid water build up in the anode gas channel.

Simulation results of dead–ended anode configuration are presented in the following subsections to show the voltage response during start–up and step changing of current demand. The inputs are set according to Table 6.2 in the following.

Input Variables	Symbol	Quantity	Units
Anode Inlet Temperature	$T_{an,in}$	333	K
Cathode Inlet Temperature	$T_{ca,in}$	333	K
Stack Temperature	T_{st}	333	K
Cathode Inlet Gas Flow	$\dot{v}_{ca,in}$	3.24e–4	kg/m^3
Anode Inlet Pressure	$p_{an,in}$	120	kPa
Cathode Inlet Pressure	$p_{an,in}$	120	kPa
Anode Inlet Gas Relative Humidity	$RH_{an,in}$	0	%
Cathode Inlet Gas Relative Humidity	$RH_{ca,in}$	100	%

Table 6.2: Inputs of the dead–ended anode simulation.

6.5.1 Start–up Response

In this section a start–up response is presented where initially there is no liquid water in the porous media and the gas channels. The simulation focuses on the effect of liquid water accumulation as the time increases to the fuel cell output voltage during dead–ended anode with purging cycle. Figures 6.18 to 6.24 with the magnification subplots on the right hand side show the response of the fuel cell during start–up.

A constant 10 Amps stack current load is applied and a 6 second purging event is performed every 1 minute cycle. To observe the flooding effect in this configuration, dry hydrogen gas is fed in the anode inlet to induce back diffusion of the water in the membrane. To show a more general performance, the cell voltage which represents the average of individual cell voltages is plotted rather than the stack voltage. The cell voltage response is shown in Figure 6.18. As the time increases the liquid water in the porous media accumulates and increases the resistance of the reactant gas flow. Additionally due to condensation, liquid water build up in the anode channel, as shown in Figure 6.19, also contributes to decreasing the cell voltage by reducing the fuel cell active area, described in Equation 5.53, which defined as the apparent current density. At time longer than 5 minutes, the cell voltage reaches a steady state cycle. This is mainly due to the increasing saturation levels in the cathode GDL and CL during start–up that is shown in Figure 6.23. As a consequence, the oxygen concentration is reduced due to resistance gas flow by the liquid present in the GDL and CL (second subplot of Figure 6.20).

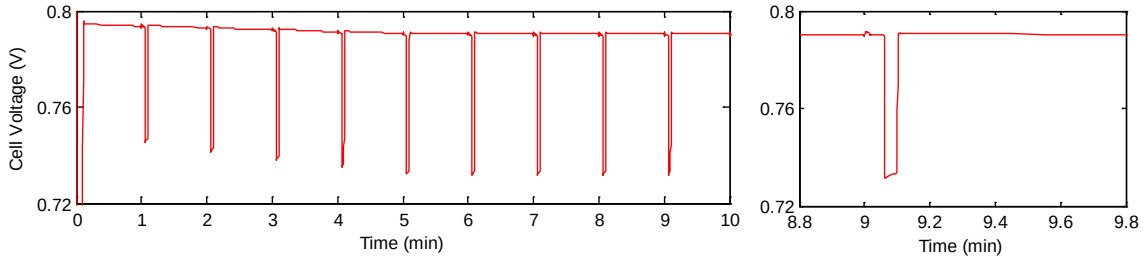

Figure 6.18: Dead–ended anode cell voltage during start–up.

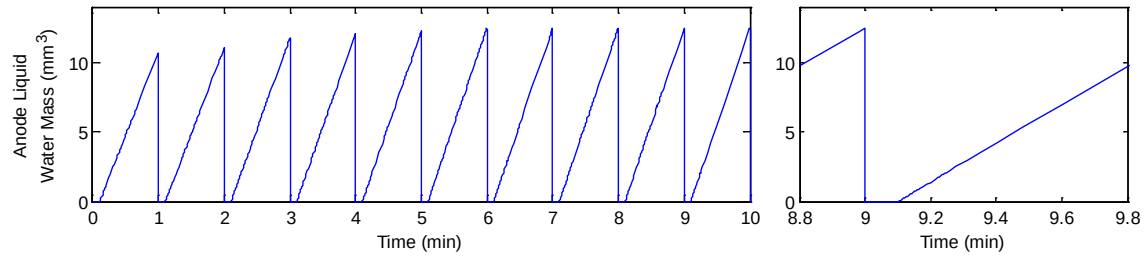

Figure 6.19: Liquid water accumulation in the anode channel during start–up.

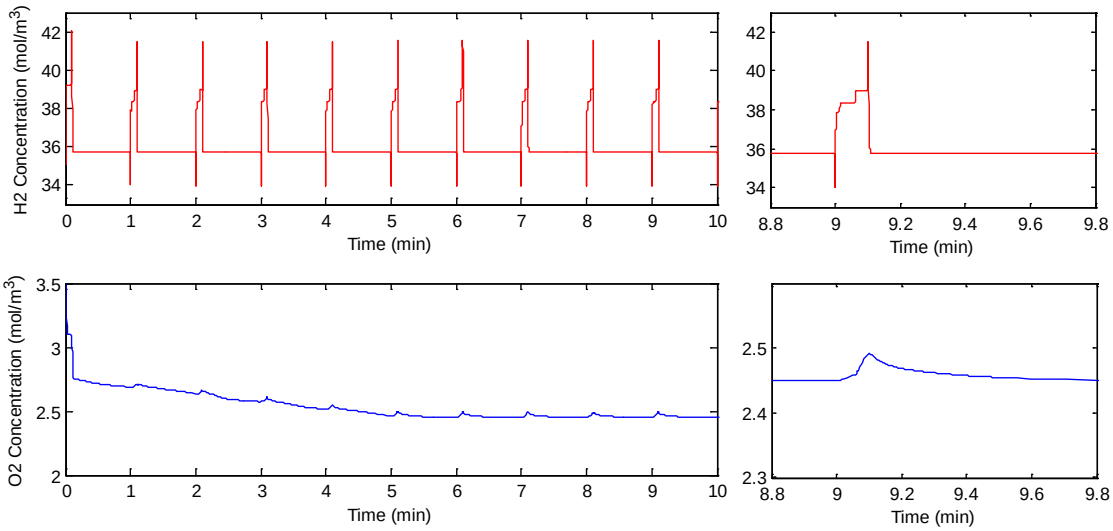

Figure 6.20: Hydrogen and oxygen concentrations in the CLs during start–up.

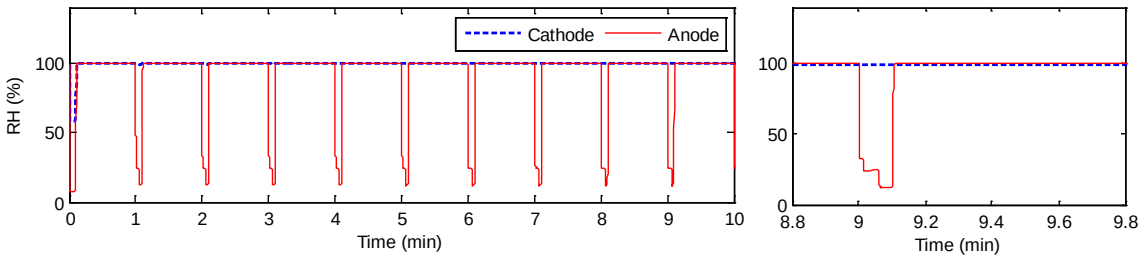

Figure 6.21: Relative humidity in the anode and cathode channels during start–up.

A sudden drop of the cell voltage is seen during the purges. When the anode outlet valve is opened during the purge, the pressure in the anode decreases and the gas flow increases. The liquid water in the anode channel is immediately evaporated and taken away by the gas stream, as shown in Figure 6.19. Following that the liquid water in the anode GDL is also gradually evaporated to zero saturation level, as shown in Figure 6.22 subplot 1. These decreases the vapor concentration i.e. RH in the anode channel and consequently the water in the cathode side is more back diffused to the anode side, causing the cathode channel RH and liquid water saturation in the cathode porous media also decrease and hence reduce the membrane conductivity.

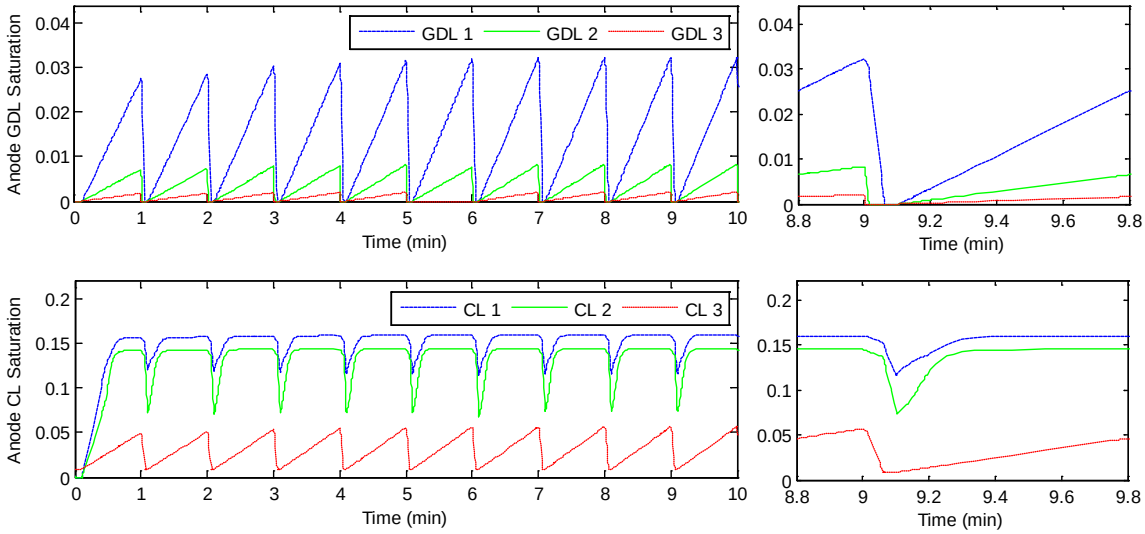

Figure 6.22: Saturation levels in the anode GDL and CL during start–up.

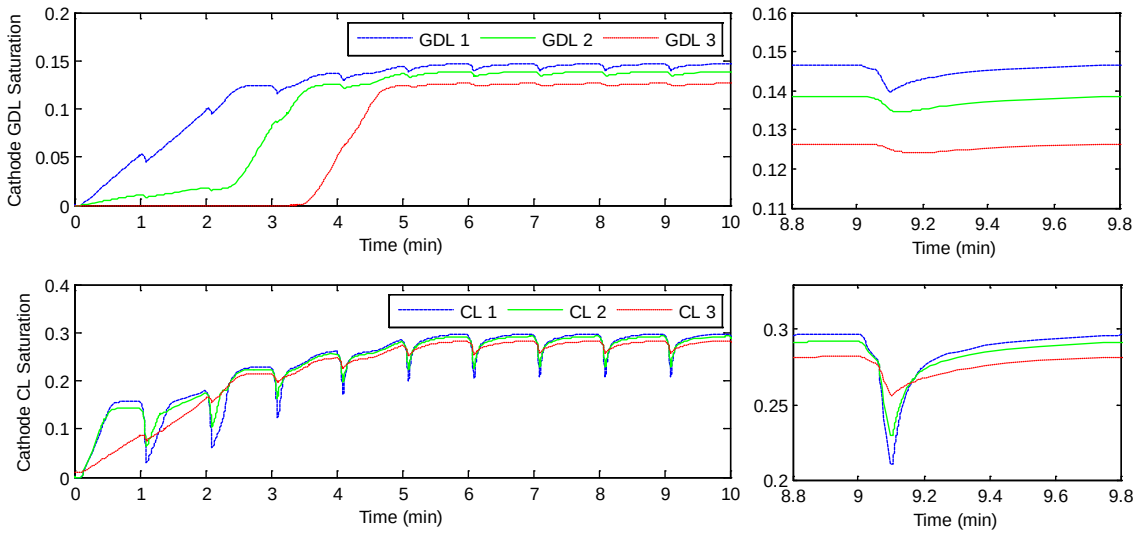

Figure 6.23: Saturation levels in the cathode GDL and CL during start–up.

Shown in subplot 2 of Figure 6.23, the liquid water saturation at cathode CL section 1 (the layer section next to the membrane) has a sharper drop than that at the CL section 2 and 3. This indicates the back diffusion of water from the cathode side to the

anode side. Although the hydrogen and oxygen concentrations increase during the purge (Figure 6.20), the liquid water in the anode channel is removed completely, and the liquid water saturations in the porous media decrease, they do not improve the cell voltage that much to compensate the cell voltage drop caused by the reduced membrane conductivity during the purge.

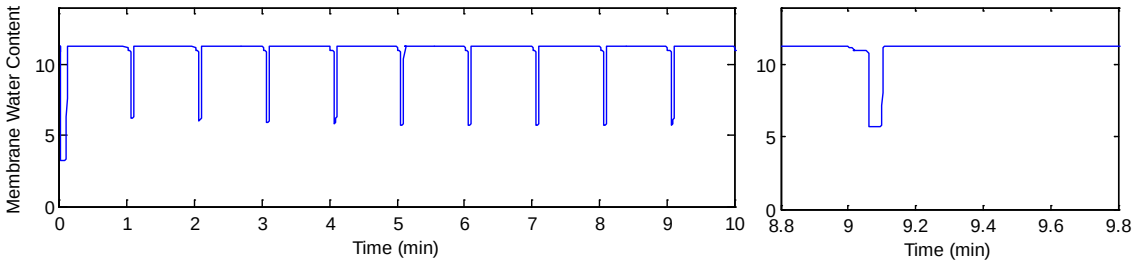

Figure 6.24: Membrane water content during start–up.

The membrane conductivity shown in Figure 6.24, has a very significant impact on the cell voltage. When there is liquid water in the porous media, it helps to humidify the gas flow by evaporation whenever the gas is not fully saturated. Therefore it helps the membrane humidification to keep its conductivity high. This can be seen from the anode GDL saturation; when the saturation drops to zero the anode RH has a very significant drop also.

After the purge valve is closed, the cell voltage is recovered and then slowly reduced due to the liquid water accumulation in the anode channel and the decreasing oxygen concentration. The oxygen concentration in CL is exponentially decaying which is relevant with the increasing liquid water saturations in the GDL and CL that reduce the oxygen flux.

6.5.2 Step Response

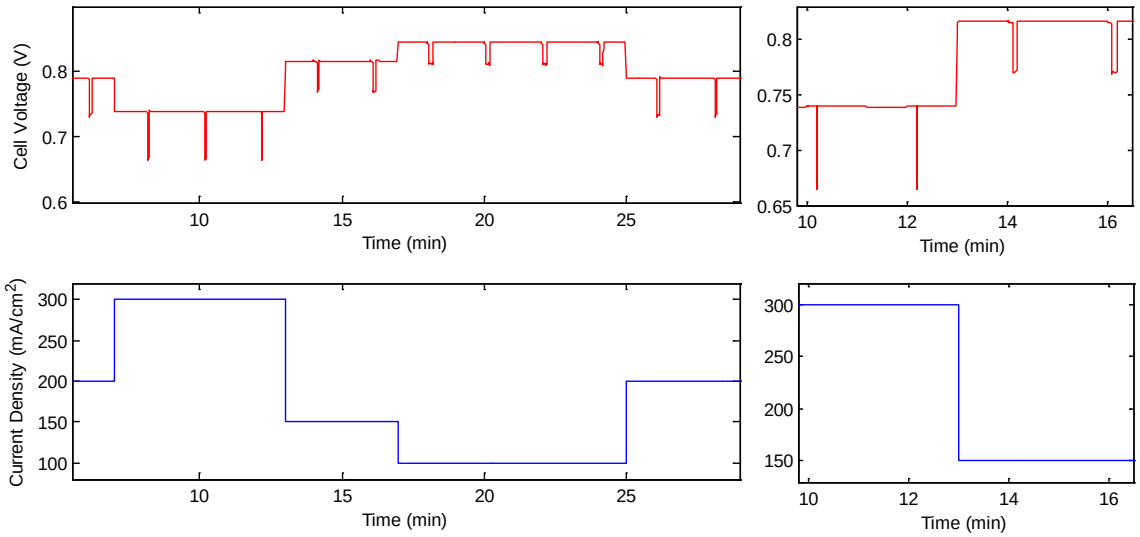

Figure 6.25: Step response cell voltage.

Figure 6.25 shows the step response of the dead ended anode configuration. The cycle time is set to120 seconds with 10 seconds of purging time. The stack current is step changed ranging from 5 to 15 Amps or current density of 100 to 300 mA/cm^2. The cathode inlet gas flow is set to stoichiometry of two.

The magnified subplots in the right hand side of Figures 6.25 to 6.31 are shown when the current density changes from 300 to 150 mA/cm^2. During the change, the cell voltage increases due to the increases of oxygen and hydrogen concentrations which happen because of the reduced water generation since the current density is lowered. Therefore the liquid water saturation and accumulation in the anode channel are also reduced leading to increases the gas reactant and oxidant flows. The vapor concentration has a slight decrease that it does not cause any significant degradation of the cell voltage. There is no overshoot or slow increase during the step change of the cell voltage noticeably. This is because the cathode inlet gas flow is assumed to change

instantaneously and the cathode volume is small that the pressure change happens fast. For the future work, a compressor to pressurize the cathode inlet and an inlet manifold can be added into the system to better model the system response.

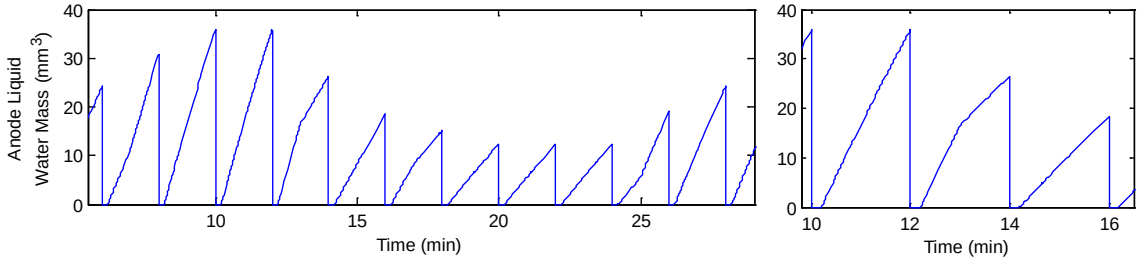

Figure 6.26: Step response liquid water accumulation in the anode channel.

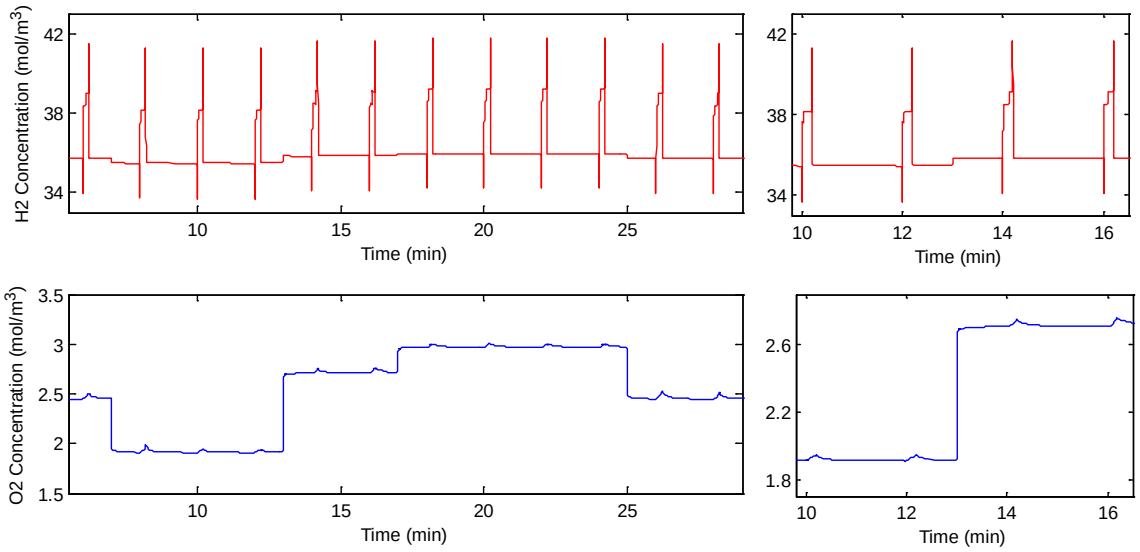

Figure 6.27: Step response hydrogen and oxygen concentrations in the CLs.

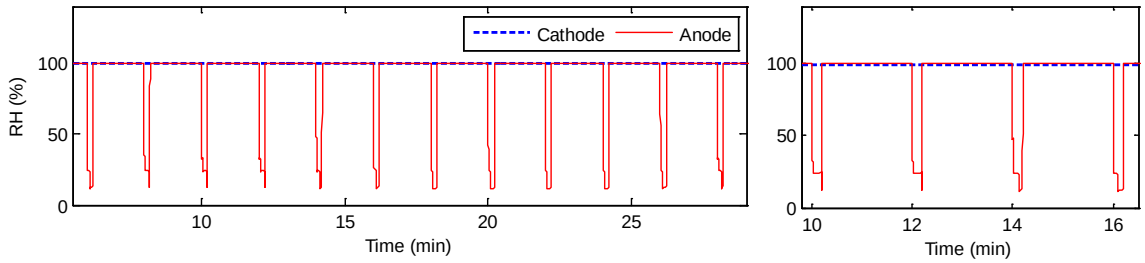

Figure 6.28: Step response relative humidity in the anode and cathode channels.

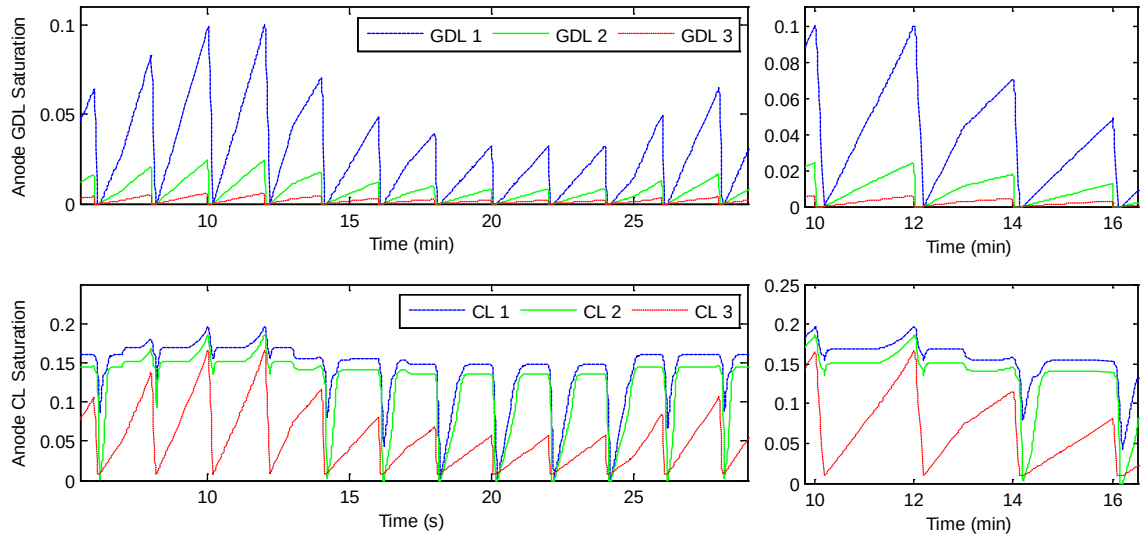

Figure 6.29: Step response saturation levels in the anode GDL and CL.

Looking at a cycle of current density at 300 mA/cm^2 and at time around 12 minutes in the magnified subplot on the right hand side of Figure 6.29, the liquid water saturation in the anode CL 1 and CL 2 starts to increase even higher after a short period of steady saturation level and before the purge valve is opened. The liquid water flow, described in Equation 5.14, in the anode CL reaches the limit to transport the liquid water from higher saturation to lower saturation. Due to the higher water generation and back diffusion at higher current density, liquid water accumulation in the anode CL increases

unboundedly until the purge valve is opened. The liquid saturations in the cathode porous media have only slight jumps, indicating that most of the water produced by the reaction is back diffused to the anode side. Notice that the voltage drops at the 300 mA/cm^2 is narrower in time than that at the 150 mA/cm^2, indicating that the higher current density the more time is needed for purging time to remove the excess water in the system.

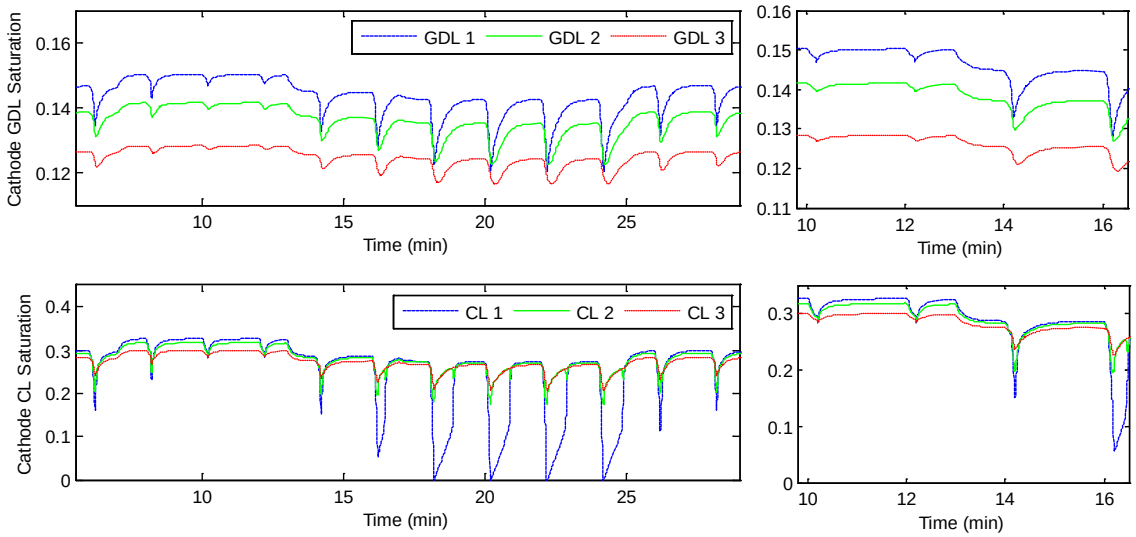

Figure 6.30: Step response saturation levels in the cathode GDL and CL.

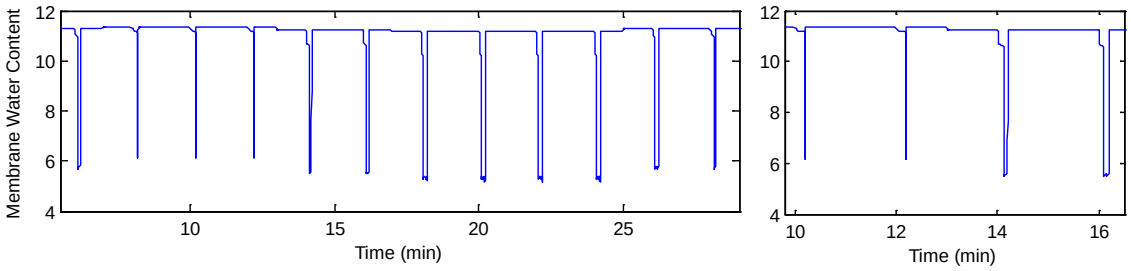

Figure 6.31: Step response membrane water content.

The membrane water content in Figure 6.31 shows that the membrane conductivity has similar level for every current load applied outside the purging event.

The back diffusion and flooding in the anode side help keeping the anode relative humidity and membrane water content high to sustain high hydrogen proton conductivity.

The trend of the transient responses of the model has similar behavior of Reference 87. The main difference is in the liquid water saturation level in the GDL since the CL is added in the model. The cell voltage output is further reduced due to the flooding effect in CL compared to only accounting the flooding effect in GDL. The saturation level in the CL is higher than that in the GDL due to different properties and hydrophobicity of the two materials. In steady state, the performance and the liquid saturation are comparable of Reference 69. Note that in this model, the cathode inlet stoichiometry of 2 was used, where stoichiometry of 2 to 3 was used in the above references, thus the performance increased was expected.

Chapter 7: Conclusion and Future Work

7.1 CONCLUSION

A control oriented thermal model was developed for PEM fuel cells during this research. This model predicts the dynamic thermal and voltage response of the fuel cell system. This model was experimentally validated. Even though the model is a lumped parameter model with a low order, the model can be used to provide a sufficiently accurate prediction of the cathode outlet temperature and the stack voltage. Analysis results based on the model indicate that there exists a relatively small effect of spatial temperature variations on the bulk flow temperature of the anode and cathode. Formulation of this model enables the development of control algorithms to achieve optimal thermal management and stack performance.

In order to find a suitable control framework for a fuel cell stack, relative gain array (RGA) analysis was performed. The RGA analyses results suggest that single–input single–output (SISO) control methods will be valid for the fuel cell stack system which does not include auxiliary components. A multi-input multi-output (MIMO) control framework is necessary for fuel cells with auxiliary components, such as compressor or blower, to achieve an optimal performance.

Water management has been considered as one of the primary challenges for PEM fuel cell technology. The water dynamics inside a catalyst layer plays a critical role for the system performance and the durability of the electrode. In order to understand the water dynamics inside a PEM fuel cell, especially inside the catalyst layer (CL), a two–phase flow in porous media was modeled and experimentally verified. This model accounts the effect of the liquid water on fuel cell performance. The addition of CLs and application of empirically derived porous media model improve the accuracy of the model. This finding is in good agreement with other analysis results in the literature.

The saturation level in the CL is higher than that in the GDL due to different properties and hydrophobicity of the two materials. The cell voltage output is further reduced due to the flooding effect in CL compared to only accounting the flooding effect in GDL. In contrast, simulation results indicate that the presence of the liquid water in the porous media improves the membrane humidification to maintain hydrogen proton conductivity when the relative humidity less than its maximum. The model predictions provide much insights of the water behavior inside the fuel cell during operation.

Since the water, humidification and the thermal behavior are closely related, the two–phase flow in porous media model and thermal model are indispensable and must be integrated so that a comprehensive understanding and a control–oriented modeling tool for a PEM fuel cell stack can be made to achieve optimum PEM fuel cell performance.

7.2 CONTRIBUTION

PEM fuel cells are highly regarded as clean energy option for future power generation. Tremendous improvement has been achieved, yet there is still a need to further advance the technology. Numerous publications have discussed the importance of thermal and water management to achieve high performance and reliability of PEM fuel cells. However, for real–time control purpose, only few have considered to describe the dynamic thermal and humidification phenomena. The thermal models are usually standalone models and not integrated with the mass transfer aspect of a fuel cell system. This research fills in the knowledge gap through integrating the dynamic thermal model with two–phase flow porous media model.

The contributions of this research are:

- A control oriented thermal model was developed and experimentally validated for a PEM fuel cell. This model helps to define control formulation and gives insight how the temperatures affects the fuel cell performance.
- RGA analyses were performed and demonstrated that the fuel cell stack inclined towards to be decoupled and can be controlled by using SISO control design. However when adding auxiliary components into the fuel cell system, RGA analysis results showed that the thermal and mass dynamics are coupled and require MIMO control design. The RGA analysis results provide a novel enabling tool for control design of fuel cell stack and fuel cell system.
- A catalyst layer model was developed and incorporated into a fuel cell stack model by employing an empirically derived capillary flow. The modeling result was verified based on experimental data. It increases the modeling accuracy and provides more detailed insights of water balance during and relative humidity dynamics inside a PEM fuel cell stack.

7.3 FUTURE WORK

Combining the thermal model with the porous media model could enhance our understanding on water balance inside PEM fuel cells and sets the foundation for subsequent control design. Many dynamic models of the PEM fuel cells have been reported in the literature. However reports on experiments to validate such models are still scarce. The developed thermal model shows a good agreement with the data. However, due to the test stand constraints, the experiments were conducted at lower current density. The model still needs to be validated when large current demand is applied. Similar concern applies to modeling the two–phase flow in porous media.

Experiments on high current density will be conducted in the future to provide a comprehensive view of the thermal and water dynamics inside a PEM fuel cell. It will ultimately provide an enabling tool for real time control.

The RGA analysis serves as a tool to quantitatively determine whether a decentralized SISO controller would achieve the control goal for a system with coupled heat and mass transfer dynamics. Depending on the analysis result, control design can be applied accordingly to make PEM fuel cells operate in optimum conditions and thus can improve the performance and reliability. For a PEM fuel cell system that consists of not only the fuel cell stack but also other auxiliary components, traditionally SISO controllers are designed to achieve the operational goal. However, this research result suggested that a MIMO control is inevitably the controller structure for the entire PEM fuel cell system. MIMO control techniques will be explored in the future to seek improved performance of an overall fuel cell system.

Appendix A

Parameters, Symbols, and Definitions

Symbol	Definition	Quantity	Units	Reference
A_{fc}	Fuel cell active area	0.005	m^2	
b_{11}	Ohmic resistance parameter	0.005139		98
b_{12}	Ohmic resistance parameter	0.00326		98
b_2	Ohmic resistance parameter	0.00326		98
$C_{p_{air}}$	Specific heat of air at constant pressure	1004	J kg^{-1} K^{-1}	91
$C_{v_{air}}$	Specific heat of air at constant volume	718	J kg^{-1} K^{-1}	91
$C_{p_{H_2}}$	Specific heat of hydrogen at constant pressure	14830	J kg^{-1} K^{-1}	91
$C_{v_{H_2}}$	Specific heat of hydrogen at constant volume	1071	J kg^{-1} K^{-1}	91
$C_{p_{N_2}}$	Specific heat of nitrogen at constant pressure	1040.9	J kg^{-1} K^{-1}	91
$C_{v_{N_2}}$	Specific heat of nitrogen at constant volume	743.9	J kg^{-1} K^{-1}	91
$C_{p_{O_2}}$	Specific heat of oxygen at constant pressure	923	J kg^{-1} K^{-1}	91
$C_{v_{O_2}}$	Specific heat of oxygen at constant volume	663	J kg^{-1} K^{-1}	91
$C_{p_{vap}}$	Specific heat of water vapor at constant pressure	1872.3	J kg^{-1} K^{-1}	91
$C_{v_{vap}}$	Specific heat of water vapor at constant volume	1409.5	J kg^{-1} K^{-1}	91
C_{liq}	Specific heat of liquid water	4181.3	J kg^{-1} K^{-1}	91
D_{H_2}	Hydrogen diffusion coefficient	114	mm^2 s^{-1}	33
D_{O_2}	Oxygen diffusion coefficient	30.3	mm^2 s^{-1}	33
D_v	Vapor diffusion coefficient	34.5	mm^2 s^{-1}	33
E_c	Activation energy	66	kJ mol^{-1}	102
F	Faraday's constant	96485	C mol^{-1}	
ΔH	Enthalpy difference (water in vapor phase)	–228740	J mol^{-1}	87

Symbol	Definition	Quantity	Units	Reference
i_{loss}	Loss current density	1	mA cm^{-2}	102
$k_{an,out}$	Anode outlet orifice constant	1.2e–6	m s	
$k_{ca,out}$	Cathode outlet orifice constant	3e–6	m s	
$k_{an,purge}$	Anode outlet manifold orifice constant	10e–6	m s	
$K_{l,GDL}$	GDL liquid water absolute permeability	2.55e–13	m^2	69
$K_{l,CL}$	CL liquid water absolute permeability	1e–15	m^2	69
M_{H_2}	Hydrogen molecular weight	0.002	kg mol^{-1}	
M_{O_2}	Oxygen molecular weight	0.032	kg mol^{-1}	
M_{N_2}	Nitrogen molecular weight	0.028	kg mol^{-1}	
M_{H_2O}	Water molecular weight	0.018	kg mol^{-1}	
$M_{mb,dry}$	Membrane dry equivalent weight	1.0	kg mol^{-1}	87
n_{cell}	Number of cells in stack	30		
p_0	Standard state pressure	1	atm	60
R	Universal gas constant	8.314	mol^{-1} K^{-1}	
ΔS	Entropy difference (water in vapor phase)	–44.43	J mol^{-1} K^{-1}	102
t_{GDL}	Compressed GDL thickness	0.5	mm	69
t_{CL}	Compressed CL thickness	16	microns	69
t_{mb}	PEMFC membrane thickness	50	microns	
t_{wl}	Water layer thickness	0.12	mm	87
T_0	Standard state temperature	298.15	K	102
y_{O_2}	Oxygen mole fraction in air	0.21		60
ε_{CL}	CL porosity	0.12		69
ε_{GDL}	GDL porosity	0.5		69
γ	Volumetric condensation rate	900	s^{-1}	33
$\rho_{mb,dry}$	Membrane dry density	1900	kg m^{-3}	87
ρ_{col}	Liquid water coolant density	997	kg m^{-3}	91
σ	Stefan Boltzmann constant	5.67e–8	W/m^{-2} K^{-4}	58

Appendix B

Fuel Cell Stack Dimension

Anode (single cell):	
Active area	70.75 x 70.75 = 5000 mm^2
Channel length	2400.3 mm
Channel width	0.864 mm
Channel depth	0.56 mm
Total exposed area	2400.3 x 0.864 = 2133.87 mm^2
Exposed to active ratio	2133.87 / 5000 x 100% = 42.7%
Total channel volume	2400.3 x 0.864 x 0.056 = 1161.36 mm^3
Cathode (single cell):	
Active area	70.75 x 70.75 = 5000 mm^2
Channel length	1768.8 mm
Channel width	1.5748 mm
Channel depth	1.27 mm
Total exposed area	1768.8 x 1.5748 = 2785.5 mm^2
Exposed to active ratio	2785.5 / 5000 x 100% = 55.7%
Total channel volume	1768.8 x 1.5748 x 1.27 = 3537.59 mm^3
Fuel cell stack body (graphite):	
Plate area	127 x 127 = 16129 mm^2
Anode plate thickness	5.6 mm
Cathode plate thickness	5.6 mm
Coolant plate thickness	5.5 mm
Total surface area to ambient	127 x 16.6125 x 30 x 4 sides = 254508 mm^2
Coolant (single cell):	
Channel length	381 mm
Channel width	2.54 mm
Channel depth	1.27 mm
Total channel volume	381 x 2.54 x 1.27 = 1229 mm^3

Appendix C

Thermal Model Linearization Results

Model linearization was performed using the linearize function of Matlab's Control System Toolbox [115].

This appendix shows the linearized fuel cell thermal model in state space representation as follows.

$$\dot{x}(t) = Ax(t) + Bu(t) \tag{C.1}$$

$$y(t) = Cx(t) + Du(t) \tag{C.2}$$

There are 2 inputs, 2 outputs and 8 state variables. The Inputs are the cathode inlet air flow (u1) and inlet water coolant (u2). The outputs are the stack voltage (y1) and cathode outlet temperature (y2). The states are the outlet manifold pressure (x1), hydrogen mass (x2), anode flow out temperature (x3), nitrogen mass (x4), oxygen mass (x5), cathode flow out temperature (x6), coolant flow out temperature (x7), and fuel cell body temperature (x8).

Linearization at operating conditions 293K and 0.15 Amps.

A

-3430	0	0	4.219E+10	3.693E+10	2.349E+04	0	0
0	5.411	-3.31E-07	0	0	0	0	0
0	-7.106e+09	-8078	0	0	0	0	7459
2.595E-09	0	0	-7.935	-3.643	-3.395E-06	0	0
5.739E-11	0	0	-0.1012	-3.44	-7.509E-08	0	0
0.007422	0	0	-2.230E+08	-1.95E+08	-4563	0	5667
0	0	0	0	0	0	-17.14	16.87
0	-6.907	0.02813	0.2741	-3.57	0.01921	0.2631	-0.3161

B

0	0
0	0
0	0
0.6888	0
0.2092	0
2.581E+06	0
0	0.2672
0	0

C

0	4.569E+05	0.001341	-1.813E+04	2.361E+05	-0.00924	0	0.01653
0	0	0	0	0	0	1	0

D

0	0
0	0

Linearization at operating conditions 293K and 5 Amps.

A

-3430	0	0	4.219E+10	3.693E+10	2.349E+04	0	0
0	5.411	-3.306E-07	0	0	0	0	0
0	-7.09e+09	-8076	0	0	0	0	7459
2.595E-09	0	0	-7.935	-3.643	-3.395E-06	0	0
5.739E-11	0	0	-0.1012	-3.44	-7.509E-08	0	0
0.007422	0	0	-2.257E+08	-1.998E+08	-4564	0	5667
0	0	0	0	0	0	-17.14	16.87
0	-230.2	0.02813	9.137	-361.6	0.01922	0.2631	-0.3161

B

0	0
0	0
0	0
0.6888	0
0.2092	0
2.581E+06	0
0	0.2672
0	0

C

0	4.569E+05	0.001341	-1.813E+04	7.176E+05	-0.007824	0	0.06617
0	0	0	0	0	0	1	0

D

0	0
0	0

Linearization at operating conditions 293K and 10 Amps.

A

-3430	0	0	4.219E+10	3.693E+10	2.349E+04	0	0
0	5.411	-3.306E-07	0	0	0	0	0
0	-7.09e+09	-8076	0	0	0	0	7459
2.595E-09	0	0	-7.935	-3.643	-3.395E-06	0	0
5.739E-11	0	0	-0.1012	-3.44	-7.509E-08	0	0
0.007422	0	0	-2.284E+08	-2.022E+08	-4565	0	5667
0	0	0	0	0	0	-17.14	16.87
0	-460.5	0.02813	18.27	-917.3	0.01922	0.2631	-0.3162

B

0	0
0	0
0	0
0.6888	0
0.2092	0
2.581E+06	0
0	0.2672
0	0

C

0	4.569E+05	0.001341	-1.813E+04	7.176E+05	-0.007824	0	0.06617
0	0	0	0	0	0	1	0

D

0	0
0	0

Linearization at operating conditions 293K and 15 Amps.

A

-3430	0	0	4.219E+10	3.693E+10	2.349E+04	0	0
0	5.411	-3.306E-07	0	0	0	0	0
0	-7.056e+09	-8073	0	0	0	0	7459
2.595E-09	0	0	-7.935	-3.643	-3.395E-06	0	0
5.739E-11	0	0	-0.1012	-3.44	-7.509E-08	0	0
0.007422	0	0	-2.311E+08	-2.046E+08	-4566	0	5667
0	0	0	0	0	0	-17.14	16.87
0	-690.7	0.02813	27.41	-1508	0.01922	0.2631	-0.3163

B

0	0
0	0
0	0
0.6888	0
0.2092	0
2.581E+06	0
0	0.2672
0	0

C

0	4.569E+05	0.001341	-1.813E+04	9.977E+05	-0.007	0	0.09559
0	0	0	0	0	0	1	0

D

0	0
0	0

Linearization at operating conditions 318K and 0.15 Amps.

A

-3430	0	0	4.219E+10	3.693E+10	2.349E+04	0	0
0	5.411	-3.306E-07	0	0	0	0	0
0	-7.106e+09	-8078	0	0	0	0	7459
2.595E-09	0	0	-7.935	-3.643	-3.395E-06	0	0
5.739E-11	0	0	-0.1012	-3.44	-7.509E-08	0	0
0.007422	0	0	-2.230E+08	-1.974E+08	-4566	0	5667
0	0	0	0	0	0	-17.14	16.87
0	-690.7	0.02813	0.2741	-3.57	0.01921	0.2631	-0.3161

B

0	0
0	0
0	0
0.6888	0
0.2092	0
2.581E+06	0
0	0.2672
0	0

C

0	4.569E+05	0.001341	-1.813E+04	2.361E+05	-0.00924	0	0.01653
0	0	0	0	0	0	1	0

D

0	0
0	0

Linearization at operating conditions 318K and 5 Amps.

A

-3430	0	0	4.219E+10	3.693E+10	2.349E+04	0	0
0	5.411	-3.306E-07	0	0	0	0	0
0	-7.056e+09	-8073	0	0	0	0	7459
2.595E-09	0	0	-7.935	-3.643	-3.395E-06	0	0
5.739E-11	0	0	-0.1012	-3.44	-7.509E-08	0	0
0.007422	0	0	-2.310E+08	-1.974E+08	-4566	0	5667
0	0	0	0	0	0	-17.14	16.87
0	-690.7	0.02813	27.41	-3.57	0.01921	0.2631	-0.3161

B

0	0
0	0
0	0
0.6888	0
0.2092	0
2.581E+06	0
0	0.2672
0	0

C

0	4.569E+05	0.001341	-1.813E+04	2.361E+05	-0.00924	0	0.01653
0	0	0	0	0	0	1	0

D

0	0
0	0

Linearization at operating conditions 318K and 10 Amps.

A

-3430	0	0	4.219E+10	3.693E+10	2.349E+04	0	0
0	5.411	-3.306E-07	0	0	0	0	0
0	-7.056e+09	-8073	0	0	0	0	7459
2.595E-09	0	0	-7.935	-3.643	-3.395E-06	0	0
5.739E-11	0	0	-0.1012	-3.44	-7.509E-08	0	0
0.007422	0	0	-2.284E+08	-2.022E+08	-4565	0	5667
0	0	0	0	0	0	-17.14	16.87
0	-460.5	0.02813	18.27	-917.3	0.01921	0.2631	-0.3162

B

0	0
0	0
0	0
0.6888	0
0.2092	0
2.581E+06	0
0	0.2672
0	0

C

0	4.569E+05	0.001341	-1.813E+04	9.101E+05	-0.007258	0	0.0863
0	0	0	0	0	0	1	0

D

0	0
0	0

Linearization at operating conditions 318K and 15 Amps.

A

-3430	0	0	4.219E+10	3.693E+10	2.349E+04	0	0
0	5.411	-3.306E-07	0	0	0	0	0
0	-7.056e+09	-8073	0	0	0	0	7459
2.595E-09	0	0	-7.935	-3.643	-3.395E-06	0	0
5.739E-11	0	0	-0.1012	-3.44	-7.509E-08	0	0
0.007422	0	0	-2.311E+08	-2.046E+08	-4566	0	5667
0	0	0	0	0	0	-17.14	16.87
0	-690.7	0.02813	27.41	-1508	0.01922	0.2631	-0.3163

B

0	0
0	0
0	0
0.6888	0
0.2092	0
2.581E+06	0
0	0.2672
0	0

C

0	4.569E+05	0.001341	-1.813E+04	9.977E+05	-0.007	0	0.01653
0	0	0	0	0	0	1	0

D

0	0
0	0

Linearization at operating conditions 343K and 0.15 Amps.

A

-3430	0	0	4.219E+10	3.693E+10	2.349E+04	0	0
0	5.411	-3.306E-07	0	0	0	0	0
0	-7.056e+09	-8073	0	0	0	0	7459
2.595E-09	0	0	-7.935	-3.643	-3.395E-06	0	0
5.739E-11	0	0	-0.1012	-3.44	-7.509E-08	0	0
0.007422	0	0	-2.230E+08	-1.974E+08	-4563	0	5667
0	0	0	0	0	0	-17.14	16.87
0	-690.7	0.02813	27.41	-3.57	0.01921	0.2631	-0.3161

B

0	0
0	0
0	0
0.6888	0
0.2092	0
2.581E+06	0
0	0.2672
0	0

C

0	4.569E+05	0.001341	-1.813E+04	2.361E+05	-0.00924	0	0.01653
0	0	0	0	0	0	1	0

D

0	0
0	0

Linearization at operating conditions 343K and 5 Amps.

A

-3430	0	0	4.219E+10	3.693E+10	2.349E+04	0	0
0	5.411	-3.306E-07	0	0	0	0	0
0	-7.056e+09	-8073	0	0	0	0	7459
2.595E-09	0	0	-7.935	-3.643	-3.395E-06	0	0
5.739E-11	0	0	-0.1012	-3.44	-7.509E-08	0	0
0.007422	0	0	-2.257E+08	-1.998E+08	-4566	0	5667
0	0	0	0	0	0	-17.14	16.87
0	-230.2	0.02813	9.137	-361.6	0.01921	0.2631	-0.3162

B

0	0
0	0
0	0
0.6888	0
0.2092	0
2.581E+06	0
0	0.2672
0	0

C

0	4.569E+05	0.001341	-1.813E+04	7.176E+05	-0.007824	0	0.06617
0	0	0	0	0	0	1	0

D

0	0
0	0

Linearization at operating conditions 343K and 10 Amps.

A

-3430	0	0	4.219E+10	3.693E+10	2.349E+04	0	0
0	5.411	-3.306E-07	0	0	0	0	0
0	-7.056e+09	-8075	0	0	0	0	7459
2.595E-09	0	0	-7.935	-3.643	-3.395E-06	0	0
5.739E-11	0	0	-0.1012	-3.44	-7.509E-08	0	0
0.007422	0	0	-2.284E+08	-2.022E+08	-4565	0	5667
0	0	0	0	0	0	-17.14	16.87
0	-460.5	0.02813	18.27	-917.3	0.01922	0.2631	-0.3162

B

0	0
0	0
0	0
0.6888	0
0.2092	0
2.581E+06	0
0	0.2672
0	0

C

0	4.569E+05	0.001341	-1.813E+04	9.101E+05	-0.007258	0	0.0863
0	0	0	0	0	0	1	0

D

0	0
0	0

Linearization at operating conditions 343K and 15 Amps.

A

-3430	0	0	4.219E+10	3.693E+10	2.349E+04	0	0
0	5.411	-3.306E-07	0	0	0	0	0
0	-7.056e+09	-8073	0	0	0	0	7459
2.595E-09	0	0	-7.935	-3.643	-3.395E-06	0	0
5.739E-11	0	0	-0.1012	-3.44	-7.509E-08	0	0
0.007422	0	0	-2.311E+08	-2.046E+08	-4566	0	5667
0	0	0	0	0	0	-17.14	16.87
0	-690.7	0.02813	27.41	-1508	0.01922	0.2631	-0.3163

B

0	0
0	0
0	0
0.6888	0
0.2092	0
2.581E+06	0
0	0.2672
0	0

C

0	4.569E+05	0.001341	-1.813E+04	9.977E+05	-0.007	0	0.09959
0	0	0	0	0	0	1	0

D

0	0
0	0

Appendix D

Regression Summary

The Microsoft Excel summary output of the regression result presented in Chapter 6 is in the following.

Regression Statistics	
Multiple R	0.999416896
R Square	0.998834131
Adjusted R Square	0.998759566
Standard Error	0.01305076
Observations	13462

Anova

	df	SS	MS	F	Significance F
Regression	4	1963.793656	490.9484141	2882466.612	0
Residual	13458	2.292197845	0.000170322		
Total	13462	1966.085854			

	Coefficients	Standard Error	t Stat	P-value
Intercept	0	#N/A	#N/A	#N/A
X Variable 1	1.294751508	0.00786949	164.5280109	0
X Variable 2	-8.135085165	0.063683471	-127.74249	0
X Variable 3	6.357019181	0.037129499	171.2120907	0
X Variable 4	1.951230007	0.067474395	28.91808091	1.9111E-178

	Lower 95%	Upper 95%	Lower 95.0%	Upper 95.0%
Intercept	#N/A	#N/A	#N/A	#N/A
X Variable 1	1.279326205	1.310176812	1.279326205	1.310176812
X Variable 2	-8.259913697	-8.010256632	-8.259913697	-8.010256632
X Variable 3	6.284240157	6.429798206	6.284240157	6.429798206
X Variable 4	1.818970732	2.083489282	1.818970732	2.083489282

Appendix E

Matlab/Simulink

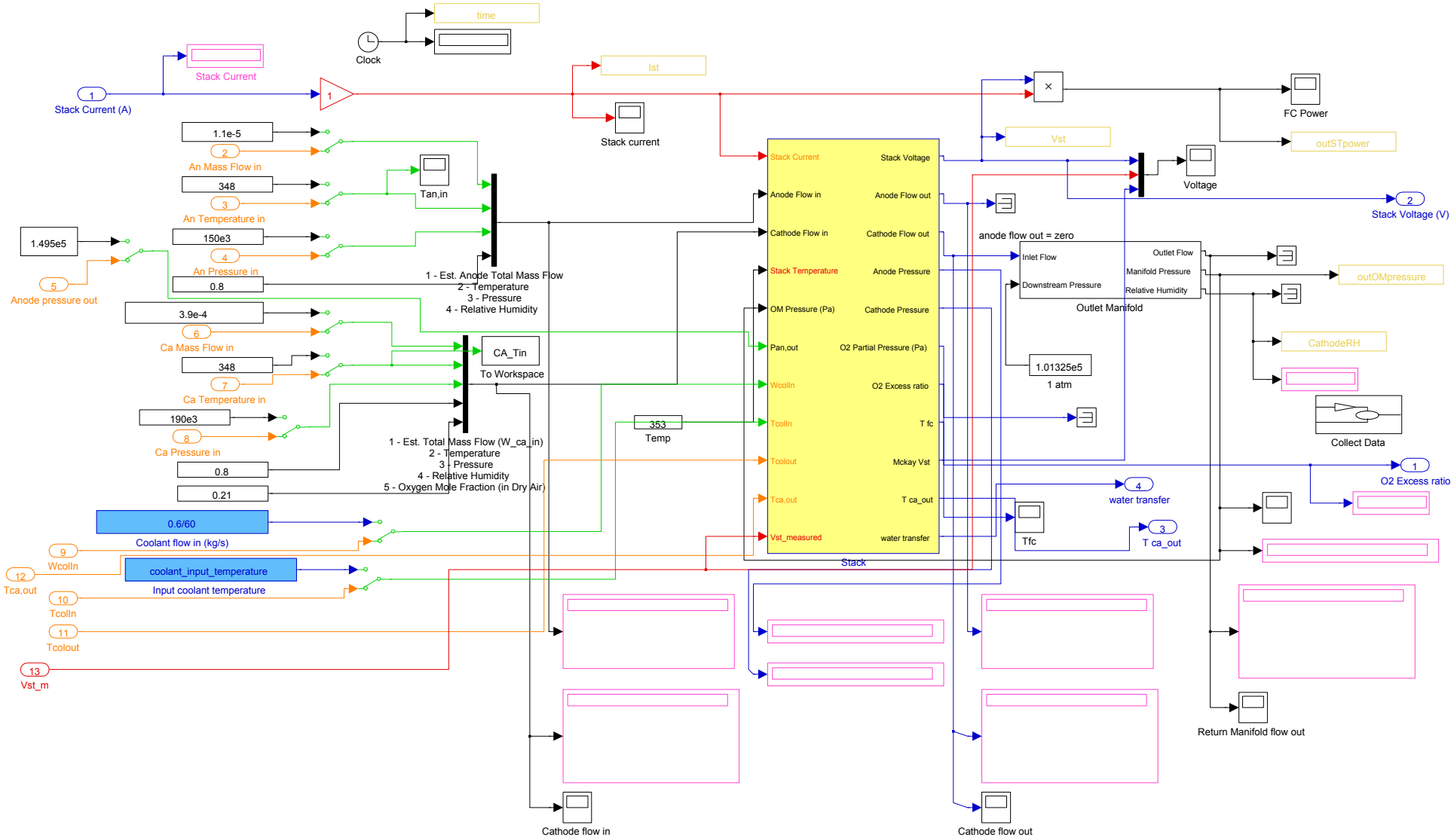
time
Clock
Stack Current
1
Stack Current (A)
Ist
Stack current
1.1e-5
2
An Mass Flow in
348
3
An Temperature in
150e3
4
An Pressure in
0.8
Tan,in
1.495e5
5
Anode pressure out
1 - Est. Anode Total Mass Flow
2 - Temperature
3 - Pressure
4 - Relative Humidity
3.9e-4
6
Ca Mass Flow in
348
7
Ca Temperature in
190e3
8
Ca Pressure in
0.8
0.21
CA_Tin
To Workspace
1 - Est. Total Mass Flow (W_ca_in)
2 - Temperature
3 - Pressure
4 - Relative Humidity
5 - Oxygen Mole Fraction (in Dry Air)
353
Temp
0.6/60
Coolant flow in (kg/s)
9
WcolIn
12
Tca,out
coolant_input_temperature
Input coolant temperature
10
TcolIn
11
Tcolout
13
Vst_m
Stack Current
Anode Flow in
Cathode Flow in
Stack Temperature
OM Pressure (Pa)
Pan,out
WcolIn
TcolIn
Tcolout
Tca,out
Vst_measured
Stack Voltage
Anode Flow out
Cathode Flow out
Anode Pressure
Cathode Pressure
O2 Partial Pressure (Pa)
O2 Excess ratio
T fc
Mckay Vst
T ca_out
water transfer
Stack
Vst
FC Power
outSTpower
Voltage
2
Stack Voltage (V)
anode flow out = zero
Inlet Flow
Downstream Pressure
Outlet Flow
Manifold Pressure
Relative Humidity
Outlet Manifold
outOMpressure
CathodeRH
1.01325e5
1 atm
Collect Data
1
O2 Excess ratio
4
water transfer
Tfc
3
T ca_out
Return Manifold flow out
Cathode flow in
Cathode flow out

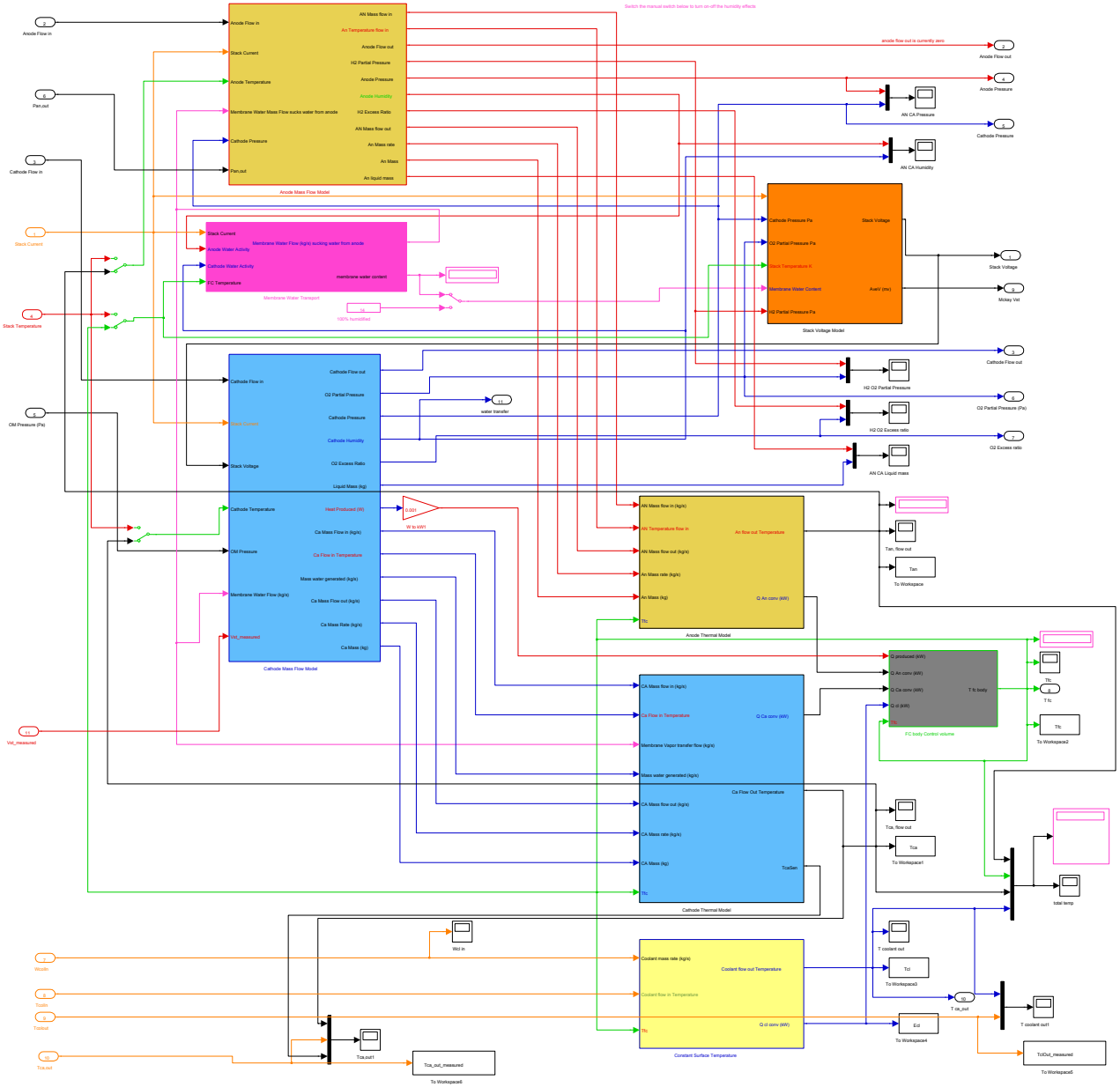
Anode Flow in
Pan,out
Cathode Flow in
Stack Current
Stack Temperature
Cell Pressure (Pa)
Vol_measured
Anode Mass Flow Model
Membrane Water Transport
100% humidified
Cathode Mass Flow Model
Stack Voltage Model
water transfer
W to kW
Anode Thermal Model
FC body Control volume
Cathode Thermal Model
Constant Surface Temperature
Wcl in
Tcl,out
Tca,out
Tcl
Tca
Tfc
Tan
Ecl
Tcl,out
Tca_out_measured
To Workspace
To Workspace1
To Workspace2
To Workspace3
To Workspace4
To Workspace5
To Workspace6
AN CA Pressure
AN CA Humidity
AN CA Liquid mass
H2 O2 Partial Pressure
H2 O2 Excess ratio
Stack Voltage
Mickey Vol
Cathode Flow out
O2 Partial Pressure (Pa)
O2 Excess ratio
Anode Flow out
Anode Pressure
Cathode Pressure
T fc
T coolant out
T coolant out1
total temp
T ca_out

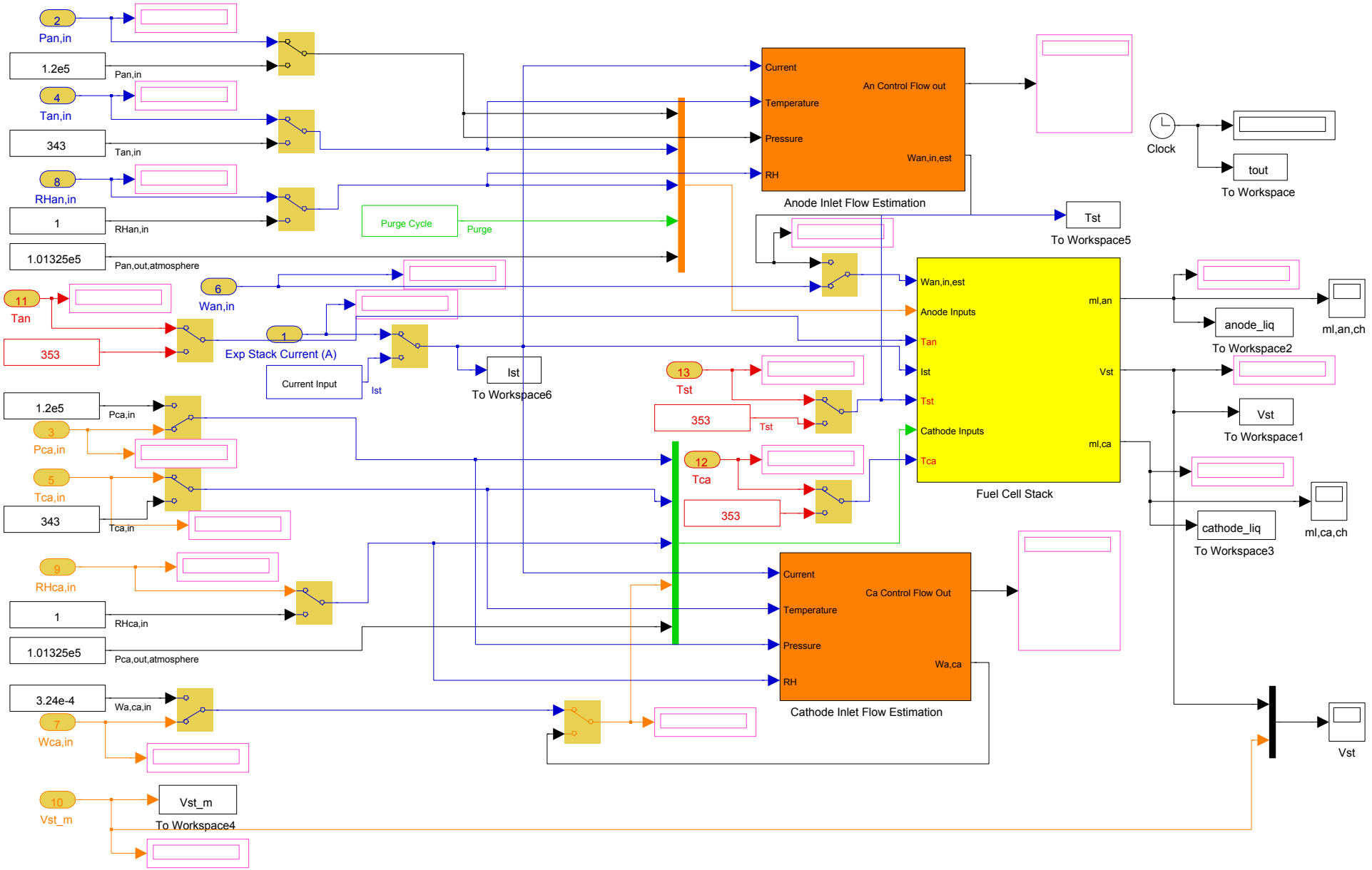
2
Pan,in
1.2e5
Pan,in
4
Tan,in
343
Tan,in
8
RHan,in
1
RHan,in
1.01325e5
Pan,out,atmosphere
Purge Cycle
Purge
Current
Temperature
Pressure
RH
An Control Flow out
Wan,in,est
Anode Inlet Flow Estimation
Clock
tout
To Workspace
Tst
To Workspace5
11
Tan
353
6
Wan,in
1
Exp Stack Current (A)
Current Input
Ist
Ist
To Workspace6
Wan,in,est
Anode Inputs
Tan
Ist
Tst
Cathode Inputs
Tca
ml,an
Vst
ml,ca
Fuel Cell Stack
anode_liq
To Workspace2
ml,an,ch
Vst
To Workspace1
cathode_liq
To Workspace3
ml,ca,ch
13
Tst
353
Tst
12
Tca
353
1.2e5
Pca,in
3
Pca,in
5
Tca,in
343
Tca,in
9
RHca,in
1
RHca,in
1.01325e5
Pca,out,atmosphere
Current
Temperature
Pressure
RH
Ca Control Flow Out
Wa,ca
Cathode Inlet Flow Estimation
3.24e-4
Wa,ca,in
7
Wca,in
10
Vst_m
Vst_m
To Workspace4
Vst

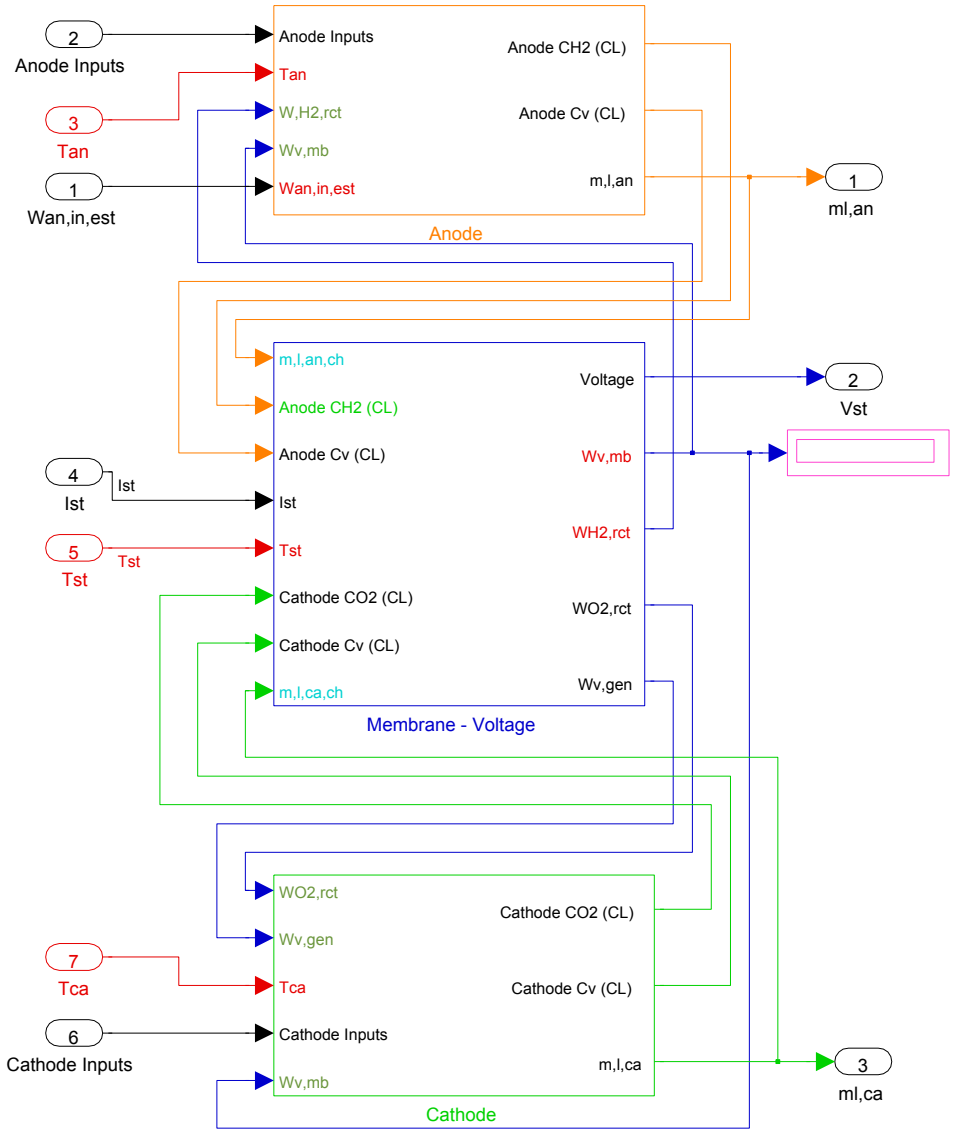
2
Anode Inputs
3
Tan
1
Wan,in,est
Anode Inputs
Tan
W,H2,rct
Wv,mb
Wan,in,est
Anode CH2 (CL)
Anode Cv (CL)
m,l,an
Anode
1
ml,an
m,l,an,ch
Anode CH2 (CL)
Anode Cv (CL)
Ist
Tst
Cathode CO2 (CL)
Cathode Cv (CL)
m,l,ca,ch
Voltage
Wv,mb
WH2,rct
WO2,rct
Wv,gen
Membrane - Voltage
2
Vst
4
Ist
5
Tst
WO2,rct
Wv,gen
Tca
Cathode Inputs
Wv,mb
Cathode CO2 (CL)
Cathode Cv (CL)
m,l,ca
Cathode
7
Tca
6
Cathode Inputs
3
ml,ca

References

[1] The U.S. Department of Energy, Hydrogen production roadmap: Technology Pathway to the Future, United States Department of Energy, US DRIVE, Hydrogen Production Technical Team (HPTT), January 2009.

[2] The U.S. Department of Energy, Hydrogen Production: Overview of Technology Options, United States Department of Energy, US DRIVE, Hydrogen Production Technical Team (HPTT), January 2009.

[3] The U.S. Department of Energy, Annual Energy Outlook 2009: With Projections to 2030, United States Department of Energy, Energy Information Administration, 2009.

[4] http://www1.eere.energy.gov/hydrogenandfuelcells/fuelcells/transportation.html.

[5] V. Mehta, J. S. Cooper, "Review and Analysis of PEM Fuel Cell Design and Manufacturing," Journal of Power Sources, vol. 114, pp. 32–53, 2003.

[6] S. Gottesfeld, T. Zawodzinski, "Polymer Electrolyte Fuel Cells," Advance Electrochemical Science Engineering 5 (1997) 195–301.

[7] EG&G Services, Fuel Cell Handbook, 5th edition, Parsons Inc., October 2000.

[8] K. Jost, "Fuel Cell Concepts and Technology," Automotive Engineering International, March 2000.

[9] http://automobiles.honda.com/fcx-clarity/drive-fcx-clarity.aspx.

[10] A. Emadi, K. Rajashekara, S. Williamson, S. Lukic, "Topological Overview of Hybrid Electric and Fuel Cell Vehicular Power System Architectures and Configurations," IEEE Transactions on Vehicular Technology, vol.54, no. 3, pp. 763–770, May 2005.

[11] http://www.fueleconomy.gov/feg/fcv_benefits.shtml.

[12] M. Melendez, A. Milbrandt, "Analysis of the Hydrogen Infrastructure Needed to Enable Commercial Introduction of Hydrogen–fueled Vehicles," National Hydrogen Association Annual Hydrogen Conference, Washington DC, March 29–April 1, 2005.

[13] The U.S. Department of Energy, Progress and Accomplishments in Hydrogen and Fuel Cells, 2013.

[14] The U.S. Department of Energy, Hydrogen and Fuel Cell Activities, Progress, and Plans: Report to Congress, 2009.

[15] http://www.fueleconomy.gov/feg/fcv_benefits.shtml.

[16] A. Z. Weber, J. Newman, "Coupled Thermal and Water Management in Polymer Electrolyte Fuel Cells," Journal of The Electrochemical Society, vol. 153, iss. 12, pp. A22005–A2214, December 2006.

[17] W. He, J.S. Yi, T.V. Nguyen, “Two–Phase Flow Model of The Cathode of PEM Fuel Cells Using Interdigitated Flow Fields”, AIChE Journal, vol.46, iss.10, pp.2053–2064, October 2000.

[18] Z.H. Wang, C.Y. Wang, K.S. Chen, “Two–Phase Flow and Transport in The Air Cathode of Proton Exchange Membrane Fuel Cells”, Journal of Power Sources, vol. 94, iss. 1, pp. 40–50, February 2001.

[19] A.Z. Weber, J. Newman, “Transport in Polymer–Electrolyte Membranes”, Journal of The Electrochemical Society, vol. 151, iss. 2, pp. A326-A339, January 2004.

[20] U. Pasaogullari, C.Y. Wang, “Liquid Water Transport in Gas Diffusion Layer of Polymer Electrolyte Fuel Cells,” Journal of the Electrochemical Society, vol. 151, no. 3, pp. A399–A406, 2004.

[21] D. Chen, H. Peng, “A Thermodynamic Model of Membrane Humidifiers for PEM Fuel Cell Humidification Control,” Journal of Dynamic Systems, Measurements, and Control, vol.127, iss. 3, pp. 424–433, September 2005.

[22] http://www1.eere.energy.gov/hydrogenandfuelcells/fuelcells/transportation.html.

[23] http://www.jari.or.jp/jhfc/e/beginner/about_fc/.

[24] A. Z. Weber, J. Newman, “Coupled Thermal and Water Management in Polymer Electrolyte Fuel Cells”, Journal of The Electrochemical Society, vol. 153, iss. 12, pp. A22005–A2214, December 2006.

[25] D. Chen, W. Li, H. Peng, “An Experimental Study and Model Validation of a Membrane Humidifier for PEM Fuel Cell Humidification Control,” Journal of Power Source, vol. 180, no. 1, pp. 461–467, 2008.

[26] H. Li, Y. Tang, Z. Wang, Z. Shi, S. Wu, D. Songa, J. Zhang, K. Fatih, J. Zhang, H. Wang, Z. Liu, R. Abouatallah, A. Mazza, “A Review of Water Flooding Issues in the Proton Exchange Membrane Fuel Cell”, Journal of Power Sources, vol. 178, pp. 103–117, March 2008.

[27] A. Weber, R.M. Darling, J. Newman, “Modeling Two–Phase Behavior in PEFCs,” Journal of Electrochemical Society, vol. 151, iss. 10, pp. A1715–A1727, 2004.

[28] T. Nguyen, R. White, “A Water and Heat Management Model for Proton-Exchange–Membrane Fuel Cells” Journal of the Electrochemical Society, vol. 140, iss. 8, pp. 2178–2186, August 1993.

[29] W. He, G. Lin, T. V. Nguyen, “Diagnostic Tool to Detect Electrode Flooding in PEM Fuel Cells,” AIChE J., 49, 3221–3228, 2003.

[30] G. Lin, T. V. Nguyen, “Effect of Thickness and Hydrophobic Polymer Content of the Gas Diffusion Layer on Electrode Flooding Level in a PEM Fuel Cell,” Journal of The Electrochemical Society, vol. 152, pp. A1942–A1948, 2005.

[31] W. Schmittinger, A. Vahidi, “A Review of the Main Parameters Influencing Long–term Performance and Durability of PEM Fuel Cells”, Journal of Power Sources vol. 180, pp. 1–14, 2008.

[32] G. Lin, T. V. Nguyen,” A Two–Dimensional Two–Phase Model of a PEM Fuel Cell,” Journal of The Electrochemical Society, vol. 153, iss. 2, pp. A372–A382, 2006.

[33] J. H. Nam, M. Kaviany, “Effective Diffusivity and Water Saturation Distribution in Single– and Two–Layer PEMFC Diffusion Medium,” International Journal Heat and Mass Transfer, vol. 46, pp. 4595–4611, 2003.

[34] J. H. Nam, K. Lee, G. Hwang , C. Kim, M. Kaviany, “Microporous Layer for water morphology control in PEMFC”, International Journal of Heat and Mass Transfer vol. 52, pp. 2779–2791, 2009.

[35] G. S. Hwang, M. Kaviany, J. H. Nam, M. H. Kim, S. Y. Son,” Pore–Water Morphological Transitions in Polymer Electrolyte of a Fuel Cell”, Journal of The Electrochemical Society, vol. 156, iss. 10, pp. B1192–B1200, 2009.

[36] H. Kim, T. Ha, S. Park, K. Min, M. Kim, “Visualization Study of Cathode Flooding with Different Operating Conditions in a PEM Unit Fuel Cell,” Proceedings Fuel Cell, Ypsilanti, Michigan, 2005.

[37] T. A. Trabold, J.P. Owejan, D.L. Jacobson, M. Arif, P.R. Huffman, “In Situ Investigation of Water Transport in an Operating PEM Fuel Cell Using Neutron Radiography: Part 1 – Experimental Method and Serpentine Flow Field Results”, International Journal of Heat and Mass Transfer, vol. 49, pp. 4712–4720, 2006.

[38] J. P. Owejan, T. A. Trabold, D.L. Jacobson, D.R. Baker, D.S. Hussey, M. Arif, “In Situ Investigation of Water Transport in an Operating PEM Fuel Cell Using Neutron Radiography: Part 2 – Transient Water Accumulation in an Interdigitated Cathode Flow Field”, International Journal of Heat and Mass Transfer, vol. 49, pp. 4721–4731, 2006.

[39] K. Nishida, T. Murakami, S. Tsushima, S. Hirai, “Measurement of Liquid Water Content in Cathode Gas Diffusion Electrode of Polymer Electrolyte Fuel Cell,” Journal of Power Sources, vol. 195, pp. 3365–3373, 2010.

[40] S. Litster, D. Sinton, N. Djilali, “Ex Situ Visualization of Liquid Water Transport in PEM Fuel Cell Gas Diffusion Layers,” Journal of Power Sources, vol. 154, pp. 95–105, 2006.

[41] A. Taniguchi, T. Akita, K. Yasuda, Y. Miyazaki, “Analysis of Electrocatalyst Degradation in PEMFC Caused by Cell Reversal during Fuel Starvation,” Journal of Power Sources, vol. 130, pp. 42–49, 2004.

[42] R. Borup, J. Meyers, B. Pivovar, Y. S. Kim, R. Mukundan, N. Garland, D. Myers, M. Wilson, F. Garzon, D. Wood, P. Zelenay, K. More, K. Stroh, T. Zawodzinski,

J. Boncella, J. E. McGrath, M. Inaba, K. Miyatake, M. Hori, K. Ota, Z. Ogumi, S. Miyata, A. Nishikata, Z. Siroma, Y. Uchimoto, K. Yasuda, K. Kimijima, N. Iwashita, “Scientific Aspects of Polymer Electrolyte Fuel Cell Durability and Degradation”, Chemical Review, vol. 107, pp. 3904–3951, 2007.

[43] F. A. de Bruijn, V. A. T. Dam, G. J. M. Janssen, “Review: Durability and Degradation Issues of PEM Fuel Cell Components”, FUEL CELLS 08, no. 1, pp. 3–22, 2008.

[44] S. Zhang, X. Yuana, H. Wanga, W. Me´rida, H. Zhuc, J. Shena, S. Wua, J. Zhanga, “A Review of Accelerated Stress Tests of MEA Durability in PEM Fuel Cells,” International Journal of Hydrogen Energy, vol. 34, pp. 388–404, 2009.

[45] M. Cai, M. S. Ruthkosky, B. Merzougui , S. Swathirajan, M. P. Balogh, Se H. Oh, “Investigation of Thermal and Electrochemical Degradation of Fuel Cell Catalysts”, Journal of Power Sources, vol. 160, pp. 977–986, 2006.

[46] T.E. Springer, T.A. Zawodzinski, S. Gottesfeld, ”Polymer Electrolyte Fuel Cell Model,” Journal of Electrochemical Society, vol. 138, iss. 8, pp. 2334–2342, 1991.

[47] X. Wang, T. V. Nguyen, “Modeling the Effects of the Microporous Layer on the NetWater Transport Rate Across the Membrane in a PEM Fuel Cell,” Journal of The Electrochemical Society, vol. 157, iss. 4, pp. B496–B505, 2010.

[48] F. Khemili, M. Najjari, S. B. Nasrallah, “Transient Thermal Model for Proton Exchange Membrane Fuel Cells,” Journal of Fuel Cell Science and Technology, vol. 9, no. 2, 0pp. 21008, 2012.

[49] S. Didierjean, O. Lottin, G. Maranzana, T. Geneston, “PEM Fuel Cell Voltage Transient Response to a Thermal Perturbation,” Electrochimica Acta, vol. 53. pp. 7313–7320, 2008.

[50] S. Shimpalee, D. Spuckler, J. W. Van Zee, “Prediction of Transient Response for a 25-cm^2 PEM Fuel Cell,” Journal of Power Sources, vol. 167, no. 1, pp. 130–138, 2007.

[51] L. S. Martins, J. E. F. C. Gardolinski, J. V. C. Vargas, J. C. Ordonez, S. C. Amico, M. M. C. Forte, ”The Experimental Validation of a Simplified PEMFC Simulation Model for Design and Optimization Purposes,” Applied Thermal Engineering, vol. 29, pp. 3036–3048, 2009.

[52] D. DiPenta, K. Bencherif, M. Sorine, Q. Zhang, ”A Reduced Fuel Cell Stack Model for Control and Fault Diagnosis,” Journal of Fuel Cell Science and Technology, vol. 3, no. 4, pp. 384–388, 2006.

[53] E. A. Muller, A. G. Stefanopoulou, “Analysis, Modeling, and Validation for the Thermal Dynamics of a Polymer Electrolyte Membrane Fuel Cell System,” Journal of Fuel Cell Science and Technology, vol. 3, no. 2, pp.99–110, 2006.

[54] J. R. Kolodziej, “Thermal Dynamic Modeling and Nonlinear Control of a Proton Exchange Membrane Fuel Cell Stack”, Journal of Fuel Cell Science and Technology, Vol. 4, pp. 255, August 2007.

[55] Y. Zhang, M. Ouyang, Q. Lu, J. Luo, X. Li, “A Model Predicting Performance of Proton Exchange Membrane Fuel Cell Stack Thermal Systems”, Applied Thermal Engineering, vol. 24, pp. 501–513, 2004.

[56] Y. Shan, S. Choe, “A High Dynamic PEM Fuel Cell Model with Temperature Effects,” Journal of Power Sources, vol. 145, pp. 30–39, July 2005.

[57] Y. Shan, S. Choe, “Modeling and Simulation of a PEM Fuel Cell Stack Considering Temperature Effects,” Journal of Power Sources, vol. 158, pp. 274–286, 2006.

[58] F. Incropera, D. Dewitt, T. Bergman, A. Lavine, “Fundamentals of Heat and Mass Transfer,” sixth edition, John Wiley & Sons, 2007.

[59] A. F. Mills, Heat Transfer, Upper Saddle River, NJ: Prentice Hall, Print, 1999.

[60] J. T. Pukrushpan, A. G. Stefanopoulou, H. Peng, “Control of Fuel Cell Power Systems,” Springer–Verlag, Telos, 2004.

[61] R. T. Meyer, B. Yao, “Modeling and Simulation of a Modern PEM Fuel Cell System,” Proceedings of Fuel Cell 2006, Irvine, CA., June 2006.

[62] J. Larminie, A. Dicks, “Fuel Cell Systems Explained,” Chichester: John Wiley, Print, 2000.

[63] D. Chen, D. E. Seborg, “Relative Gain Array Analysis for Uncertain Process Models,” AIChE Journal, vol. 48, pp. 302–310, 2002.

[64] F.G. Shinskey, Process Control Systems: Application, Design, and Tuning, Fourth Edition, McGraw-Hill, Inc., 1996.

[65] B. Hadisujoto, R. Refai, D. Chen, T.J. Moon, “Dynamic Thermal Model of PEM Fuel Cells for MIMO Control Design,” Proceedings of ASME Dynamic Systems and Control Conference, September 13–15, 2010.

[66] D. Natarajan, T. V. Nguyen, “A Two-Dimensional, Two–Phase, Multicomponent, Transient Model for the Cathode of a Proton Exchange Membrane Fuel Cell Using Conventional Gas Distributors”, Journal of The Electrochemical Society, vol. 148, iss. 12, pp. A1324–A1335, 2001.

[67] G. Lin, W. He, T. V. Nguyen, “Modeling Liquid Water Effects in the Gas Diffusion and Catalyst Layers of the Cathode of a PEM Fuel Cell,” Journal of The Electrochemical Society, vol. 151, iss. 12, pp. A1999–A2006, 2004.

[68] Q. Ye, T.V. Nguyen, “Three–Dimensional Simulation of Liquid Water Distribution in a PEMFC with Experimentally Measured Capillary Functions,” Journal of The Electrochemical Society, vol. 154, iss. 12, pp. B1242–B1251, 2007.

[69] X. Wang, T. V. Nguyen, “Modeling the Effects of Capillary Property of Porous Media on the Performance of the Cathode of a PEMFC,” Journal of The Electrochemical Society, vol. 155, iss. 11, pp. B1085–B1092, 2008.

[70] C.Y. Wang, “Fundamentals Models for Fuel Cell Engineering,” Chemical Review vol. 104, pp. 4727–4766, 2004.

[71] U. Pasaogullari, C.Y. Wang, “Two–Phase Transport and the Role of Micro-Porous Layer in Polymer Electrolyte Fuel Cells,” Electrochimica Acta, vol. 49, pp. 4359–4369, 2004.

[72] U. Pasaogullari, C.Y. Wang, K.S. Chen, “Two–phase Transport in Polymer Electrolyte Fuel Cells with Bilayer Cathode Gas Diffusion Media,” Journal of Electrochemical Society, vol. 152, no. 8, pp. A1574–A1582, 2005.

[73] Y. Wang, C.Y. Wang, K.S. Chen, “Elucidating Differences Between Carbon Paper and Carbon Cloth in Polymer Electrolyte Fuel Cells,” Electrochimica Acta, vol. 52, pp. 3965–3975, 2007.

[74] H. Meng, C.Y. Wang, “Model of Two–phase Flow and Flooding Dynamics in Polymer Electrolyte Fuel Cells,” Journal of Electrochemical Society, vol. 152, no. 9, pp. A1733–A1741, 2005.

[75] M. V. Williams, E. Begg, L. Bonville, H.R. Kunz, J. M Fenton, “Characterization of Gas Diffusion Layers for PEMFC”, Journal of The Electrochemical Society, vol. 151, iss. 8, pp. A1173–A1180, 2004.

[76] L. Cindrella, A.M. Kannana, J.F. Lina, K. Saminathana, Y. Hoc, C.W. Lind, J. Wertz , “Gas Diffusion Layer for Proton Exchange Membrane Fuel Cells—A Review”, Journal of Power Sources, vol. 194, pp. 146–160, 2009.

[77] M. Hana, J.H. Xua, S.H. Chana, S.P. Jiang, “Characterization of Gas Diffusion Layers for PEMFC”, Electrochimica Acta, vol. 53, pp. 5361–5367, 2008.

[78] J. T. Gostick, M. W. Fowler, M. A. Ioannidis, M. D. Pritzker, Y. M. Volfkovich, A. Sakars, “Capillary Pressure and Hydrophilic Porosity in Gas Diffusion Layers for Polymer Electrolyte Fuel Cells”, Journal of Power Sources, vol. 156, pp. 375–387, 2006.

[79] V. Gurau, M. J. Bluemle, E. S. De Castro, Y. Tsou, J. A. Mann Jr., T. A. Zawodzinski Jr., “Characterization of Transport Properties in Gas Diffusion Layers for Proton Exchange Membrane Fuel Cells. Part 1. Wettability (Internal Contact Angle to Wwater and surface energy of GDL fibers)”, Journal of Power Sources 160, 1156–1162, 2006.

[80] V. Gurau, M. J. Bluemle, E. S. De Castro, Y. Tsou, J. A. Mann Jr., T. A. Zawodzinski Jr., “Characterization of Transport Properties in Gas Diffusion Layers for Proton Exchange Membrane Fuel Cells. Part 2. Absolute Permeability”, Journal of Power Sources, vol. 165, pp. 793–802, 2007.

[81] J. T. Gostick, M.A. Ioannidis, M.W. Fowler, M.D. Pritzker, “Wettability and Capillary Behavior of Fibrous Gas Diffusion Media for Polymer Electrolyte Membrane Fuel cells,” Journal of Power Sources, vol. 194, pp. 433–444, 2009.

[82] J. T. Gostick, M. W. Fowler, M. D. Pritzker, M. A. Ioannidis, L. M. Behra, “In–Plane and Through–Plane Gas Permeability of Carbon Fiber Electrode Backing Layers,” Journal of Power Sources, vol. 162, pp. 228–238, 2006.

[83] J. T. Gostick, M. W. Fowler, M. A. Ioannidis, M. D. Pritzker, Y. M. Volfkovich, A. Sakars, “Capillary Pressure and Hydrophilic Porosity in Gas Diffusion Layers for Polymer Electrolyte Fuel Cells,” Journal of Power Sources, vol. 156, pp. 375–387, 2006.

[84] J. T. Gostick, M. A. Ioannidis, M. W. Fowler, M. D. Pritzker, ”Direct Measurement of the Capillary Pressure Characteristics of Water–Air–Gas Diffusion Layer Systems for PEM Fuel Cells,” Electrochemistry Communications, vol. 10, pp. 1520–1523, 2008.

[85] J. T. Pukrushpan, A. G. Stefanopoulou, H. Peng, “Control–Oriented Modeling and Analysis for Automotive Fuel Cell Systems,” Transaction ASME, vol. 126, pp. 14–25, 2004.

[86] B. A. McCain, J. B. Siegel, A. G. Stefanopoulou, “Stack–Level Validation of a Semi–Analytic Channel–to–Channel Fuel Cell Model for Two–phase Water Distribution Boundary Value Control,” Proceeding of American Control Conference, pp. 5098–5103, 11–13 June 2008.

[87] D. A. McKay, J. B. Siegel, W. Ott, A. G. Stefanopoulou, “Parameterization and Prediction of Temporal Fuel Cell Voltage Behavior during Flooding and Drying Conditions,” Journal of Power Sources, vol. 178, iss. 1, pp. 207–222, 2008.

[88] G. Vasu, A. Tangirala, “Control Oriented Thermal Model for Proton Exchange Membrane Fuel Cell Systems” Journal of Power Sources, vol. 183, pp 98–108, August 2008.

[89] A. J. del Real, A. Arce, C. Bordons, “Development and Experimental Validation of a PEM Fuel Cell Dynamic Model,” Journal of Power Sources, vol. 173, iss. 1, pp. 310–324, 2007.

[90] P. R. Pathapati, X. Xue, J. Tang, “A New Dynamic Model for Predicting Transient Phenomena in A PEM Fuel Cell System,” Renewable Energy, vol. 30, iss. 1, pp. 1–22, January 2005.

[91] P. Schmidt, O. Ezekoye, J. Howell, D. Baker, “Thermodynamics: An integrated Learning System,” John Wiley & Sons, 2006.

[92] R. T. Meyer, B. Yao, “Modeling and Simulation of a Modern PEM Fuel Cell System,” Proceedings of Fuel Cell, Irvine, CA., June 2006.

[93] G. Inoue, T. Yoshimoto, Y. Matsukuma, M. Minemoto, “Development of Simulated Gas Diffusion Layer of Polymer Electrolyte Fuel Cells and Evaluation of Its Structure,” Journal of Power Sources, vol. 175, pp. 145–158, 2008.

[94] T. V. Nguyen, G. Lin, H. Ohn, and X. Wang, ”Measurement of Capillary Pressure Property of Gas Diffusion Media Used in Proton Exchange Membrane Fuel Cells,” Electrochemical and Solid–State Letters, vol. 11, no. 8, pp. B127-B131, 2008.

[95] T. V. Nguyen, G. Lin, H. Ohn, D. S. Hussey, D. L. Jacobson, M. Arif, “Measurement of Two–phase flow Properties of the Porous Media Used in PEM Fuel Cells,” ECS Transaction, vol.3, iss. 1, pp. 415–423, 2006.

[96] J. D. Fairweather, P. Cheung, J. St–Pierre, D. T. Schwartz, “A Microfluidic Approach for Measuring Capillary Pressure in PEMFC Gas Diffusion Layers,” Electrochemistry Communications, vol. 9, pp. 2340–234, 2007.

[97] J. Hinatsu, M. Mizuhata, H. Takenaka, “Water Uptake of Perfluorosilfonic Acid Membranes from Liquid Water and Water Vapor,” Journal of Electrochemical Society, vol. 141, pp. 1493, 1994.

[98] T. A. Zawodzinski, T. E. Springer, J. Davey, R. Jestel, C. Lopez, J. Valerio, G. Gottesfeld, “A Comparative Study of Water Uptake by and Transport through Ionomeric Fuel Cell Membranes,” Journal of Electrochemical Society, vol. 140, iss. 7, pp. 1981–1985, 1993.

[99] M. Mathias, J. Roth, J. Fleming, W. Lehnert, W. Vielstich, H. Gasteiger, A. Lamm, “Handbook of Fuel Cells: Fundamentals, Technology and Applications,” vol. 3, John Wiley & Sons Ltd, 2003.

[100] S. Kim, M. Mench, “Investigation of Temperature–Driven Water Transport in Polymer Electrolyte Fuel Cell: Phase–Change–Induced Flow,” Journal Electrochemical Society, vol. 156, iss. 3, pp. B353–B362, 2009.

[101] T. Colinarta, A. Chenua, S. Didierjeana, O. Lottin, S. Besseb, “Experimental Study on Water Transport Coefficient in Proton Exchange Membrane Fuel Cell,” Journal of Power Sources, vol. 190, pp. 230–240, 2009.

[102] F. Barbir, PEM Fuel Cells: Theory and Practice, Elsevier, Burlington, MA, 2012.

[103] F. Y. Zhang, X. G. Yang, C. Y. Wang, “Liquid Water Removal from a Polymer Electrolyte Fuel Cell,” Journal of The Electrochemical Society, vol.153, iss. 2, pp. A225–A232, 2006.

[104] B. R. Munson, D. F. Young, T. H. Okiishi, “Fundamentals of Fluid Mechanics,” fifth edition, John Wiley & Sons, 2005.

[105] H. Ju, C.Wang, S. Cleghorn, U. Beuscher, “Nonisothermal Modeling of Polymer Electrolyte Fuel Cells,” Journal of Electrochemical Society, vol. 152, pp. A1645, 2005.

[106] J. Amphlett, R. Baumert, R. Mann, B. Peppley, P. Roberge, “Performance Modeling of the Ballard Mark IV Solid Polymer Electrolyte Fuel Cell,” Journal of Electrochemical Society, vol.142, 1995.

[107] Y. Wang, C. Wang, “Two–Phase Transient of Polymer Electrolyte Fuel Cells,” Journal of Electrochemical Society, vol. 154, pp. B636, 2007.

[108] K. C. Neyerlin, W. Gu, J. Jorne, H. A. Gasteiger, “Determintation of Catalyst Unique Parameters for the Oxygen Reduction Reaction in a PEMFC,” Journal of the Electrochemical Society, vol. 153, iss. 10, pp. A1955–A196, 2006.

[109] C. Francia, V. S. Ijeri, S. Specchia, P. Spinelli, “Estimation of Hydrogen Crossover through Nafion Membranes in PEMFCs,” Journal of Power Sources, vol. 196, iss. 4, pp. 1833–1839, 2011.

[110] R. Berber, “Methods of Model Based Process Control,” Kluwer Academic Publishers, 1994.

[111] B. G. Liptak, “Process Control and Optimization,” Instrument Engineers’ Handbook, fourth edition, 2006.

[112] F.G. Shinskey, “Process Control Systems: Application, Design, and Tuning,” Fourth Edition, McGraw–Hill, Inc., 1996.

[113] J. Chang, C. Yu, “Relative Disturbance Gain Array,” Journal of American Institute of Chemical Engineers, vol.38, no. 4, 1992.

[114] N. S. Nise, “Control Systems Engineering,” Fourth Edition, John Wiley and Sons, 2004.

[115] MATLAB, Simulink, Control System Design Toolbox, Release 2012b, The MathWorks, Inc., Natick, MA, 2012.